9-27-2019 10:30 AM

Development of a Co-Rotating, Fully Intermeshing Twin-Screw Extruder Model for the Extrusion of Natural Fibre Suspensions

Keller J H George
The University of Western Ontario

Supervisor
Hrymak, Andrew N.
The University of Western Ontario Co-Supervisor
El Naggar, M. Hesham
The University of Western Ontario

Graduate Program in Chemical and Biochemical Engineering
A thesis submitted in partial fulfillment of the requirements for the degree in Doctor of Philosophy

Recommended Citation

George, Keller J H, "Development of a Co-Rotating, Fully Intermeshing Twin-Screw Extruder Model for the Extrusion of Natural Fibre Suspensions" (2019). *Electronic Thesis and Dissertation Repository*. 6557.
https://ir.lib.uwo.ca/etd/6557

Abstract

Twin-screw extruders are continuous processing devices that have been used in many industries concerned with the processing of multiphase fibrous suspensions, such as the food and pulping industries. While these devices offer great flexibility due to their modularity and customizability, optimization for specific applications can be challenging due to the unavailability of reliable, global models with accurate predictive capabilities. Consequently, this work seeks to eliminate this knowledge gap with the development of a novel global, composite model capable of predicting key process outputs for suspension-processing, phase-separating, co-rotating, fully-intermeshing twin-screw extruders. Creation of the novel global algorithm involved the modification of existing plasticating twin-screw extruder modelling techniques. To account for two phase flow, the power-law model typically used to describe the rheological behaviour of molten polymer in plasticating extruders was replaced with the Herschel-Bulkley model, which has been used to describe the flow of fibrous suspensions in pipes. Terzaghi's 1D consolidation equation was used to describe the phase separation taking place in the filtering sections of the extruder, and the absorption properties of the fibres in suspension were accounted for using a correlation developed for water-immersed woods. The extruder model was implemented as 'TSESimFibre' in MATLAB. A parametric study was carried out to assess the effect of operation parameters and screw configuration on the outcomes of the twin-screw extrusion system. The major performance parameter monitored was net liquid extraction rate from the extruder. The operation parameters assessed were the flow rate of wash liquid at the filter, and the dry fibre flow rate through the extruder. The screw configuration features investigated were the location of the reverse screw element, and the length of the filtering section. The simulations revealed that higher wash liquid flow rates and lower dry fibre flow rates were the best operating conditions to maximize net liquid extraction rates from the system. The simulations also revealed that longer filtering sections had smaller net liquid extraction flow rates, while the location of the reverse screw element had no effect.

Keywords

Twin-screw extruder, extruder geometry, two-phase flow, phase separation, woody biomass, extruder modelling

Summary for Lay Audience

A novel, global simulator was developed to predict the system response of a solid/liquid separating twin-screw extruder used for the processing of wood fibre suspensions. To begin this work, literature on polymer-processing twin-screw extruders was explored to find equations relating predicted parameters (i.e. pressure, residence time, filling ratio …) to the extruder's dimensions, operating conditions and processed material properties, and needed to be modified for the case of suspension-processing extruder applications. Modifications to those traditional modelling practices required the exploration of literature sources describing fibre behaviour across various disciplines. Techniques used to describe the rheological behaviour of flowing fibrous suspensions were gleaned from the materials literature, while that describing its consolidation behaviour was gleaned from the geotechnical engineering literature. The liquid absorption characteristics of the fibres in suspension was obtained from literature related to wood properties. Together, this information was used to modify existing extruder modelling procedures for two-phase, phase-separating twin-screw extruder applications. The novel model was validated using data obtained from Greenfield Global Inc. to assess the predictive capabilities of the simulator, and a parametric study was carried out to assess the effect of various extruder design features and operating conditions on pivotal model responses.

Acknowledgements

I would like to sincerely thank my supervisors, Dr. Andrew Hrymak and Dr. M. Hesham El Naggar, for their guidance throughout my studies – completion of this work would not have been possible without their wisdom, insights, inspiration and support. I have sincerely enjoyed my time under their tutelage, and I have learned to become more analytical, independent and confident.

I would also like to thank Dr. Mamdouh Abou-Zaid for his knowledge and expertise with chemical characterization techniques, and Dr. Aly Ahmed for his knowledge and assistance with the numerous soil characterisation methods and analyses employed throughout this work. I am also thankful to Biotron for their help with the imaging techniques used for the physical characterisation studies.

A very special thanks to Greenfield Global Inc. (referred to as Greenfield hereafter) for sharing their extruding system, materials and data, and for their financial contributions to the project.

I would also like to thank my friends and colleagues, in particular Dr. Tulip Chakraborty, Dr. Malini Ghosh, Oyefisayo Olufidipe, Dr. Shengtai Zhou and Tian Nan. Thank you for encouraging, listening, supporting, and accommodating me over the years.

This thesis is dedicated to my parents Joshua and Fidelis George, my sister Londa George, my aunt Beverlyann Early and my deceased grandmothers Esther George and Theodora Phillip. Their encouragement and limitless love, both past and current, compels me to do my very best, to be honest in all my actions, and to persevere through difficulties.

"No testing has overtaken you that is not common to everyone. God is faithful, and he will not let you be tested beyond your strength, but with the testing he will also provide the way out so that you may be able to endure it."

1 Corinthians 10:13

Table of Contents

List of Tables

List of Figures

Nomenclature

Symbol	**Description**	**Unit**
A_b	Barrel Cross-sectional Area (perpendicular to flow direction)	m^3
A_s	Screw Cross-sectional Area (perpendicular to flow direction)	m^2
B	Pitch	m
$^{E}/_{R}$	Activation Energy-to-Universal Gas Constant Ratio	K
C_c	Compression Index = $C_c{}'(1+e_{r0})$	-
$C_c{}'$	Compression Ratio	-
C_L	Centerline Distance	m
C_p	Heat Capacity	J/kg·K
$C_r{}'$	Recompression Ratio	-
c_v	Coefficient of Consolidation	m^2/s
e	Flight Land Width	m
e_r	Void Ratio	-
f_d	Drag Flow Shape Factor	-
f_p	Pressure Flow Shape Factor	-
f_R	Filling Ratio	-
h	Depth	m
h_b	Barrel Heat Transfer Coefficient	W/m^2·K
h_v	Dimensionless Depth	-
$\bar{h}$	Average Depth	m
k	Thermal Conductivity	W/m·K
K	Permeability	m^2
k_{asb}	Liquid Absorption Coefficient	Kg/m^2·s$^{1/2}$
k_{kc}	Kozeny Constant	-
K_n	Consistency (rheological)	Pa·s^n
k_v	Hydraulic Conductivity	m/s
L	Extruder Length	m
$\dot{m}$	Mass Flow Rate	kg/s
$\dot{m}_{absorbed}$	Effective Mass Flow Rate of Water Absorbed by Fibres	kg/s
$\dot{m}_{Consolidation}$	Effective Mass Flow rate of Water Expressed from Consolidation	kg/s

$\dot{m}_{filtrate}$	Filtrate Mass Flow Rate	kg/s
$\dot{m}_{sf}$	Swollen Fibre Mass Flow Rate	kg/s
$\dot{m}_{wash\ liquid}$	Mass Flow Rate of Wash Liquid Injected at Filter	kg/s
m	Screw Start	-
m_a	Mass of Absorbed Liquid	kg
$m_{f,dry}$	Mass of Dry Fibres	kg
m_{sf}	Mass of Swollen Fibres	kg
m_v	Coefficient of Volume Compressibility	1/kPa
N	Screw Frequency of Rotation	rev/s
n	Flow Behavior Index	-
n_p	Porosity	-
OCR	Overconsolidation Ratio	-
P	Down-channel Pressure in single screw element	Pa
P_C	Down-channel Pressure (across C-chambers)	Pa
P_{exit}	Down-channel Pressure (across entire Intermeshing region)	Pa
P_I	Down-channel Pressure (across entire Intermeshing region)	Pa
P_w	Viscous Dissipation	W
P_v	Vertical Component of Pressure	Pa
$Q_{Consolidation}$	Expressed Liquid Flow Rate from Fibre Consolidation	m^3/s
Q_{Cv}	Down-channel Volumetric Flow Rate (C-chamber)	m^3/s
Q_{Cw}	Cross-channel Volumetric Flow Rate (C-chamber)	m^3/s
$Q_{filtrate}$	Total Liquid Flow Rate from Filter	m^3/s
Q_{Iv}	Down-channel Volumetric Flow Rate (Intermeshing Region)	m^3/s
$Q_{wash\ liquid}$	Wash Liquid Volumetric Flow Rate at Filter	m^3/s
r	r-direction	m
r_E	Screw External Radius	m
r_I	Internal Screw Radius	m
s	Material Speed in Extruder	m/s
S_a	Specific Surface Area of Fibres	m^2/kg
S_{As}	Surface Area of Screw	m^2
S_{Ab}	Surface Area of Barrel	m^2
S_S	Pitch Fraction or Step-size	m

T	Average Material C-chamber Temperature	K
T_b	Barrel Temperature	K
t_R	Residence Time	s
T_{ref}	Reference Temperature (Arrhenius Equation)	K
T_v	Dimensionless Time	-
t_{90}	Time taken for 90% Consolidation	s
u_v	Degree of consolidation	-
V	Volume of C-chamber fraction under consideration	m^3
v_c	Down-channel Velocity (C-chamber)	m/s
V_C	Volume of Single C-chamber fraction under consideration	m^3
V_I	Volume of Single Intermeshing Region fraction under consideration	m^3
w	Axial Location in extruder (z-direction)	m
w_c	Cross-channel Velocity (C-chamber)	m/s
W_C	Maximum C-chamber Width	m
W_I	Approximate Intermeshing Region Width	m
x_c	Consistency (i.e. dry fibre mass fraction)	-
z	z-direction	-

α	Flight Land Angle	rad
β	External Helix Angle	rad
ε	Vertical Strain	-
γ	Strain	-
$\dot{\gamma}$	Strain Rate	1/s
$\bar{\dot{\gamma}}$	Average Strain Rate	1/s
η	Viscosity	Pa·s
θ	Arbitrary Angle, θ-direction	rad
π	Trigonometric Constant	3.14159 …
ρ	Density	kg/m^3
ρ_{sf}	Swollen Fibre Density	kg/m^3
ρ_l	Density of Water	kg/m^3
τ	Shear Stress	Pa/m^2
φ	Intermeshing Angle	rad

φ'	Angle of Internal friction	-
ω	Screw Rotational Speed	rad/s

1. Introduction

Natural fibres have played an important role in the development of early human societies, and continue to do so even today. These include organic fibres, such as those from plants and animals, and inorganic fibres like mineral asbestos. There are many different types of organic plant and animal fibres. Animal fibres include silks, wools and cashmeres, and are primarily used in the textile industry. Conversely, the fibres from plants have much higher versatility. In addition to textiles, both cottons and flaxes are used in the production of speciality papers in the paper milling industry. Cottons are used in the manufacture of various currencies, while flaxes are used to produce cigarette paper. Plant fibres are also finding increasing application in the composite and renewable energy industries. Hemps and short flax fibres have been used to produce lighter, reinforced plastics with enhanced properties for further applications (i.e. the automotive industry), while a variety of different woody biomasses can be used to produce renewable, bio-based energy streams such as bio-ethanol and bio-butanol (Westenbroek 2000; Malherbe and Cloete 2002; Lin and Tanaka 2006; Stevens 2010, p.42, 73 - 84; Zheng 2014; Isikgor and Becer 2015; Gallos et al. 2017).

Over the years, many different devices have been employed to process plant and animal fibres. With respect to plant fibre processing, twin-screw extruders have found much utility in the polymer composite, food (i.e. pressing) and paper milling industries due to its continuous processing capabilities. Additionally, the high modularity of the device, due to an assortment of already available but customizable screw elements and barrel sections, permits the completion of a variety of different processing tasks. For example, use of high-shear generating screw elements provide enough mixing to blend various polymer-fibre mixes for use in the polymer composite industry. This industry also makes use of a wide variety of uniquely shaped dies to produce an equivalent number of uniquely shaped products. Solids-liquid separation can be achieved when a pressure-generating screw element configuration is used in tandem with slitted barrel sections, permitting liquid expulsion from the extruder. Such technologies are used extensively in the oil/juice-pressing and paper-milling industries, which primarily focus on fibrous suspension-processing. The paper-milling industry can also control the average length of the processed fibre through the implementation of screw elements with ‘cutting’ capabilities (Westenbroek 2000; Guy 2001, p. 29 - 30; Bouvier and Campanella 2014, p. 1 - 9; Gallos et al. 2017). Despite its already wide-spread usage, new applications for extruders in plant processing are continuously being developed. One of the more recent applications is for the mechanical pre-treatment of woody biomasses in the bioenergy industry (Zheng 2014).

Although twin-screw extruders are not exceptionally old devices, significant progress has been made in the development of numerical models for those dedicated to polymer-processing. Such models are able to predict key processing parameters (i.e. pressure, temperature, filling ratio and residence time) for a specific screw configuration and unique polymer, under certain operating conditions. Many of those models have since been developed into commercial software packages such as Ludovic (Vergnes et al. 1998), TXS (Canedo 1999), Akro-Co-Twin-Screw (White et al. 2001) and Sigma (Kretschmer et al. 2005), and are useful tools for designing, scaling and optimizing operations. Regrettably, far less research has been dedicated to the modelling of fibrous suspensions in twin-screw extruders. This lack of information has negatively affected the efficiency of older fibre extruding applications, and challenges the viability of newer ones. To minimize this knowledge gap, a new global, composite model has been proposed for the extrusion of a natural fibre suspension of shredded wood in a co-rotating, fully intermeshing twin-screw extruder owned by Greenfield. This extruder was used for the pre-treatment of poplar wood fibres for fermentation into bio-alcohols.

1.1. Description of Problem and Aim of Study

When compared to the available correlations, models, general literature and commercial simulators available for polymer-processing extruders, that pertaining to suspension-processing extruders is severely lacking, despite the prominence of such devices in major industries like the food and pulp processing industries. Of particular importance are correlations and theoretical models, which are often the foundation for commercial simulators. These simulators are useful tools for extruder design and optimization since they allow for the prediction of important parameters such as pressure, filling ratio, consistency and flow rate. To minimize this knowledge gap, this work aims to develop a novel, global model that is capable of predicting parameters pivotal to the operation of suspension-processing, co-rotating, fully-intermeshing twin-screw extruders.

To gain access to a suspension-processing twin-screw extruder, a partnership was forged with Greenfield, a company concerned with the renewable energy industry, among other things. The company used a pilot- scale, co-rotating, fully intermeshing twin-screw extruder to pre-treat a natural fibre suspension of poplar wood fibres to increase accessibility of their cellulosic sugars by disrupting the protective lignin layer within which the sugars are encased. The company was interested in the development of this model because it allowed for the quick isolation of theoretical operating conditions which promised the best performance and in so doing, provided a cheaper method for system optimization.

There are five major objectives that this study aims to fulfill:

- To understand existing methods and techniques used in polymer-processing twin-screw extruder global models and simulators. These techniques will be the foundation for the novel model that will be proposed.
- To modify a polymer-processing twin-screw extruder model for Greenfield's suspension-processing extruder (i.e. Extruder 2). Modifications will be centered around differences in the material behaviour of polymer melts and natural fibre suspensions. Since this extruder contains filtering sections with unique screw elements (i.e. flightless screw elements), a method for modelling such sections will also be sought after.
- To obtain the necessary material correlations required for the development of the novel global, suspension-processing extruder model. To do this, the physical, chemical, mechanical and surface properties of the poplar suspension entering and leaving Extruder 2 will be assessed using techniques such as light microscopy, SEM, mass spectrometry, HPLC, oedometeric and direct shear box testing.
- To develop the global suspension-processing extruder model into a simulator using MATLAB.
- To demonstrate the applicability of the novel, global simulator for design and optimization applications through a theoretical parametric study. The study will assess the effects of both operation and design parameters on selected model response predictions.

1.2. Structure of Thesis

This thesis is written in the monograph format and contains six major chapters. The first is the 'Introduction' chapter, and it discusses the knowledge gap to be eliminated, as well as the specific goals of the study. The second is the 'Literature Review' chapter, which is broken down into two major sections. The first section explores the techniques used in the modelling of a specific polymer-processing twin-screw extruder algorithm, and highlights the relevant equations. The second portion of the literature review explores literature on wood and wood suspensions across various disciplines such as the botany, materials and geotechnical engineering disciplines. The literature review is presented in great detail since it is the foundation for the model modification work presented in chapter four. The third is the 'Experimental' chapter, and it details the techniques used to characterize the biomass, including the methodologies, reagents and materials used. The fourth is the 'Discussion' chapter, and is broken down into two major sections. The first section summarizes the results obtained from the experimental procedures described in chapter three. Those results were analysed in order to characterize the physical, chemical and material properties of the woody biomass in the form of material constants and correlations. The second section of the discussion details the development of the novel, global composite model for natural suspension-processing twin-screw extruders, and also reviews the validation procedure used. Lastly, this section demonstrates how the simulator may be used to isolate the ideal operating and design conditions of a twin-screw extruder through a parametric study. The fifth is the 'Conclusion' chapter, which summarizes the major findings of the study. The sixth is the 'Recommendation' chapter, and proposes ideas for the further development of the model.

1.1. Statement of Originality

I assert that I am the sole author of this thesis, which has not been submitted in part or in its entirety to any other publishing body. To my knowledge, this work does not violate any copyrights or proprietary rights; all referenced work has been properly cited using standard referencing practices. I profess this to be a true copy of my thesis, inclusive of the feedback obtained from my thesis defense committee.

2. Literature Review

The design and development of a predictive simulator for a fibre processing twin-screw extruder is challenging because of the intricacies of extruding device geometries, and the complicated material behaviour of fibrous suspensions. To better understand this challenge, an extensive literature review was carried out, the results from which are presented below. The review surveys the literature for techniques relevant to the modelling of plasticating twin-screw extruders, as well as different techniques available for the modelling of fibrous materials.

2.1. Review of Plasticating Twin-screw Extruders

Extrusion is a process that involves the pumping, mixing, heating and shaping of materials through the use of a device called an extruder. A single screw extruder is a barrel-like vessel with an enclosed, close-fitting screw. This barrel is connected to a hopper for feeding at its beginning, and a die for shaping and purging at its end. The screw of an extruder is typically composed of small screw elements, which could be mounted onto a shaft, allowing this device great design flexibility. A schematic of a typical single screw extruder can be seen in Figure 1.

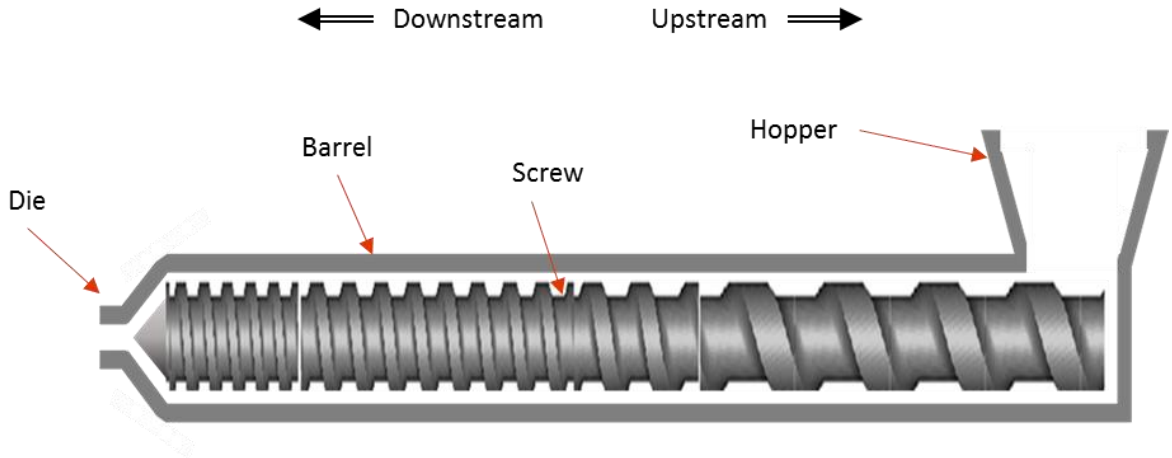

Figure 1: Single screw extruder

Parallel twin-screw extruders are variants of the single screw extruder, which include two screws oriented within the same horizontal plane. These twin-screw extruders can be classified based on relative screw rotations and inter-axial distances as depicted in Figure 2 below. With respect to relative screw rotations, the screws of a twin-screw extruder may move concurrently or in the same direction, as is the case for co-rotating twin-screw extruders. Screws may also move counter-currently or in opposing directions, as is the case for counter-rotating twin-screw extruders. Regarding inter-axial distances, twin-screw extruders may have different degrees of flight interlocking which vary from intermeshing, in which the flights of one screw infiltrate the screw channel of the second, to non-intermeshing, in which neighbouring flights do not interfere with each other's screw channels (Giles et al. 2004, p. 95 - 102; Stevens and Covas 2012, p. 317; Tadmor and Gogos 2013, p. 525 - 533).

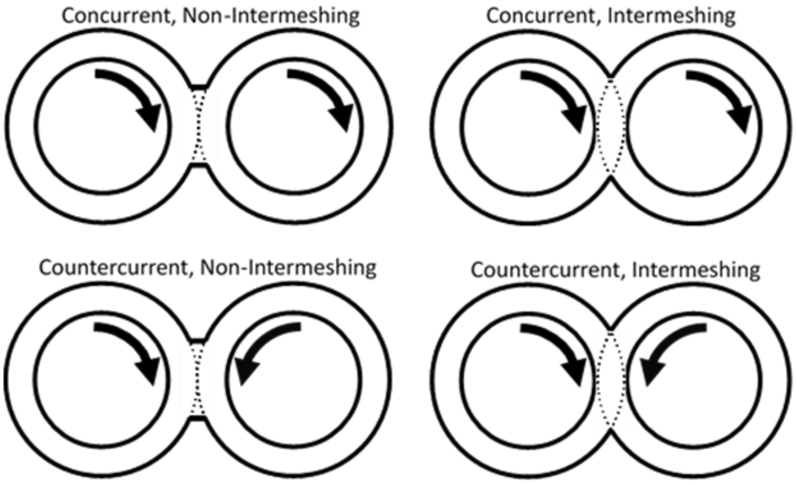

Figure 2: Twin-screw extruder classifications

Historically, the twin-screw extruder is known to contain three major zones with regard to polymer-processing – the solids conveying, melting and metering zones (Vergnes et al. 1998). The solids conveying zone refers to the region immediately following the hopper in which fed solids are transported and gradually compacted. Transition into the melting zone occurs when polymer solids begin melting due to temperature increases from shearing. After melting is completed, there is a final transition into the metering zone where the polymer melt experiences additional mixing before expulsion via the die. The uniqueness of each zone within a working twin-screw extruder mandates the development of unique models to adequately describe each zone. To gain an overall understanding of the system, these zone models are connected to yield a global, composite model that is unified by physical parameters such as temperature and pressure (Potente et al. 1996; Vergnes et al. 1998; Canedo 1999; Jiang 2008).

Over the years, several software packages have been developed from their published, literature fundamentals (Tang et al. 2003; Jiang 2008). These packages may be general simulation packages such as POLYFLOW or BEMflow (Tang et al. 2003), or specific twin-screw extruder simulators, a summary for which can be seen in Table 1. All software packages find their basis in transport equations, with the Navier-Stokes Equations being a popular option. However, differences between packages exist based on the quality of the assumptions which go into the simplification of these equations, such as the assumption of a cylindrical system for the case of Ludovic (Vergnes et al. 1998) and the use of a detailed melting model for the case of Akro-Co-Twin-screw (White et al. 2001). For the case of TSX, a 1D model is used to model the entirety of the extruding region for the sole purpose of maintaining simplicity and quick calculation speeds. Attempts to restore accuracy are achieved through the implementation of adjustable constants and the establishment of reasonable parameter limits (Canedo 1999).

Table 1: Selected co-rotating twin-screw extruder simulation packages.

Package	Developer	Features	Reference
Akro-Co-Twin-screw	University of Akron; USA	1D, 2D	(White et al. 2001)
Ludovic	CEMEF/INRA/SCC; France	1D, 2D	(Vergnes et al. 1998)
TXS	Polymer Process Institute; USA	1D	(Canedo 1999)
Sigma	University of Paderborn and Co; Germany	2D - 3D FEM	(Kretschmer et al. 2005)

*FEM – finite element method

As with any simulation package, the reliability of the results obtained are highly dependent on the correctness of the assumptions used in the development of the physical model, the precision with which the system's geometry may be re-created, and the accuracy of the mathematical technique used for obtaining the final solution. However, the efficiency of a simulator should not only be based off of a model's predictive capabilities, despite its arguable pre-eminence. According to Canedo (1999), a practical simulator should be efficient not only in terms of the time required for computation, but also in terms of simulation setup and result analysis. Additionally, efficient simulators should be able to run on modest hardware, and should not require special mathematical knowledge to be operated. While such requirements are easier met with the more simplistic 1D models, the trade-offs in accuracy can vary across systems. With those limitations in mind, careful consideration should be given to the specific extruder modelling technique considered. This literature review gives emphasis to the modelling technique used in Vergnes et al. (1998), which is schematically shown in Figure 3 below. The algorithm assumes a curved screw channel geometry and accordingly, is formulated from the Navier-Stokes Equations using the cylindrical co-ordinate system. This modelling technique is advantageous since it captures the major features of an extrusion system (such as curvature) without need for overly complex and time consuming 3D computations.

2.1.1. Inputs to Extruder Simulators

Inputs to the Vergnes et al. (1998) model for a plasticating twin-screw extruder can generally be classified into three major categories. The first category is that pertaining to the geometry and dimensions of the extruder. This includes definition of the external (or internal) screw radius, centreline distance (or diameter ratio) and the screw element profile (pitch, handedness, screw start and section length). The second category of inputs pertains to the operating conditions of the extruder, and includes material mass flow rate, screw frequency of rotation, barrel temperature and the die pressure at the exit of the extruder. The last category concerns the properties of the processed material. For the case of a thermoplastic, these include properties such as heat capacity, thermal conductivity, melting temperature, density and viscosity. If the material's viscosity is variable, then the parameters of the relevant viscosity correlation should be defined instead. A common model used to describe the viscosity of molten polymers is the Ostwald–de Waele relationship, or the power law model. This relationship requires the specification of the polymer's rheological consistency and flow behaviour index. If the effect of temperature is also considered, the Arrhenius form may be used in conjunction, and requires the specification of two additional parameters, reference temperature and the ratio of activation energy-to-universal gas constant.

The Vergnes et al. (1998) model starts its calculation at the extruder's die, resulting in the back-calculation of unknowns till the hopper. This design is favoured since parameters at the die tend to be more defined, and facilitate easier model development. The following subsections detail the equations required to fulfill the aforementioned model.

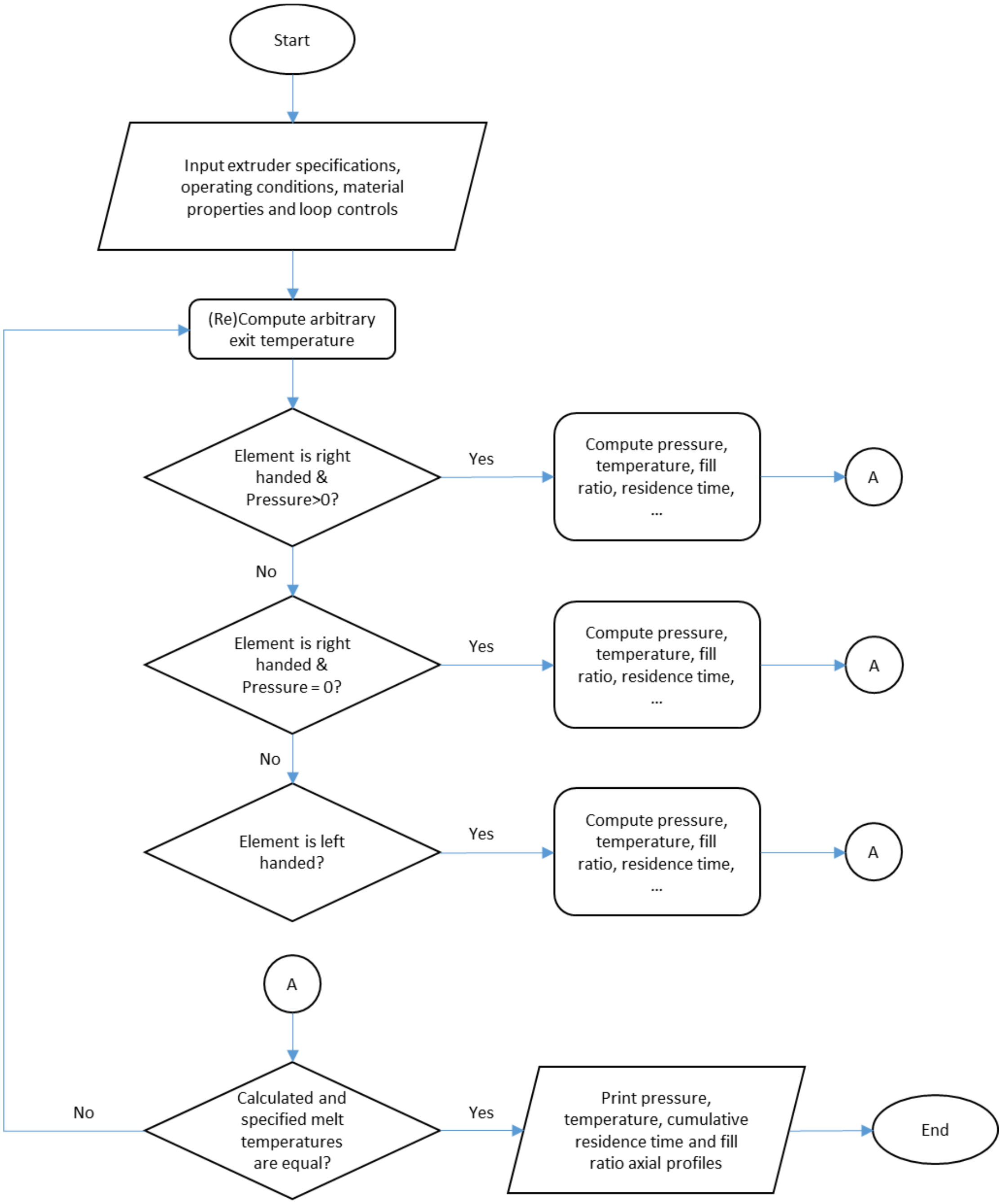

Figure 3: General algorithm for plasticating extruders according to Vergnes et al. (1998)

2.1.2. Geometry of a Self-Wiping Twin-screw Extruder

2.1.2.1. Screw Element Geometry

The geometry of self-wiping twin-screw extruders has been discussed in several research articles (Booy 1978; Potente et al. 1990, 1994; Vergnes et al. 1998), text books (Stevens 1985; Kohlgrüber 2008; Tadmor and Gogos 2013; Rauwendaal 2014) and theses (Strutt 1998; Elsey 2002). The term 'self-wiping' refers to twin-screw extruders with negligible clearances between their screws, consequently allowing one screw to 'wipe' product off of its companion screw. This subsection summarizes the specific equations that geometrically describe a self-wiping twin-screw extruder.

To begin, one should first consider the cross-section of the twin-screw extruder shown in Figure 4 below. From this figure, the three major parameters required for defining an extruder's geometry, in addition to the screw's pitch (B) and start (m), are shown – the centreline distance (C_L), the external screw radius (r_E) and the intermeshing angle (φ). The pitch of the screw refers to the axial distance between two screw flights, while the start refers to the number of threads that are wrapped around a screw. From the figure, it could be seen that the centreline distance is the distance between the centres of the two screws in a twin-screw extruder, while the external screw radius intuitively indicates the distance from a screw's centre to its flights (or the barrel wall if the assumption of a negligible flight clearance is made). Lastly, the intermeshing angle, as seen in the figure, measures the degree of intermeshing between the two screws of a twin-screw extruder – the closer the two screws are set to each other, the larger the degree of intermeshing and its associated angle.

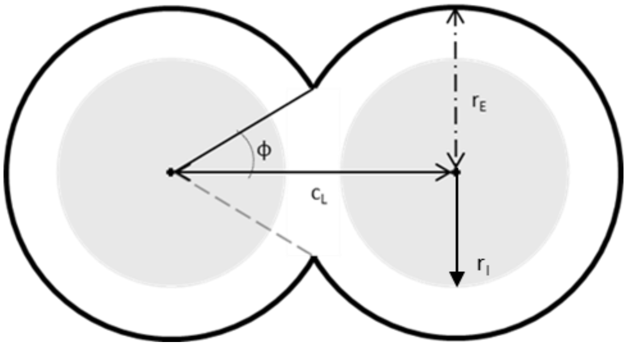

Figure 4: Cross-section of twin-screw extruder

From Figure 4 above, a mathematical relationship between the centreline distances, external screw radius and intermeshing angle may be inferred. This relationship, trigonometric in nature, is shown in Equation 1. Due to this dependence, only two parameters are required of the user as the third may be easily calculated. For the case of the model proposed by Vergnes et al. (1998), values for the centreline distance and external screw radius need to be entered, while the value of phi is calculated.

Equation 1: Intermeshing Angle

$$\varphi = \cos^{-1}\left(\frac{C_L}{2r_E}\right)$$

In addition to the intermeshing angle, there are two other angles required by the generalized model proposed by Vergnes et al. (1998) – the flight land angle (α) and the external helix angle (β) as seen in Equation 2 and Equation 3 respectively (Potente et al. 1990).

Equation 2: Flight Land Angle

$$\alpha = \frac{\pi}{m} - 2\varphi$$

Equation 3: (External) Helix Angle

$$\beta = \tan^{-1}\left(\frac{B}{2r_E\pi}\right)$$

To continue to define the twin-screw extruder, it is helpful to visualise the device in three dimensions, as shown in Figure 5. From this figure, the free volume available for material flow (for the complementary pair of dot-indicated screw elements) is shown through various views. The flow between a pair of complementary screw elements is ‘figure 8’ shaped, and can be easily separated into two distinct regions – the C-chamber region and the intermeshing region. Equations for obtaining the volume of a single C-chamber fraction and intermeshing region fraction can be seen in Equation 4 and Equation 5 respectively (Elsey 2002). In those equations, S_S is the instantaneous step-size or element length under consideration, and A_S is defined by Equation 7. It should be pointed out that the sum of two times the C-chamber volume and four times the intermeshing region volume yields the total free volume obtained from Booy's (1978) equation for a given step-size. That proposed by Booy is shown in Equation 6 below, from which A_b is defined by Equation 8. All volume calculations are performed on the sectionalized screw profile and thus, the instantaneous step-size is used in favour of the element's pitch.

Equation 4: Single Intermeshing Region Volume (for Instantaneous Step Size)

$$V_I = \frac{S_S}{4m}\left(r_E C_L \sin(\varphi) - \frac{2A_S\varphi}{\pi}\right)$$

Equation 5: Single C-chamber Volume (for Instantaneous Step Size)

$$V_C = \frac{S_S(\pi - \varphi)}{m\pi}(\pi r_E^2 - A_S)$$

Equation 6: Total Free Volume (for Instantaneous Step Size)

$$V = S_S(A_b - 2A_S)$$

Equation 7: Screw Cross-sectional Area

$$A_S = m(\varphi C_L^2 - C_L r_E \sin(\varphi)) + \frac{m\alpha(r_E^2 + (C_L - r_E)^2)}{2}$$

Equation 8: Barrel Cross-sectional Area

$$A_b = 2(\pi - \varphi)r_E^2 + c_L r_E \sin(\varphi)$$

It should be pointed out that for the case of flightless screw elements (i.e. spacers), Equation 6 can still be used if '$A_S = \pi r_I^2$' is substituted instead, where '$A_S = \pi r_I^2$' is the volume of the screw shaft.

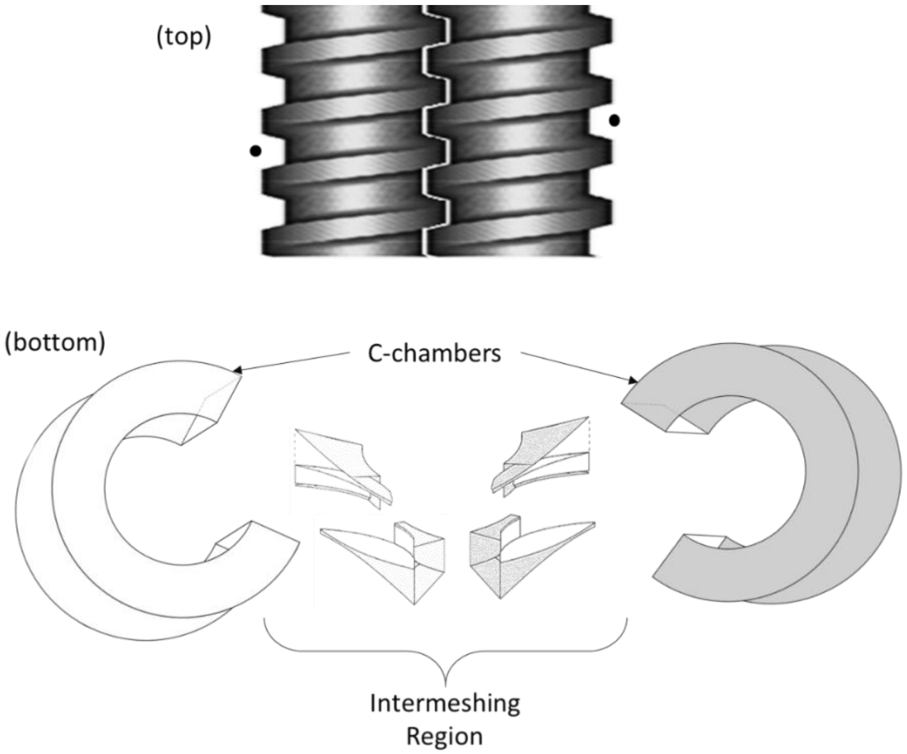

Figure 5: Schematic of screw channels in an intermeshing twin-screw extruder – pair of conveying screw elements under consideration (indicated by dot) (top), c-chamber and intermeshing region sub-volumes in screw channel (bottom)

Other important variables with regard to the definition of a screw channel are its width and depth. For the generalized model proposed by Vergnes et al. (1998), the width of the C-chamber portion was assumed to be independent of channel depth and equivalent to the maximum width (W_C) of the screw channel. This is a relatively reasonable assumption when screw elements are shallow. The equation for c-chamber channel width can be seen in Equation 9 (Potente et al. 1990). In this equation, e represents the flight land width and can be calculated using Equation 10 below.

Equation 9: Maximum Channel Width

$$W_C = \frac{B\cos(\beta)}{m} - e$$

Equation 10: Flight Land Width

$$e = \frac{B\alpha \cos(\beta)}{2\pi}$$

For certain calculations, there is a need to approximate the width of the intermeshing region (W_I). To facilitate this, an approximation proposed by Vergnes et al. (1998) is used, and can be seen in Equation 11. This approximation is based on the results from a three-dimensional analysis of the intermeshing region, and yields satisfactory values.

Equation 11: Equivalent Intermeshing Region Width

$$W_I = W_C - \alpha r_E \sin(\beta)$$

The average depth of a C-chamber screw channel ($\bar{h}$) may be obtained from the integration of the depth function proposed by Booy (1978). To further understand this integration, the screw channel should be visualized in yet another plane, as depicted in Figure 6 below. From this figure, channel depth naturally varies in the cross-channel direction (the z-direction), but through a mathematical transformation (Booy 1978), it is made to vary with an arbitrary angle (θ). Before calculating, it should be understood that the screw channel is composed of zero volume and non-zero volume sections, and that integration occurs over its non-zero portions. This calculation is also made easier by utilizing the fact that screw channels are symmetric and consequently, are independent of whether the calculation is performed on half the screw channel, or over its entirety.

To begin the calculation, the screw channel portion labelled 1 to 3 in Figure 6 is considered (for reasons stated above) and needs to be separated into two sections to facilitate accurate integration. The first section to be integrated is that found between points 1 and 2. The function describing this portion is shown in Equation 12 (Booy 1978), and the integration takes place over the range $0 \leq \theta \leq 2\varphi$. The second section to be integrated lies between points 2 and 3. In this section, the channel depth is maximum and constant over the range $2\varphi \leq \theta \leq \left(2\varphi + \frac{1}{2}\alpha\right)$. The equation for maximum channel depth is found in Equation 13 (Lafleur 2014, p. 118). Summing up the results from the integrations performed for those two sections, the average depth can finally be obtained by dividing the summation by the integration range, $2\varphi + \frac{1}{2}\alpha$. A composite equation for this calculation is shown in Equation 14.

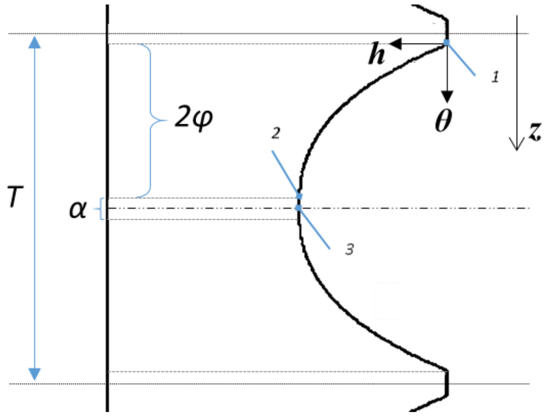

Figure 6: Cross-section of screw channel perpendicular to axial flow

Equation 12: Channel Depth (0 ≤ ϑ ≤ 2φ)

$$h_{12} = r_E(1 + \cos(\theta)) - \sqrt[2]{C_L^2 - (r_E \sin(\theta))^2}$$

Equation 13: (Maximum) Channel Depth (2φ ≤ ϑ ≤ ½(4φ+α))

$$h_{23} = (2r_E - C_L)$$

Equation 14: Composite Equation for Average Channel Depth

$$\bar{h} = \frac{\int_0^{2\varphi} \left(r_E(1 + \cos(\theta)) - \sqrt[2]{C_L^2 - (r_E \sin(\theta))^2} \right) d\theta + (2r_E - C_L)\, {}^{\alpha}/_{2}}{2\varphi + {}^{\alpha}/_{2}}$$

After the average channel depth has been obtained, the average internal screw radius (r_I) can be computed. This relationship is shown in Equation 15.

Equation 15: Internal Screw Radius

$$r_I = r_E - \bar{h}$$

The final geometry equation relevant to the design of a plasticating, twin-screw extruder simulator is one that describes the barrel surface that a screw channel contacts. This equation yields the total barrel surface area (S_{Ab}) for a pair of complementary screw elements, for a given step-size. To facilitate this calculation, the equation proposed by Booy (1978) is utilised and shown in

Equation 16. Again, the surface area calculations are performed on the sectionalized screw profile and thus, the instantaneous step-size (S_s) is used in favour of the element's pitch (B).

Equation 16: Barrel Surface Area for Complementary Screw Element Pair (for Instantaneous Step Size)

$$S_{Ab} = 4r_E(\pi - \varphi)S_s$$

2.1.2.2. Shape Factors

Shape factors are important dimensionless parameters that are used to correct variables affected by any simplifying geometry assumptions that have been imposed on a system of interest. While not strictly a geometry calculation, such variables are indispensable because they permit the evaluation of a much simpler problem without compromising on the accuracy of the obtained results. Several simplifications needed to be made due to the inherently complex geometry of a screw channel. This is particularly the case for the Navier-Stokes Equation, which is used to describe fluid flow through the C-chambers of the screw elements. The major geometry-associated assumption made is that the screw channels are wide enough to facilitate negligible flight effects on the fluid flow. Because this assumption is understandably flawed, shape factors have been added for mollification. There are two types of shape factors that are applicable to the Navier-Stokes Equation – shape factors for correcting drag contributions to net flow (f_d) and shape factors for correcting pressure contributions to net flow (f_p). For each case, the specific values used were obtained from Figure 7, which was created based on the data from Heldman et al. (2006, p. 803) and Tadmor & Klein (1978, p. 216 - 217).

Another common simplification to extruder systems is the assumption of negligible curvature effects and straight channel walls (i.e. C-chambers are likened to rectangular flow channels). Application of this assumption allows use of the Navier-Stokes Equations written in Cartesian coordinates, the most straightforward of the three most frequently used orthogonal coordinate systems (the others being cylindrical and spherical coordinates). When making such assumptions, corrections for curvature and 'obliqueness' are necessary. Such correction factors are not required for models developed using cylindrical coordinate systems, as is the case with the Vergnes et al. (1998) model. Regardless, the shape factors for correcting these assumptions may be found in Heldman et al. (2006, p. 804 - 805), and Tadmor & Klein (1978, p. 220 - 221, 303 - 304).

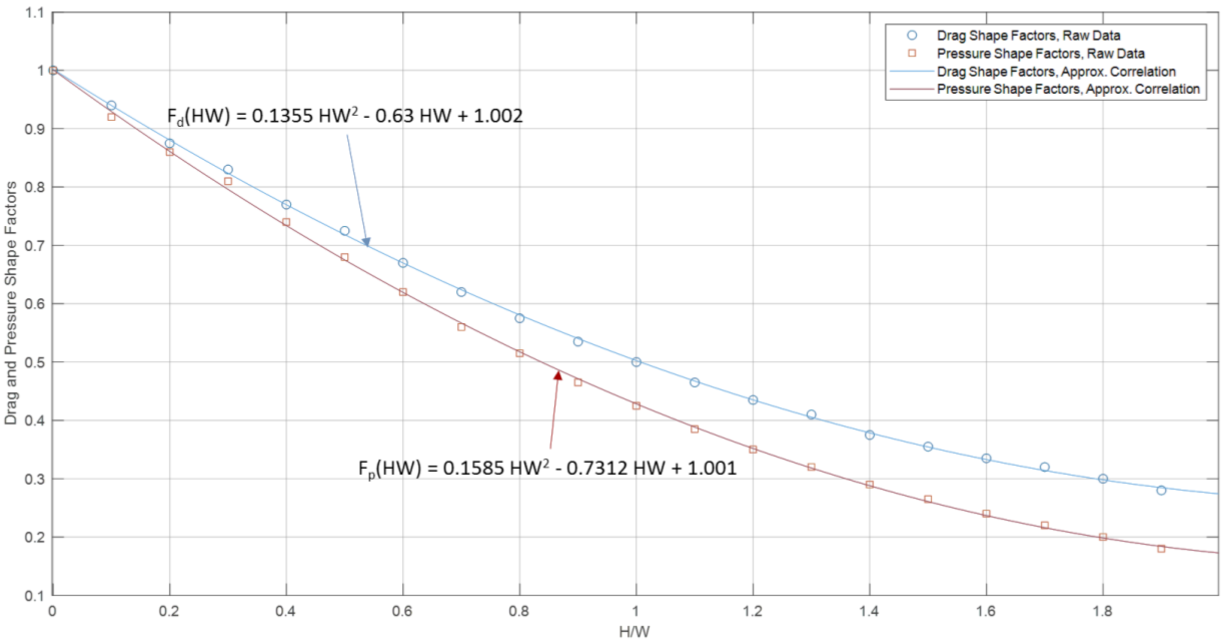

Figure 7: Shape factors for flight effects on channel flows

2.1.3. Pressure, Filling Ratio and Residence Time

2.1.3.1. Pressure, Pressure Drop and Pressure Gradient

2.1.3.1.1. Solid Conveying

Although the Vergnes et al. (1998) model acknowledges the existence of the solids conveying region in plasticating twin-screw extruders, the algorithm does not make use of equations and correlations specifically developed for solids transport. Consequently, the topic of solids conveying in twin-screw extruders will not be discussed in this review. However, information on this topic could be found in the work of Tadmor and Klein (1970) p. 49 - 78, Lovegrove and Williams (1973), and Orisaleye and Ojolo (2018).

2.1.3.1.2. Liquid Conveying

C-Chamber

As discussed in the previous subsection, the Navier-Stokes equation is indispensable when it comes to describing material flows. In the work of Vergnes et al. (1998), the cylindrical formulation of this equation is used to assess the flow of materials in a C-chamber. A schematic showing the specific coordinate orientation used can be seen in Figure 8. Due to the difficulty associated with the solution of the complete set of Navier-Stokes Equations, several simplifying assumptions were made. The first major assumption is the steady-state assumption, which implies time independence of the variables. The second set of assumptions regard the velocity components that are thought to be more significant for this problem. It is generally assumed that the velocities in the down-channel or θ-direction (v), and the cross-channel or z-direction (w), are more impactful than the velocity in the radial or r-direction. Consequently, radial velocities are assumed negligible and equal to zero. Both the down-channel and cross-channel velocities are assumed to only vary with the radius of the screw channel. Such assumptions were also made by Tayeb et al. (1988). The third assumption mandates that all densities and viscosities are constant within the screw section under current evaluation, and lastly, the extruder's screws are assumed to be stationary while the barrel rotates.

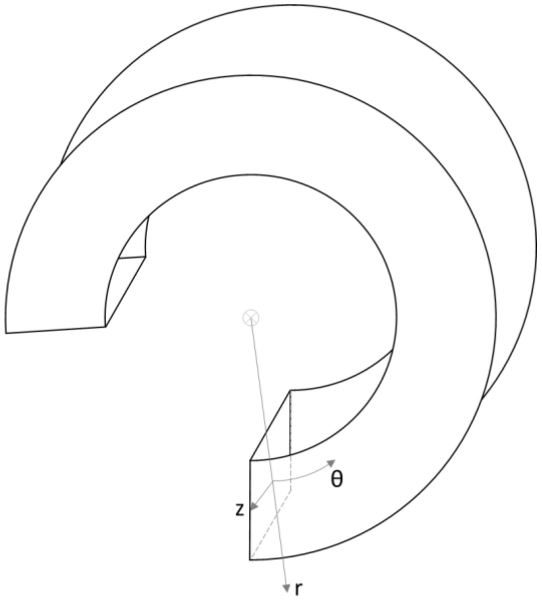

Figure 8: Schematic of C-chamber

From the above stated assumptions, the cylindrical formulation of the Navier-Stokes Equation may be simplified and solved to obtain the velocity equations shown in Equation 17 and Equation 18 for the down-channel and cross-channel directions (v_C and w_C correspondingly). The details of this integration can be found in Tayeb et al. (1988). It should be pointed out that the expressions $'\omega\, r_E \cos(\beta)'$ and $'\omega r_E \sin(\beta)'$ are the barrel velocity components in the down-channel and cross-channel directions respectively. The variable 'ω' is the rotational speed of the barrel (rad/s), and can be calculated from '$\omega = 2\pi N$'.

Equation 17: Down-channel Velocity for C-chamber

$$v_C(r) = \frac{1}{2\eta_a}\frac{\Delta P_C}{\Delta \theta_C}\left[r\left(\frac{r_E^2 \ln\left(\frac{r}{r_E}\right) - r_I^2 \ln\left(\frac{r}{r_I}\right)}{r_E^2 - r_I^2}\right) + \frac{1}{r}\frac{r_E^2 r_I^2}{r_E^2 - r_I^2}\ln\left(\frac{r_E}{r_I}\right)\right] + \omega\, r_E \cos(\beta)\left[\frac{r_E}{r}\left(\frac{r - r_I^2}{r_E^2 - r_I^2}\right)\right]$$

Equation 18: Cross-channel Velocity for C-chamber

$$w_C(r) = \frac{1}{4\eta_a}\frac{\Delta P_C}{\Delta z_C}\left[r^2 - \left(\frac{r_E^2 \ln\left(\frac{r}{r_I}\right) - r_I^2 \ln\left(\frac{r}{r_E}\right)}{\ln\left(\frac{r_E}{r_I}\right)}\right)\right] + \omega r_E \sin(\beta)\left(\frac{\ln\left(\frac{r}{r_I}\right)}{\ln\left(\frac{r_E}{r_I}\right)}\right)$$

With the velocity expressions defined, equations for the down-channel and cross-channel direction volumetric flows (Q_{Cv} and Q_{Cw} correspondingly) can be obtained by integrating each of the abovementioned velocity expressions over the C-chamber areas that are perpendicular to their respective flow directions. The result of this integration can be seen in Equation 19 and Equation 20.

Equation 19: Down-channel Volumetric Flow for C-chamber

$$Q_{Cv} = f_d \frac{(\omega\, r_E \cos(\beta)) W_C r_E}{2}\left[1 - \left(\frac{r_I^2}{r_E^2 - r_I^2}\right)\left(\ln\left(\frac{r_E}{r_I}\right)\right)^2\right] - f_p \frac{W_C (r_E^2 - r_I^2)}{8\eta_a}\frac{\Delta P_C}{\Delta \theta_C}\left[1 - \left(\left(\frac{2 r_E r_I}{r_E^2 - r_I^2}\right)\ln\left(\frac{r_E}{r_I}\right)\right)^2\right]$$

Equation 20: Cross-channel Volumetric Flow for C-chamber

$$Q_{Cw} = f_d(\omega r_E \sin(\beta)) W_C r_E \left[1 - \left(\frac{1 - \frac{r_I}{r_E}}{\ln\left(\frac{r_E}{r_I}\right)}\right)\right] - f_p \frac{W_C}{4\eta_a} \frac{\Delta P_C}{\Delta z_C} \left[\frac{2}{3}(r_E^3 - r_I^3) - \left(\frac{r_E^3 + r_I^3 - r_I r_E^2 + r_E r_I^2}{\ln\left(\frac{r_E}{r_I}\right)}\right)\right]$$

From the above equations, η_a is the instantaneous (apparent) material viscosity and $\frac{\Delta P_C}{\Delta \theta_C}$ and $\frac{\Delta P_C}{\Delta z_C}$ are the down-channel and cross-channel direction pressure gradients respectively. The above-stated velocity and flow equations all play a vital role in the functioning of any extruder simulation software. However, according to the method used in Vergnes et al. (1998), only the flow equations are directly used in pressure and pressure drop calculations. In order to appropriately demonstrate their applications, it is useful to analyse a generalized version of the flow equation in tandem with the three possible states of the screw channel and hence, C-chamber. The generalized equation for C-chamber flow can be found in Equation 21. From this equation, the net flow is seen to depend on the contributions of both the drag ($\zeta_d \omega$) and pressure ($\zeta_p \frac{\Delta P}{\Delta \theta}$) flows, which are mainly influenced by the rotational speed of the barrel and the instantaneous pressure gradient respectively. Regarding the state of the screw channels in a twin-screw extruder, there are four possibilities. The first three concern the forward conveying screw element (conveying screw element hereafter) while the last regards the reverse conveying reverse screw element (reverse screw element hereafter).

Equation 21: Generalized Flow Equation for Conveying Screw Elements

$$Q = \zeta_d \omega - \left(\pm \zeta_p \frac{\Delta P}{\Delta \theta}\right)$$

1) For conveying screw elements, screw channels may be fully filled or partially filled. When screw elements are fully filled with molten material (the first state), net flow in the down-channel direction is due to the contributions of both the pressure and drag flows. The drag portion of the flow moves material towards the extruder's exit, while the pressure portion regulates itself to ensure that net flow is constant along the extruder's length. This means that when the drag flow exceeds the net flow ($\zeta_d \omega > Q$), an opposing back pressure

develops to negate the occurrence, and the overall contributions of pressure are negative. Conversely, the overall pressure contributions are positive when drag flow is unable to entirely meet the requirements of the net flow.

2) The second and third states occur when the conveying screw elements are not fully filled. When in this state, material movement in the down-channel direction is only due to 'drag flow' in the broadest sense, and consequently, pressure contributions are zero. This state applies to screw elements that are partially filled with molten material or granulated solids. It can generally be assumed that partially filled screw elements before the first restrictive element (i.e. reverse screw elements, kneading blocks) in the down-channel direction convey material in a solid form. Melting is assumed to occur instantaneously at the site of the first restrictive element and thus, all further down-channel screw elements (both fully and partially filled) must contain molten material.
3) For the reverse screw element (the final state), screw channels are fully filled with molten material. Drag flow entirely opposes the down-channel flow direction and negatively contributes to the net flow in the extruder. Consequently, to obtain a positive net flow in the down-channel direction, the overall pressure contributions need to be positive. This is demonstrated in Equation 22.

Equation 22: Generalized Flow Equation for Reverse Screw Elements

$$Q = \zeta_d(-\omega) - \left(-\zeta_p \frac{\Delta P}{\Delta \theta}\right)$$

To obtain values for the down-channel pressure drop and cross-channel pressure gradient of a C-chamber, the appropriate assumptions and numerical parameters have to be applied to the flow equations. Regarding the pressure drop calculation, the down-channel volumetric flow rate from Equation 19 (Q_{Cv}) is identical to the steady-state volumetric flow rate through the extruder (Q) from Equation 23 (where $\dot{m}$ is material mass flow rate and ρ is its density), while the C-chamber length in θ-coordinates ($\Delta\theta_C$) can be determined through Figure 4, or from Equation 24 . The viscosity (η) is the apparent viscosity of the material in the screw section immediately downstream. Regarding the cross-channel pressure gradient, material flow in the cross-channel direction is assumed negligible. As a result, the cross-channel flow (Q_{Cw}) in Equation 20 equals zero.

Equation 23: Volumetric Flow Rate

$$Q = \frac{\dot{m}}{\rho}$$

Equation 24: Length of C-chamber

$$\Delta\theta_C = 2\pi - 2\varphi$$

Intermeshing Region

The intermeshing region in a twin-screw extruder has a complicated geometry deserving of full three dimensional consideration. While this may be the case, such analyses can be impractical due to the time and resources that they require. To overcome this challenge, Vergnes et al. (1998) approximate the intermeshing region to a local restriction in which flow is due only to pressure. This approximation is reasonable since the screws in this region move in opposing directions with respect to each other, and may be inferred to have a drag-flow 'cancelling-out' effect. The equation used to describe flow through the intermeshing region is Equation 19 less the drag flow term. This is shown in Equation 25.

Equation 25: Volumetric Flow for Intermeshing Region

$$Q_{Iv} = f_p \frac{W_I(r_E^2 - r_I^2)}{8\eta_a} \frac{\Delta P_I}{\Delta\theta_I}\left[1 - \left(\left(\frac{2r_E r_I}{r_E^2 - r_I^2}\right)\ln\left(\frac{r_E}{r_I}\right)\right)^2\right]$$

For this equation, the volumetric flow rate through the intermeshing region (Q_{Iv}) is identical to the steady-state volumetric flow rate from Equation 23 above, and viscosity (η) is the apparent viscosity of the material in the screw section under consideration. In order to calculate the pressure drop of the intermeshing region (ΔP_I), the angular length ($\Delta\theta_I$) must be known, and can be obtained from Equation 26.

Equation 26: Length of Intermeshing Region

$$\Delta\theta_I = 2\varphi$$

Net Pressure, Pressure Drop and Pressure Gradient

For a single screw element, the average pressure drop (ΔP) is a combination of the C-chamber and intermeshing region pressure drops. The specific relationship used to carry out this calculation can be seen in Equation 27. From the bracketed term, it becomes obvious that the individual c-chamber and intermeshing region pressure drops are proportioned according to their respective volumes. The value from this calculation yields the pressure drop across the pair of complementary screw elements, like the pair described in Figure 5 above. Thus, In order to determine the pressure contributions of a single screw element, this value is halved. Lastly, when the calculation step-size (S_S) is not equivalent to the pitch (B) of a screw element, a scaling factor needs to be applied. This scaling factor is the step-size/pitch ratio appended to Equation 27.

Equation 27: Pressure Drop across a Single Screw Element

$$\Delta P = \frac{1}{2}\left(\frac{V_I \Delta P_I + V_C \Delta P_C}{V}\right) \times \frac{S_S}{B}$$

The average pressure gradient across the screw channel of a complementary pair of screw elements can be calculated from Equation 28. The numerator of this equation is the pressure drop across a single C-chamber, while the denominator ($2\pi - \varphi$) is the angular distance of half the screw channel, or the distance occupied by half the intermeshing region and one c-chamber. To calculate the pressure in the subsequent upstream screw element, Equation 29 is used. In this equation, P_{i+1} is the pressure in the current screw channel section under consideration, while P_i is the pressure in the screw element immediately upstream. Again, it should be pointed out that the downstream variables (with respect to a particular screw element) are always defined, and the upstream variables need to be back-calculated.

Equation 28: Pressure Gradient in Complementary Pair of Screw Elements

$$\frac{\Delta P}{\Delta \theta} = \frac{\frac{1}{2}\left(\frac{V_I \Delta P_I + V_C \Delta P_C}{V}\right)}{2\pi - \varphi}$$

Equation 29: Up-channel Pressure for Succeeding Pair of Complementary Screw Elements

$$P_i = P_{i+1} - \Delta P$$

With respect to the cross-channel pressure gradient, Equation 20 is utilized as mentioned in Section 2.1.3.1.2. Again for this calculation, net flow in the cross-channel direction is assumed negligible and equal to zero ($Q_{Cw} = 0$). This assumption facilitates the easy rearrangement and solution of Equation 20 for the cross-channel pressure gradient.

2.1.3.2. Residence Time

With respect to the C-chamber, the material residence time (t_R) is the amount of time that material spends within the figure-8 screw channel formed from a complementary pair of screw elements. This variable may be calculated in different ways (Vergnes et al. 1998), depending on the state of the C-chamber as described in Section 2.1.3.1.2. When screw channels are fully filled, residence time depends mainly on the material flow rate through the channel, as seen in Equation 30. This is the case for the fully filled conveying screw elements and all reverse screw elements. When screw channels are not fully filled, residence time depends mainly on the rotational speed of the barrel as seen in Equation 31 and Equation 32. It should be pointed out that the values for residence time obtained from the highlighted equations are relevant to the instantaneous step-size assessed.

As briefly mentioned above, the material in partially filled screw channels is either solid or liquid, and conveyed under zero-pressure conditions. However, it should be pointed out that while down-channel flow is due to a drag-like mechanism for both the solid and liquid phases of a material, the specific mechanisms are not identical. For the case of the screw channels that are partially filled with molten material, material is displaced by a pure drag mechanism originating from the motion of the barrel over the fluid. For the case of the screw channels that are partially filled with granular solids conversely, material is displaced by the rotation of the screw.

Equation 30: Residence Time for Fully Filled Screw Channel (Liquid)

$$t_R = \frac{V}{Q_{Cv}}$$

Equation 31: Residence Time for Partially Filled Screw Channel (Liquid)

$$t_R = \frac{2}{(\cos(\beta))^2} \frac{S_S}{\omega B}$$

Equation 32: Residence Time for Partially Filled Screw Channel (Granular Solids)

$$t_R = \frac{S_S}{\omega B}$$

2.1.3.3. Filling Ratio

Filling ratio (f_R) is a term used to describe the mass fraction of material in partially filled screws. The general equation used to do so can be seen in Equation 33 below, and may be adapted to the phase of the material in the screw channel. For instance, when the material is a granular solid, its bulk density may be used. For screw channels that are fully filled, the filling ratio always equals unity. Lastly, the value for filling ratio obtained from the above-stated equation is only relevant to the instantaneous step-size assessed.

Equation 33: Filling Ratio for Partially filled Screws

$$f_R = \frac{\dot{m} t_R}{\rho V}$$

2.1.3.4. Flow Diagram for Pressure, Residence Time and Filling Ratio

The equations from Section 2.1.3 may be organized to form a flow diagram to assess the pressure, pressure drop, residence time and filling ratios for any screw element. The proposed algorithm is summarized in Figure 9, and is based off the rational provided in Vergnes et al. (1998).

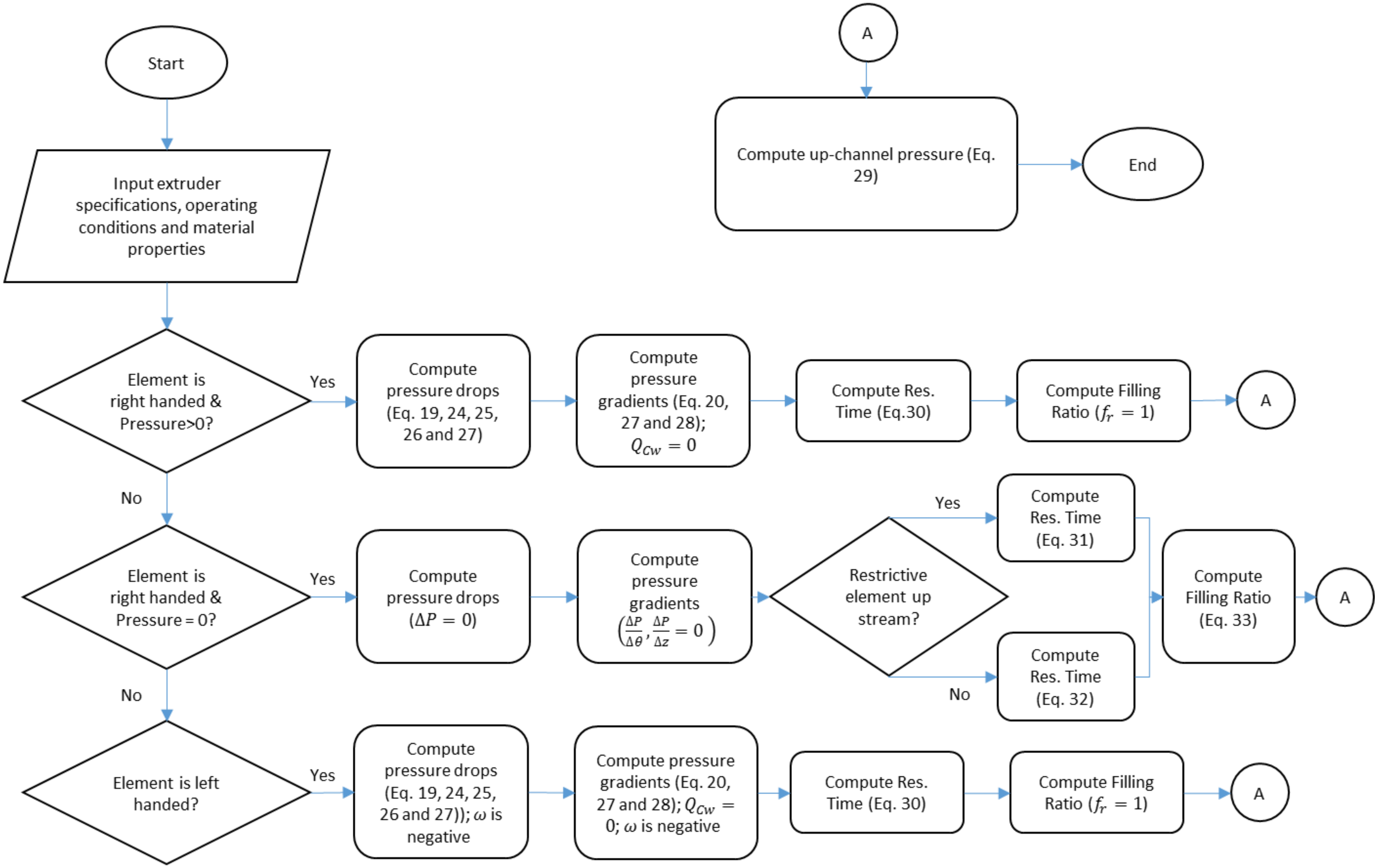

Figure 9: General Algorithm for the pressure, residence time and filling ratio calculations of the TSE Function

2.1.4. Strain Rate, Viscosity, Power, Heat Transfer and Temperature

2.1.4.1. Strain Rate, Viscosity and Power

To complete the global model for the twin-screw extruder, the behaviour of the processed material needs to be known. This is accomplished by measuring the shear stress/strain behaviour of the material and fitting the result to the appropriate rheological model. There exist several different types of rheological models, a summary of which is shown in Figure 10 below. Of the group, the most commonly encountered are those describing the behaviour of purely viscous materials. A material is described as purely viscous when the shear stress from its deformation depends only on the deformation rate (i.e. the average strain rate) at the instance of application. In such models, the shear stress (τ) is related to the deformation rate ($\dot{\gamma}$) through the viscosity of the material (η) as seen in Equation 34 below. The viscosity of a purely viscous fluid may be constant, but may also vary with the instantaneous deformation of the material. When viscosity is constant, the material is referred to as 'Newtonian'. On the other hand, when viscosity varies with the deformation rate, the material is described as 'non-Newtonian' (Dantzig & Tucker, 2001, p. 191-207; Kohlgrüber, 2008, p. 35-55).

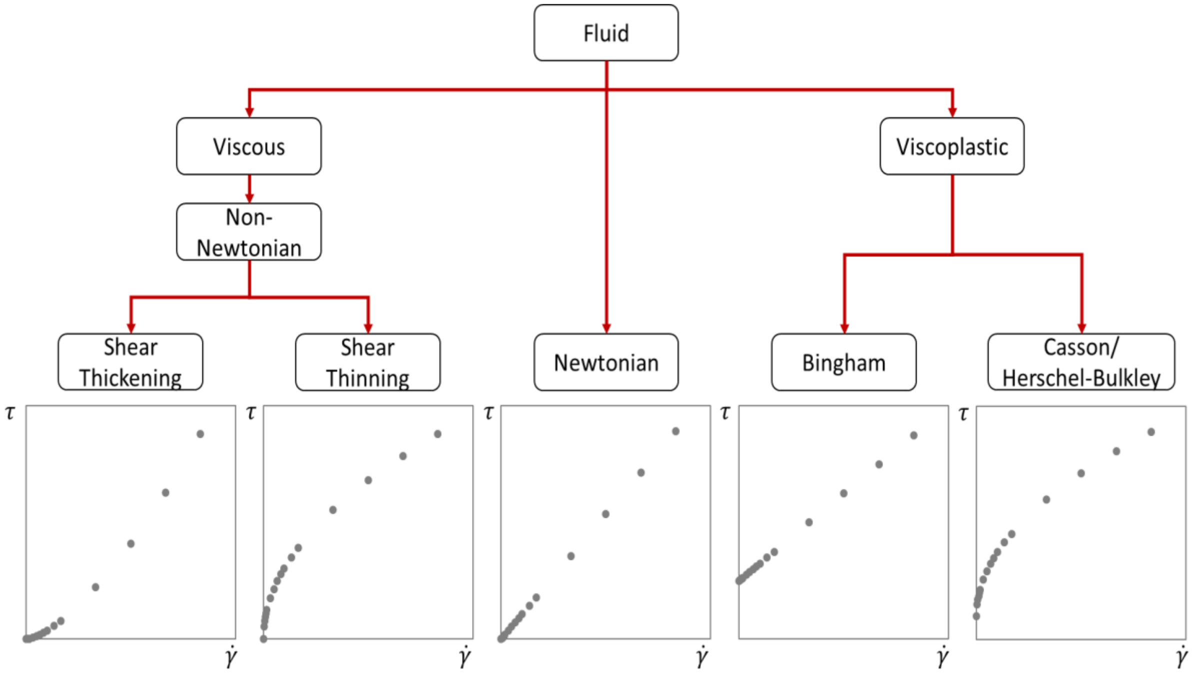

Figure 10: Summary of Common Rheological Models for Various Solids and Fluids

Equation 34: Generalized Relationship between Shear Stress and Average Strain Rate (Deformation rate)

$$\eta(\gamma) = \frac{\tau}{\dot{\gamma}}$$

The simplest rheological model is the Newtonian flow model for which shear stress and strain rate are proportioned by a constant value of viscosity. Unfortunately, many of the materials processed by twin-screw extruders are not Newtonian in nature, and require more accurate but complicated models to adequately describe their flow behaviour. To resolve this problem, a method based off of the concept of an equivalent Newtonian viscosity is applied. The term ‘equivalent Newtonian viscosity’ refers to the Newtonian viscosity that yields the identical flow rate that would be obtained for a specific non-Newtonian fluid under comparable temperature conditions, for a fixed geometry. This concept can be found in the literature when computing power was limited, and was developed by Broyer et al. (1975). In this work, Broyer et al. established a polynomial expression that yielded this equivalent viscosity value when the fluid temperature and wall shear stress was supplied (Broyer 1975; Broyer et al. 1975).

Since Broyer’s work, several variants of this approximating method have been developed and applied to extrusion systems. Of particular interest is the method described in Vergnes et al. (1998). In this paper, Vergnes et al. summarizes the method used to find a representative viscosity value for the molten material in a single C-chamber (i.e. the apparent viscosity or an average C-chamber viscosity). This method is fundamentally equivalent to that proposed by Broyer (1975), and only differs in the manner in which the viscosity value is calculated. To determine this mean C-chamber viscosity, the average strain rate of the fluid must be known, and is obtained from the second invariant of the deformation tensor of the molten material. For the assumptions made in Section 2.1.3.1 and Equation B.7-2 from Bird et al. (2001, p. 849), the second invariant of the deformation tensor ($\dot{\gamma}$) can be seen in Equation 35. Expressions for the necessary velocities have been presented in Section 2.1.3.1.2 (Equation 17 and Equation 18), and may be differentiated to obtain the necessary velocity gradients. The average strain rate ($\dot{\bar{\gamma}}$) can be found by subsequently integrating Equation 35 over the volume of the C-chamber, and by dividing the obtained result by its respective volume. The final expression can be found in Equation 36, which has been simplified by eliminating cancellable constants (i.e. channel width and angular length) (Vergnes et al. 1998). More details on this technique may be found in Szydlowski & White (1988) and Wang & White (1989), although the specific application differs to that proposed by Vergnes et al. (1998).

With the average strain rate (and other relevant parameters) defined, the apparent C-chamber viscosity can be found from the choice of non-Newtonian flow model selected. A common model of choice is the Ostwald–de Waele relationship (or the power law model) for shear thinning fluids, which is shown in Equation 37. Viscosity is also assumed to be dependent on the instantaneous temperature of the c-chamber, and solicits the use of the Arrhenius Equation shown in Equation 38. The final expression for viscosity can be found in Equation 39 (Vergnes et al. 1998) for which K_n and n are the material's consistency and flow behaviour index respectively, while T is the instantaneous temperature of the material in the screw channel and η_a is the apparent viscosity. The variable $K_{n,0}$ is the consistency at which measurements were taken at a given reference temperature T_{ref}, and $\frac{E}{R}$ is the ratio of activation energy-to-universal gas constant for the material.

Equation 35: Strain Rate (for Specified Assumptions)

$$\dot{\gamma} = \left(\left(\frac{dv}{dr} - \frac{v}{r}\right)^2 + \left(\frac{dw}{dr}\right)^2\right)^{\frac{1}{2}}$$

Equation 36: Average Strain Rate (for Specified Assumptions)

$$\dot{\bar{\gamma}} = \frac{2}{r_E^2 - r_I^2}\int_{r_I}^{r_E} \left(\left(\frac{dv}{dr} - \frac{v}{r}\right)^2 + \left(\frac{dw}{dr}\right)^2\right)^{\frac{1}{2}} rdr$$

Equation 37: Apparent Viscosity for Ostwald–de Waele Relationship

$$\eta_a = K_n \dot{\bar{\gamma}}^{n-1}$$

Equation 38: Arrhenius Equation

$$K_n = K_{n,0} exp\left[\frac{E}{R}\left(\frac{1}{T} - \frac{1}{T_{ref}}\right)\right]$$

Equation 39: Apparent Viscosity for Temperature-Dependent, Ostwald–de Waele Fluid

$$\eta_a = \left(K_{n,0} exp\left[\frac{E}{R}\left(\frac{1}{T} - \frac{1}{T_{ref}}\right)\right]\right)\dot{\bar{\gamma}}^{n-1}$$

After viscosity has been calculated, the viscous dissipation or power consumption (P_w) of fully filled screw channels can be approximated using Equation 40 (Stevens, 1985, p. 329; Guy, 2001, p. 56). It should be pointed out that the viscous dissipation calculations are performed on the instantaneous step-size volume being assessed. While this expression yields satisfactory results, more accurate expressions are available for this calculation (Vergnes et al. 1998, 2001).

Equation 40: Viscous Dissipation

$$P_w = \eta \dot{\gamma}^2 V$$

In the strictest sense, the strain rate, (apparent) viscosity and viscous dissipation equations listed above only describe the fluid flow behaviour in the C-chamber portions of screw channels, and ignores that of the intermeshing region. While neglect of the intermeshing region may change the simulation's predictions, its contributions are expected to be near-negligible due to its small size and correspondingly small weighting during volumetric averaging.

2.1.4.2. Heat Transfer

As stated in Vergnes et al. (1998), one of the major challenges faced during the application and solution of the thermal balance equation to screw channels is the choice of the barrel heat transfer coefficient (screws are often assumed adiabatic). Proper selection of this function is crucial as it greatly influences the rate at which the extruded material loses heat and consequently, the final material temperature profile obtained. While several correlations for heat transfer coefficient have been developed (Farid, 2010, p. 815-820; Rahman, 2009, p. 771-772), there are two major correlations that are often solicited (Guy, 2001, p. 66-67) – that by Todd (1988) seen in Equation 41, and that by Skelland (1958) seen in Equation 42.

Equation 41: Todd's Heat Transfer Coefficient Correlation

$$h_{Tb} = 0.94 \frac{k}{2r_E}\left(\left(\frac{(2r_E)^2 N\rho}{\mu}\right)^{0.28}\left(\frac{C_p\mu}{k}\right)^{0.33}\left(\frac{\mu}{\mu_w}\right)^{0.14}\right)$$

Equation 42: Skelland's Heat Transfer Coefficient Correlation

$$h_{Tb} = 4.9 \frac{k}{2r_E}\left(\left(\frac{(2r_E)s\rho}{\mu}\right)^{0.57}\left(\frac{C_p\mu}{k}\right)^{0.47}\left(\frac{(2r_E)N}{s}\right)^{0.17}\left(\frac{(2r_E)}{L}\right)^{0.37}\right)$$

In the above equations C_p and k are the material's heat capacity and thermal conductivity respectively, while L denotes the length of the twin-screw extruder. The material speed inside the extruder (s) can be found from the product of the frequency of rotation (N) and the screw element pitch. The viscosity of the molten material at the wall (μ_w) can be found by evaluating Equation 35 at the condition $r = r_E$ and substituting the result into Equation 39.

2.1.4.3. Average Material Temperature

The general thermal balance for the section of an arbitrary pair of complementary screw elements has been presented by Vergnes et al. (1998) for fully filled screws, and is shown in Equation 43. In this equation, $\dot{m}$ is the steady-state mass flow of the material, and h_{Tb} and h_{Ts} are the heat transfer coefficients between the barrel and molten material, and screw and molten material respectively. The barrel and screw surface areas are correspondingly denoted by S_{Ab} and S_{As}, while the average material temperature (material temperature hereafter) is denoted by T. The barrel temperature (T_b) is obtained from a user specified function which describes the temperature variations of the barrel with axial location along the extruder.

Before Equation 43 could be used, a few modifications needed to be made. For the first modification, the extruder screws are assumed adiabatic, which results in a zero value heat transfer coefficient between the material and screw. When this assumption is applied, Equation 43 can be rearranged to yield Equation 44 and thus, the average temperature change across the assessed step-size, ΔT. The second modification is the addition of the filling ratio term to Equation 44 (Barrès et al. 1991). This modification is necessary because it proportions the heat loss and viscous dissipation P_W terms according to the mass fraction of fluid present, and allows for the application of Equation 44 to partially filled screw channels.

Equation 43: General Thermal Balance for Complementary Screw Element Pair

$$\rho C_p \dot{m} \cdot \Delta T = h_{Tb}(T_b - T)S_{Ab} + h_{Ts}(T_s - T)S_{As} + P_W$$

Equation 44: Temperature Change for Complementary Pair of Screw Elements

$$\Delta T = \frac{(h_{Tb}(T_b - T)S_{Ab} + P_W)f_R}{\rho C_p \dot{m}}$$

With these modifications applied, the temperature change across the complementary screw element section can be easily obtained and substituted into Equation 45. In Equation 45, T_{i+1} is the temperature of the screw channel section under current investigation, while T_i is the temperature of the screw element immediately upstream. Again, it should be pointed out that the downstream variables (with respect to a particular screw element) are always defined, and the upstream variables need to be back-calculated.

Equation 45: Up-channel Temperature for Succeeding Pair of Complementary Screw Elements

$$T_i = T_{i+1} - \Delta T$$

As discussed earlier, there exist several screw channel states, each of which deserving special consideration. From Section 2.1.3.1.2, c-chambers may be fully or partially filled in conveying screw elements, or fully filled in reverse screw elements. Additionally, partially filled screws may convey material in a granular or molten state.

1) For the case of conveying screw elements that are fully filled with molten material, the equations presented above may be applied without modification (Equation 35 to Equation 45). The value of filling ratio in Equation 44 is unity.
2) The same equations hold for the case of the reverse screw element, with one exception. Since the barrel appears to move in the opposite direction, a negative rotational speed should be used when calculating the velocity and velocity gradients necessary for the average strain rate. Again, the value of filling ratio in Equation 44 is unity.
3) When screws are partially filled, there exist three different subcases.
    a. If the conveying screw elements are partially filled and there are restrictive elements upstream, the material being conveyed is in a molten state and the above presented equations may be used without modification. When there are no restrictive elements upstream but screw channels are under pressure, the material's thermal behaviour is still considered. Thus, the equations stated above may be used without modification. For both sub-cases, filling ratio is given by Equation 44, and does not equal unity.

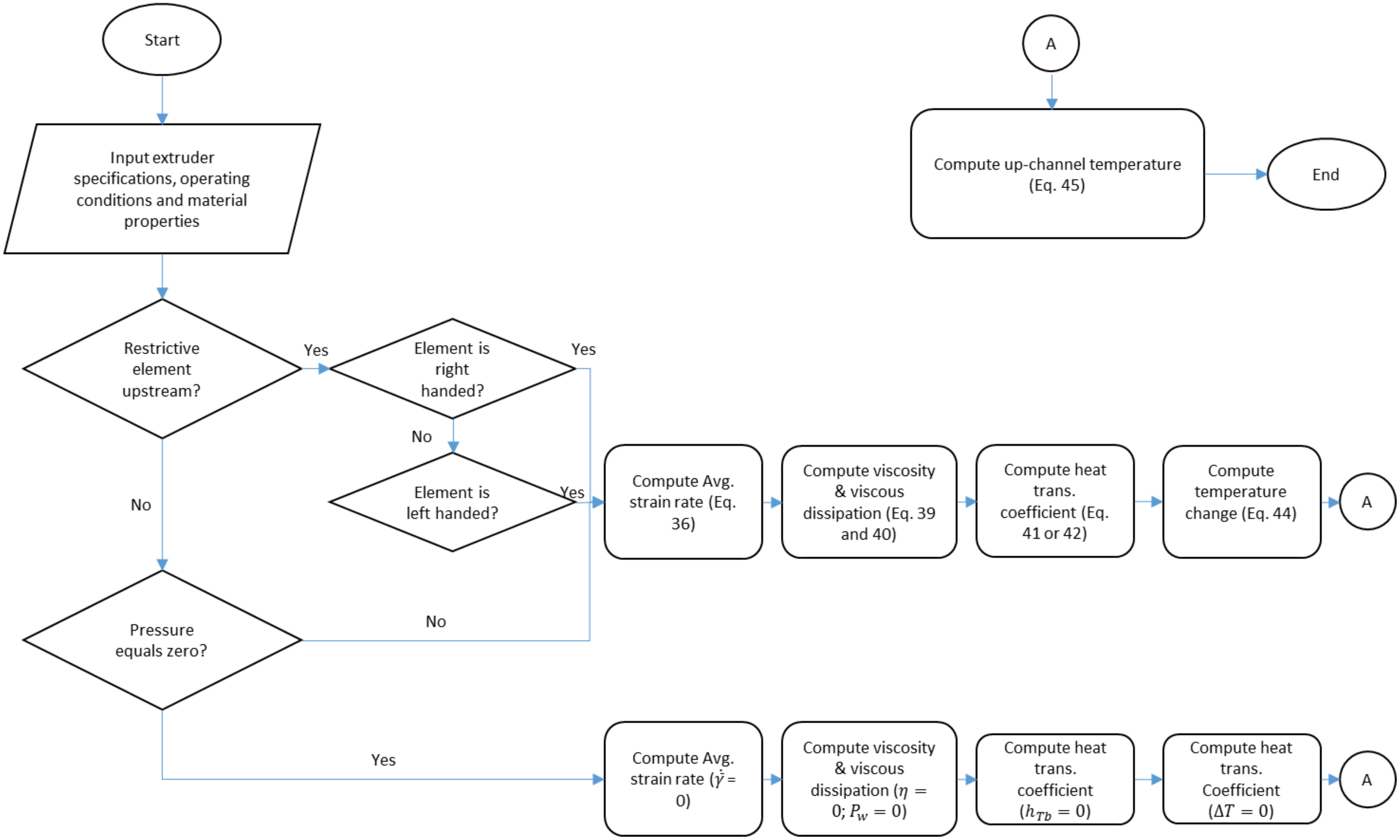

Figure 11: General Algorithm for the viscosity, viscous dissipation and temperature calculations of the TSE Function

b. In the final subcase, there are no restrictive screw elements upstream and the material is conveyed under zero pressure conditions. These properties correspond to the conveyance of granular solids whose energy contributions are ignored. Consequently, viscosity, viscous dissipation, heat transfer coefficient and temperature change are assigned null values.

2.1.4.4. Flow Diagram for Strain Rate, Viscosity, Power, Heat Transfer and Temperature

The equations from Section 2.1.4 may be organized to form a flow diagram to assess strain rate, viscosity, power, heat transfer and temperature for any screw element. The proposed algorithm is summarized in Figure 11, and is based off the rational provided in Vergnes et al. (1998).

2.1.5. Expression in Twin-screw Extruders

Screw presses are variants of extruders that focus on the separation of a liquid from a solid/liquid mixture through mechanical compression. Such mixtures are subjected to substantial forces that cause the solid matrix to compress (consolidation), and liquid to flow from the matrix through a permeable barrel section (expression) (Shirato et al. 1986; Bouvier and Campanella 2014, p. 363-367). Screw presses are commonly used to extract oils and juices from seeds, fruits and vegetables, and provide high quality extracts. However, this method achieves only moderate extraction yields (about 80% for the case of oil extractions), and results in significant product loss. One method used to minimize product loss is through process optimization using models. There are three major classes of models that have been developed to describe consolidation and expression in a screw press (Venter et al. 2007; Willems et al. 2008). The first class of models are empirical models that have been developed from performance data. While such models can be accurate, their applications are limited to the specifications of the device and the material properties of the feed they process, making them inflexible. The second class of models are those based on the cell structure of the feed material. Such models are highly insightful, but are complicated and expensive since they require knowledge of difficult to measure cellular structures and dimensions. The last class of models are those based on the consolidation theory originally proposed by Terzaghi (1943). Such models are more versatile and require parameters (i.e. densities, viscosities, compression ratios and consolidation coefficients) that are cheaper and easier to measure, unlike the classes discussed prior. The flexibility and affordability of the consolidation model class makes them a very popular method for modelling consolidation in phase separating extruders, and the technique has been modified to include more complicated scenarios (i.e. when variability during consolidation is significant) (Shirato et al. 1978, 1982, 1983, 1985; Westenbroek 2000; Bouvier and Campanella 2014, p. 363-375). Regardless, all consolidation models find their basis in Terzaghi's work, which will be discussed in detail in Section 2.2.3.2.

2.2. Review of Fibrous Biomass

Plant-based fibrous biomasses are utilized in many different industries and disciplines, particularly in manufacturing and engineering. The following subsections investigate the handling of natural fibres in the areas of material science and geotechnical engineering. However, before exploring the application of wood and its fibres on the aforementioned disciplines, the most pertinent biological and anatomical properties are reviewed and discussed.

2.2.1. Wood Fibres and their Properties

Trees are composed of three parts – the root, the stem and the crown– from which wood is obtained from the stem (Higuchi 2012, p. 1, 2). The stem of a tree has a few major roles, with the most major being the facilitation of material transport between the root and the crown. Water (and other dissolved minerals) enters the tree through the root and is a necessary raw material for photosynthesis, which occurs in the crown leaves. Consequently, a convenient transport means between the root and crown of a tree is required. The transport of water to the crown is achieved using the xylem (Campbell and Reece 2005, p. 584, 719; Higuchi 2012, p. 1). These structures make up both the heartwood and sapwood regions in mature trees as depicted in Figure 12, however only the sapwood portion participates in active water transport. Water is moved through the stem due to the synergetic collaboration of two occurrences – the transpiration pull and capillary action. Transpiration is the process through which trees release water vapour into the atmosphere through their leaves. As a tree transpires, it generates a negative pressure within itself which is termed the transpiration pull. The transpiration pull amplifies water movement via capillary action already taking place within the xylem cells. Weak attractive bonds between the water molecules and the xylem cause the water to 'stick' to the surface of the xylem (adhesion), while a slightly weaker attraction causes the water molecules to 'stick' to each other (cohesion). The continuous adhesion of water molecules to new xylem surface (while maintaining cohesion) causes water molecules to move up the xylem vessels via capillary action.

Although water is undoubtedly one of the most important fluids transported within a tree, it is not the only one. The transport of tree sap is of equal importance as it contains the sugars, proteins and nutrients required by the living tree cells for survival and growth. Sugars formed in the crown leaves are moved into the phloem and are transported throughout the plant as sap using the phloem vessels located near the bark of the tree as shown in Figure 12 (Campbell and Reece 2005, p. 584, 719; Higuchi 2012, p. 1). Unlike transport in the xylem, fluid transport in the phloem can take place in both directions and requires energy. The specific mechanism used for sap transport is called active transport. This form of transport moves sugars from regions of lower concentration (i.e. the leaves) to regions of higher concentration (i.e. the phloem, fruits and roots). The process through which material is moved from the leaves to other plant tissue is called translocation.

Another major function of the stem (along with the roots) is to aid in supporting and protecting the tree. To do this, the cell walls of the xylem are fortified with a durable, phenolic material called lignin, which is shown in Figure 13. This resistant lignin layer sandwiches an internal layer of interwoven cellulose bundles (called microfibrils) that are held in place by a hemicellulose-protein matrix. Together, the arrangement supports the weight of the tree, provides rigidity against the elements, and barricades against microbial and insect attacks. In general, wood is composed of 20% - 35% lignin, 40% - 50% cellulose and 15% - 30% hemicellulose (Higuchi 2012, p. 40 - 43).

There are several different types of vascular cells that a tree can produce based on its hardwood/softwood classification (Campbell and Reece 2005, p. 584, 719). Although this classification will be further explored in a subsequent subsection, the differences concerning the vascular cells will be discussed here. With respect to water transport, the xylem in hardwoods are typically a mix of tracheids and vessels, which are schematically depicted in Figure 13. Tracheids are thin, long, hollow cells which transport water through openings in their cell wall called pits. These cells, like vessel elements, do not contain cytoplasm and are therefore dead cells. Vessels are shorter and wider than tracheids, and are considered to be more developed water transport units as they facilitate easier liquid flow. In those structures, vessel elements align to form a continuous, internal cavity called a lumen through which water is transported. Unlike the hardwood xylem transport structure, the transport structure of softwoods contain no vessels.

Water transport is only achieved through tracheids, which result in the softwood timber having a smoother appearance than those of hardwoods when examined under a microscope.

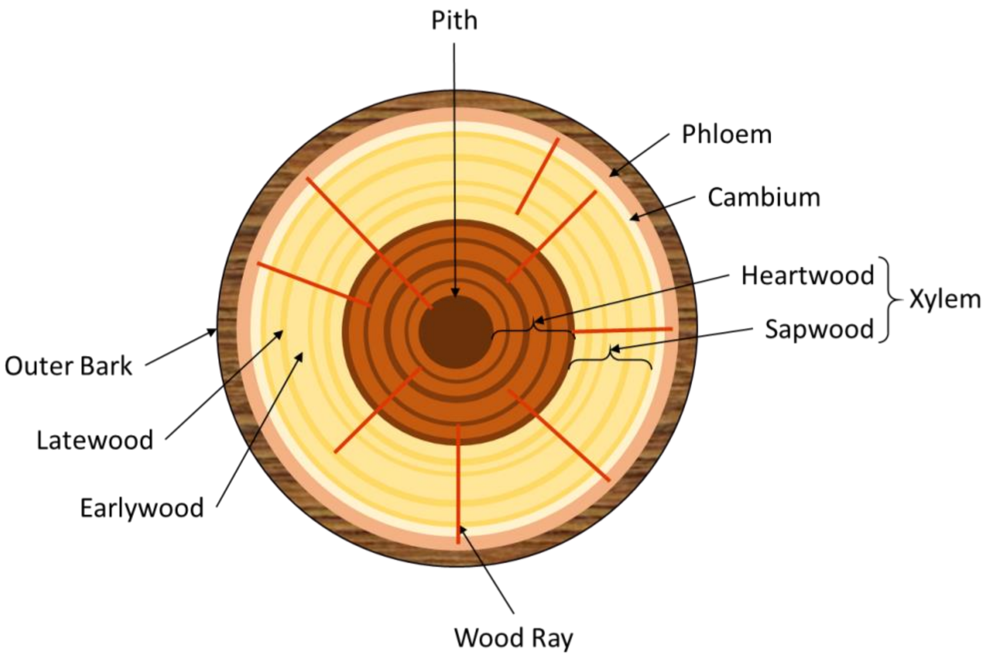

Figure 12: Anatomy of a tree stem from a temperate climate

The specific phloem network developed in a tree is also dependent on its hardwood/softwood classification. In hardwoods, sap is transported through the lumen of a series of continuously connected sieve tube elements. Each sieve tube element consists of a hollowed structure for sap conductance called the sieve tube member, and a companion cell which is believed to aide in the governance of the sieve tube member. In softwood, sap is transported through sieve cells. Like the tracheids, the sieve cells contain lateral openings called lateral sieve areas which allow sap to move from one cell to another. However like sieve tube members, governance of sieve cells is controlled by a second cell called an albuminous cell. Sieve tube members and sieve cells are externally maintained due to their unique protoplasm composition. These structures contain no nuclei despite being living, and need external assistance when performing cellular activities. Schematics of both sieve elements can be found in Figure 13.

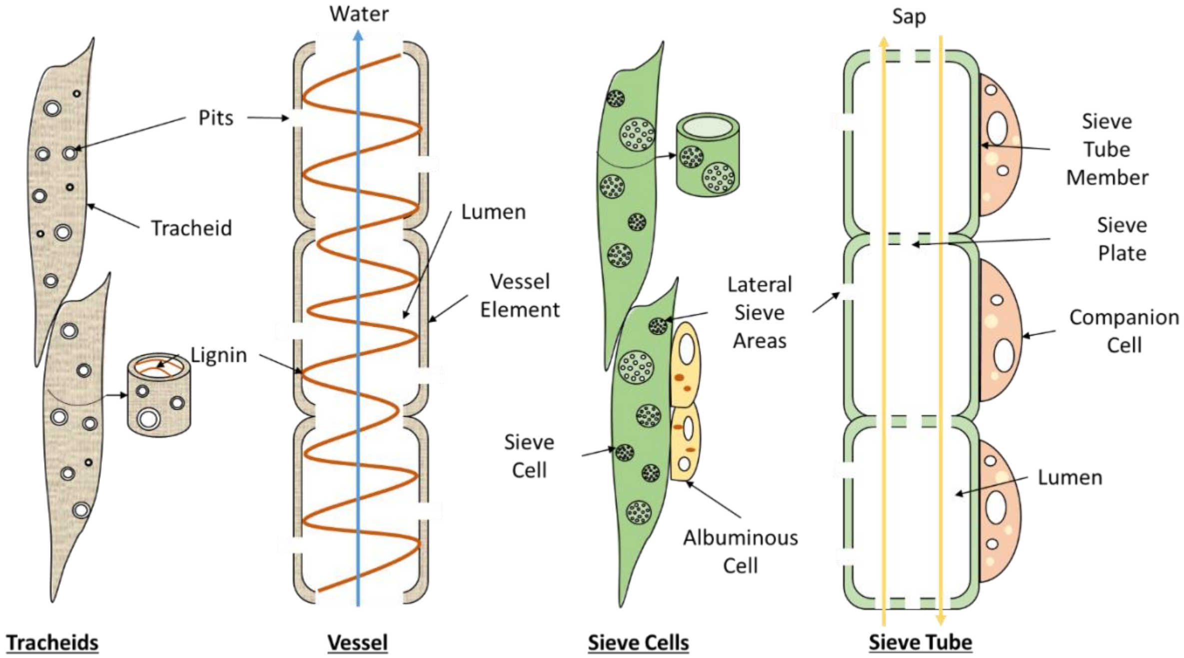

Figure 13: Types of vascular tissue cells in trees

2.2.1.1. Types of Wood

Trees do not consistently produce a single type of wood during their lifetimes. Although the properties of a tree's timber are primarily dictated by genetics, it can also be affected by external factors such as soil quality, climate (heat, precipitation, wind) and crowding (which causes competition for resources such as light) (Karth 1967, p. 168, 171; Kolleman and Cote 1986). Regardless, some generalities have been observed in the types of wood a tree can produce. Some of these types are shown pictorially in Figure 12, however the major classifications will be explored in depth in the subsequent sub-sections.

2.2.1.1.1. Hardwoods vs Softwoods

Woods are broadly classified into two major categories – hardwoods (deciduous, angiosperm) and softwoods (conifer, gymnosperm) (Ward and Simpson 2001, p. 2; Ross 2010, p. 3-2). Regarding botany, hardwoods come from plants that produce seeds which are enclosed in the ovary of a flower. Such trees are found in both temperate and tropical climates, and tend to have broad leaves that they shed during the winter and autumn seasons if present. Softwoods, on the other hand, are found in plants that produce seeds without producing a flower. Such trees are found in temperate climates, and have needle and cone type leaves that they keep during the summer and winter seasons. Regarding wood texture, hardwoods have a porous appearance as the wood contains both tracheids and vessels for water transport within the tree, as discussed in Section 2.2.1. Softwoods conduct fluids without the need for vessels and consequently, such woods have no visible pores. In general, hardwoods tend to be denser than softwoods, although a few exceptions exist. Common hardwoods include beech, mahogany, maple, oak and poplar, and common softwoods include cedar, Douglas fir, pine, spruce and redwood.

2.2.1.1.2. Heartwood vs Sapwood

Despite the specific softwood or hardwood classification, the trunk of a tree generally contains two very distinct regions – sapwood and heartwood (Kolleman and Cote 1986, p. 4, 168 - 173; Ward and Simpson 2001, p. 4; Campbell and Reece 2005, p. 725 - 727; Ross 2010, p. 3-2 - 3-3). Sapwood is the lighter-coloured band of wood located to the inner side of the cambium shown in Figure 12. This wood is mainly responsible for water and mineral transport to the crown, which is facilitated by the metabolically-inactive xylem. Throughout the xylem are regions of living cells called wood rays, which are also depicted in Figure 12. These areas are filled with cells that aid in the transport of material between the xylem and phloem, and also store starch and other organic materials. Hardwood is the darker-coloured wood found interior to sapwood. Although containing no living cells, heartwoods are formed and maintained by sapwood cells located at the heartwood/sapwood interface. The maintenance of heartwood cells involves the production and deposition of a variety of chemicals (called extractives) by the adjacent sapwood cells. Extractives include waxes, oils, gums and resins, and can fortify the heartwood (and its timber) by increasing its resistance to fungal decay and moisture. Additionally, extractives may imbue a heartwood with more superficial properties, such as an attractive colour or an aromatic scent. Although heartwood and sapwood exist in radial proportion in the trunk of a tree, it should be pointed out that those proportions are not constant throughout. The ratio of heartwood-to-sapwood can vary with a tree’s height and age, and may possess different material properties at those different locations or points in time.

Due to differences in cellular composition, it is only natural for heartwoods and sapwoods to have different properties. Regarding liquid absorption, a heartwood may have a lower affinity for liquids due to buildup of repellant extractives that are not present in its neighbouring sapwood counterpart. With respect to green wood density, the relationship between the two woods seems to be dictated by the water content of the sapwood, although exceptions have been observed. However, sapwoods are generally considered to have the higher green wood density due to their larger moisture contents.

2.2.1.1.3. Earlywood and Latewood

As mentioned in the previous sub-section, the heartwood portion of a tree is produced and maintained by the sapwood, particularly by those located at the heartwood/sapwood boundary. To replenish the lost sapwood however, trees generally produce new xylem layers near the bark region in the form of annual (or seasonal) growth rings (Kolleman and Cote 1986, p. 4 - 6, 173 - 179; Ward and Simpson 2001, p. 4; Campbell and Reece 2005, p. 725 - 727; Ross 2010, 3-4 - 3-7). The sapwood is produced by the cambium layer near the bark, depicted in Figure 12 (along with new phloem). The cambium produces two different types of sapwood – earlywood and latewood. Earlywoods are produced during the aggressive growth period, which typically occurs during the spring for trees growing in temperate climates. During this period, xylem cells with large cavities and thin cell walls are rapidly formed to facilitate efficient water transport for leaf re-growth after the winter season. As the summer season approaches, growth begins to slow down, and latewoods are formed. In contrast to those of the earlywood, the xylem of the latewood have smaller lumens, thicker cell walls and are darker in colour. They have greater densities and strength properties, and are produced to strengthen the tree stem. During the winter, the cambium is inactive and growth ceases.

2.2.1.2. Absorption

The interaction of wood fibres with water is an extremely crucial interaction, particularly when such fibres are used for structural applications. The water content of a piece of wood affects its density, in addition to affecting its volume and strength properties. However, such wood properties are only affected up till a critical point called the fibre saturation point. To further explain the fibre saturation point, the types of water in plant fibres should be understood. A schematic demonstrating the former can be seen in Figure 14 below.

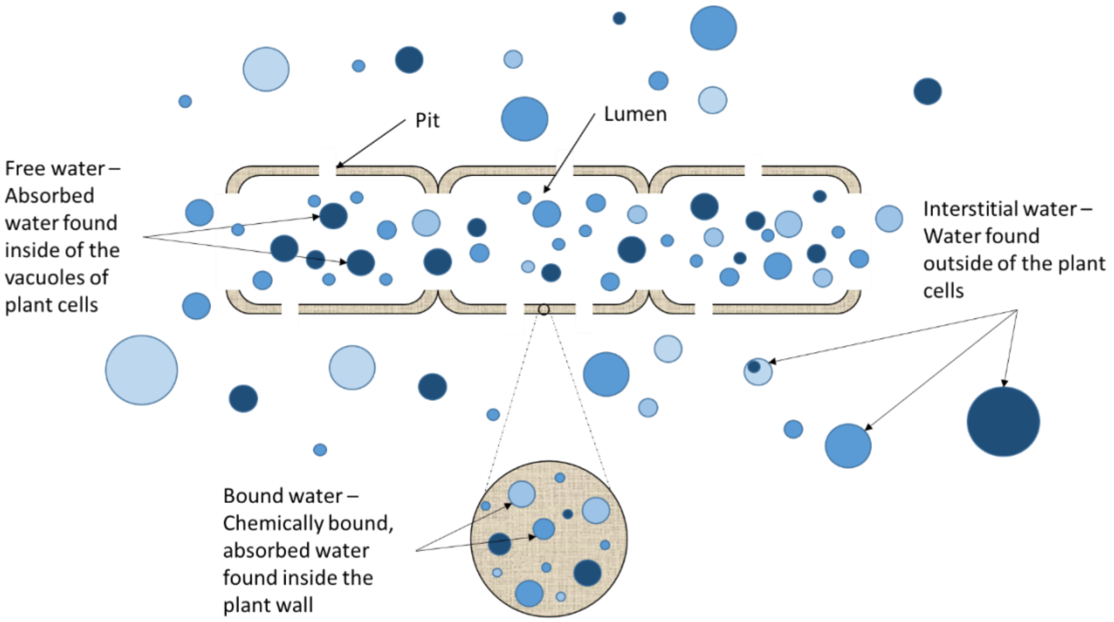

Figure 14: Types of water in a wet wood fibre suspension

As can be seen from Figure 14, there are three major types of water that can exist in a suspension of wood fibres (Westenbroek 2000; Ross 2010, p. 4-2 - 4-7; Bouvier and Campanella 2014, p. 357 - 359). The first type of water is the external water which exists outside the plant cells, and is called the 'interstitial water'. If completely dry wood fibres are added to an aqueous environment, some of the interstitial water moves into the xylem cells via osmosis and capillary action, and goes into saturating the cell walls and lumen of the fibres. The water that hydrates the cell wall is absorbed via osmosis. This type of water chemically interacts with the cell wall components, and is called 'bound water'. As the cell wall becomes saturated, the physical and mechanical properties of the fibres gradually change. The influx of water to the cell wall leads to volume increases due to swelling, while the overall strength of the wood fibres deteriorates. When the cell wall becomes saturated, the 'fiber saturation point' of the wood fibres is reached. At the fibre saturation point, there are no further changes to the volume and strength properties of the fibres. For most woods, the fibre saturation point occurs at a moisture content of about 30% $g_{water}/g_{dry\ fibre}$.

The water that enters the fibres through the pits and lumen is called 'free water'. As discussed in Section 2.2.1.1, free water is absorbed through capillary action and it exists within the xylem free of chemical interaction. Capillary action is the primary means of water absorption in wood, and it is affected by the number of open-ended tracheids and vessels in the wood sample. For example, absorption by a solid wooden block is much greater when the grain end is exposed to moisture due to greater lumen exposure from open-ended xylem structures. The rate of liquid absorption by capillary action is also affected by the rate at which the absorbed water can displace air from the wood samples. When both the cell wall and cell interior are saturated, the maximum moisture content of wood fibres can range from 44% $g_{water}/g_{dry\ fibre}$ to 267% $g_{water}/g_{dry\ fibre}$, depending on the plant species hydrated (Ross 2010, p. 4-3).

The rate at which water is absorbed by wood fibres can be modelled using several different transport models, although these models are often times complex and numerically intensive for many practical situations (Candanedo and Derome 2005). To eliminate this problem, researchers have developed correlations relating easily measurable parameters with those less easy to quantify. One of the most popular correlations describing water absorption in wood is that proposed by Krus & Kunzel (Candanedo and Derome 2005; Noorolahi et al. 2008; Lepage 2012; Okoh 2014), shown in Equation 46. This correlation is a lumped parameter model which relates the mass of liquid absorbed per unit area (m_a) to the square root of the soak time (t_R) using a liquid absorption coefficient (k_{asb}). Although the absorption coefficient of wood is strongly dependent on the specific wood species, the coefficient tends to be larger for hardwoods than for softwoods since softwoods can be less efficient at water transport. This is due to the lack of vessels in the xylem structure of softwoods, as discussed in the previous subsection. In hardwoods, overall absorption coefficients of order of magnitude ranging from 10^{-4} kg/m^2·s$^{1/2}$ to 10^{-3} kg/m^2·s$^{1/2}$ have been reported (Noorolahi et al. 2008; Okoh 2014), while for softwoods, values as small as 10^{-10} kg/m^2·s$^{1/2}$ (Ross 2010, p. 4-4) and as large as 10^{-2} kg/m^2·s$^{1/2}$ (Candanedo and Derome 2005) have been observed.

Equation 46: Krus' & Kunzel's Correlation for Water Absorption Coefficient in Wood

$$m_a = k_{asb}\sqrt{t_R}$$

For a wooden block, the mass of water absorbed by the sample may be determined by multiplying the mass of liquid absorbed per unit area (obtained from Equation 46) with the water-exposed surface area. However for wood fibres, estimation of the fibre surface area is more challenging. A common means of estimating the average surface area of a fibrous bed is through the Kozeny-Carman Equation shown in Equation 47 (Westenbroek 2000). This equation relates the permeability of a fibrous bed (K) to its porosity (n_p), specific surface area (S_a) and a special coefficient called the Kozeny constant (k_{kc}), which equals 4.5 for a bed of randomly packed glass fibres. For a bed of glass fibres parallel to flow, the Kozeny constant is 3.07, while for a bed of glass fibres perpendicular to flow, the constant is 6.04 (Westenbroek 2000). The average surface area of the fibrous bed may be obtained from Equation 47 if its mass, permeability and porosity are known.

Equation 47: Kozeny-Carman Equation

$$K = \frac{n_p^3}{k_{kc} S_a^2 (1 - n_p)^2}$$

2.2.2. Fibrous Biomass in Material Applications

The processing of fibrous suspensions is a challenge faced in many major industries, such as the pulp and paper, textile, food and composites industries. Most of the challenges faced are related to two major factors - measuring device limitations, and extreme bulk property changes with variations in the mixture's constituents (Duffy 2006; Derakhshandeh et al. 2011). The following subsection summarizes some of the most relevant research carried out on fibre flow suspensions and their properties.

2.2.2.1. Flow Structures in Fibrous Systems

There exists several different types of structures in a system of flowing fibres, depending on the consistency (x_c) of the fibrous suspension (i.e. the mass fraction of dried fibers) (Kerekes et al. 1985; Duffy 2006). According to Duffy (2006), there are four major classes of 'particles' – free fibres, floccettes, flocs and networks. When suspension consistency is dilute ($x_c < 1\%$), the fibres of a suspension are generally not in continuous contact with each other, allowing large aspect ratio fibres to exist independently of the suspension. Such fibres belong to the 'free fibre' particle class and aid in drag reduction by interacting with eddies during turbulent flow. Those interactions mitigate a portion of this turbulent energy and in so doing, reduce the amount of energy wasted during flow. The consequence of these occurrences is a lowered energy/pressure requirement to transport a dilute suspension when compared to that necessary for only transporting the fluid component through the same system at identical velocities.

As the consistency of a suspension is further increased, fibres are progressively unable to flow without having interactions that form permanent or semi-permanent agglomerated structures (i.e. floccettes, flocs and networks). There are four major interactions that occur between the fibres of higher consistency suspensions – colloidal attractions, mechanical surface linking, elastic fibre bending and surface tension (Kerekes et al. 1985). Fibre interactions classified as colloidal refer to the electrostatic and electrokinetic attractions that occur between small fibres. The strength of those forces generally depends on inter-fibre proximity, the materials of which the fibres are composed, and the type of surface modification chemical used (if any). Mechanical surface linking is more predominant in suspensions with contorted fibres from bends, kinks and curves, or fibres with highly fibrillated surfaces. As the fibres in such suspensions collide, the irregularities in there structures do not allow them to be easily detached, and leads to the formation of linkages. The strength of those linkages depends on the extent of contortion, and the flexibility and material strength of the composing fibres. Linkages through the elastic bending of a fibrous network occur at the contact points between adjacent fibres in a suspension. Bent network fibres produce a normal force at the points where they contact other fibres, inducing internal stresses within the fibre network. Since the surface of the fibres are not frictionless, friction forces also develop at those points. In combination, the two work to keep contacting fibres coupled, the extent to which depending on the surface property of the fibres. A pictorial summary of mechanical surface linking and elastic fibre bending can be seen in Figure 15. The final class of particle interaction is that related to surface tension, which occurs when the consistency of a suspension is high enough that undissolved gas bubbles exist. These gas bubbles introduce surface tension to the suspension, which supports structural cohesion. Of the four classes of particle interactions, mechanical surface linking was the most influential interaction regarding flocculation and the formation of permanent or semi-permanent structures in fibrous suspensions.

The weakest agglomerated flow structure in a fibrous system is the floccette, which is a collection of mutable, loosely woven fibres. Because they exist at low consistencies, opportunities for interactions are scarce, resulting in their continuous formation, dissolution and reformation during flow. This dynamism is thought to imbue flowing suspensions with unique viscoelastic effects. A further increase to the consistency of a fibrous suspension results in the formation of flocs. Like floccettes, flocs are a cluster of fibres that develop during flow. However, they differ from floccettes since they have mechanical strength, have a mean size, and are 'permanent' flow structures. Floc formation is primarily due to mechanical surface linking, and is the most common flow structure encountered in fibre processing systems. The last type of particle is the network, and it is formed from flocs that have developed a very large interfloccular strength. Networks generally conform to the shape of the vessel within which they flow, and are the reason why fibrous suspensions require the application of a minimum amount of shear before flow begins (the flow shear should be large enough to overcome the interfloccular strength of a network so flocs can be dislodged and transported).

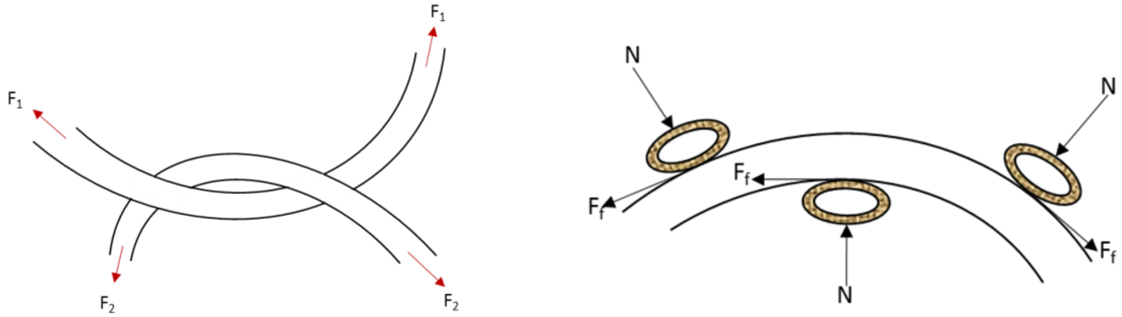

Figure 15: Mechanical surface linking (left) and elastic fibre bending (right) in fibrous suspensions

Although consistency is a major factor affecting the dominant particle in a fibrous system, there are instances where all four particles exist at the same time. Best examples of this coexistence can be found in suspension/pipe flow studies in which drag reduction is frequently observed during turbulent flow, irrespective to the consistency of the fibrous suspension (Duffy 2006; Derakhshandeh et al. 2011).

2.2.2.2. Flow Regimes in Fibrous Systems

The flow regimes of fibrous suspensions has been detailed in the work of Sumida (2013) who carried out several experiments using acrylic test pipes of varying diameters and a variety of dilute bleached Kraft pulp suspensions. From his experiments, Sumida identified the presence of five different flow regimes, which have been pictorially summarized in Figure 16. The first three flow regimes detail the suspension’s behaviour during laminar flow, while the last details the suspension’s behaviour during turbulent flow. The fourth flow regime occurs at laminar/turbulent transitioning.

The first flow regime occurs at the critical point at which the supplied stress is just enough to overcome the yield stress of a static fibrous suspension. At that instance, the system exists in a state of limiting equilibrium, in which a dynamic friction force (related to the yields stress of the suspension) is generated between the suspension and the wall, and stops the suspension from flowing. If a slight amount of stress is additionally supplied, the system enters the second flow regime. In this regime, flow commences and a very small water annulus forms at the pipe wall due to particle migration away from the high-shear regions of the system. Flow is dictated by both the dynamic friction forces (from the wall/ fibre interactions) and viscous forces (from an excess of interstitial liquid near the wall). A further increase to supplied stress causes the system to enter the third and final regime in which laminar flow is prevalent. In this regime, the water annulus near the wall is well defined, and the centrally-migrated fibres are conveyed through plug flow. Flow is primarily dictated by viscous forces due to the absence of fibres near the pipe wall.

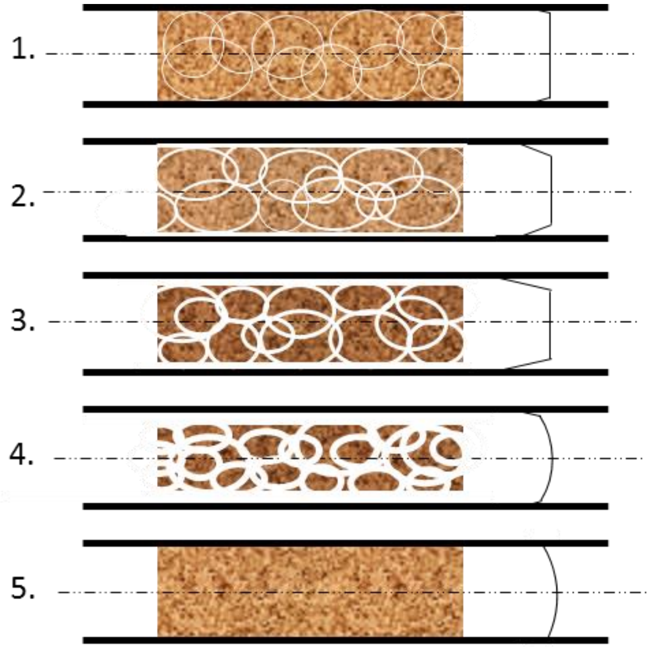

Figure 16: Flow regimes for pipe-flowing fibrous suspensions

In general, the water annulus of the third flow regime will continue to grow with an increase in supplied stress to the system. The additional stress goes into compressing the fibrous plug at the pipe's core, which expands the annulus. Eventually, the system reaches a point when the fibrous core can no longer be compressed, and any additional stress supplied causes core disintegration to occur at the annulus/core boundary. At this instance, the structured flow which dominated the first three flow regimes is disrupted as surface fibres from the fibrous core begin to move into the water annulus, indicating laminar/turbulent transitioning. This occurs at applied stresses about equivalent to four times the yield stress of the fibres. If enough stress is supplied to cause the complete disintegration of the fibrous plug, then the fifth and final flow regime is reached. The suspension in this regime experiences full turbulent flow and significant mixing, and shows drag reduction due to eddy dampening from the suspended fibres. This behaviour is observed at applied stresses in excess of ten times the yield stress of the fibres.

While the maximum suspension consistency assessed was 3%, higher consistencies are known to exhibit a similar behaviour, although requiring more significant energy inputs (due to larger yield stresses) and with greater regime transition delays. When the yield stress required to initiate flow cannot be achieved, the fibrous suspensions exhibit plug flow (Derakhshandeh et al. 2011; Sumida 2013).

2.2.2.3. Models for Fibrous Suspensions and Apparent Viscosity

As observed by numerous authors (Leong-poi and Allen 1992; Derakhshandeh et al. 2011; Sumida 2013; Daoxing and Hong 2016), fibrous pulp suspensions require the application of a minimum amount of stress before flow can commence. When in the turbulent flow regime, a fibrous suspension is fluidized and able to 'flow'. Its rheological behaviour is governed by a class of models called the yield stress fluid models, the three most common being the Bingham, Herschel-Bulkley and Casson models shown in Equation 48 to Equation 50. In those equations, τ is the applied shear stress, τ_0 is the yield stress and $\dot{\gamma}$ is the average strain rate. The variables η, K and n are viscosity, consistency (rheological) and flow behaviour index, respectively. The apparent viscosity may be obtained by dividing the shear stress from either of those models by the average shear strain rate applied. As an example, the apparent viscosity for the case of the Herschel-Bulkley Model is shown in Equation 51, where η_a is apparent viscosity and $\dot{\bar{\gamma}}$ is the average strain rate.

Equation 48: Bingham Model

$$\tau = \tau_0 + \eta\dot{\gamma}$$

Equation 49: Herschel-Bulkley Model

$$\tau = \tau_0 + K\dot{\gamma}^n$$

Equation 50: Casson Model

$$\sqrt{\tau} = \sqrt{\tau_0} + \sqrt{\eta\dot{\gamma}}$$

Equation 51: Apparent Viscosity for Herschel-Bulkley Model

$$\eta_a = \frac{\tau_y + K_n\dot{\gamma}^n}{\dot{\gamma}}$$

Although numerous investigations have been carried out on the rheological properties of wet fibres, it should be pointed out that not many complete studies exist, particularly for the case of high consistency suspensions. It is for this reason the work of Daoxing and Hong (2016) has been highlighted an summarized in Table 2. The study provides the complete rheological parameters of the Herschel-Bulkley model for unbleached Kraft pulp fibres over a large consistency (dry fibre mass fraction) range.

Table 2: Herschel-Bulkley model parameters for unbleached Kraft pulps at various consistencies (Daoxing and Hong 2016)

Consistency	τ_y (Pa)	K_n (Pa s^n)	n (s^{-n})
0.1146	371	136	0.120
0.1428	416	149	0.100
0.1904	466	181	0.090
0.2380	529	201	0.085
0.2720	706	230	0.081
0.3173	853	263	0.070

2.2.3. Fibrous Biomass in Geotechnical Applications

2.2.3.1. Material Properties

Significant insight on the engineering properties of woody biomasses can be inferred from peaty soil literature (Mesri and Ajlouni 2007; Kazemian et al. 2011; Bell 2013) due to their physical similarities. Peats are a soil type that contain a significant portion of partially humified and disintegrated plant remains. Such soils are usually acidic in nature, and are produced when fallen plant material is anaerobically decomposed by the local soil microflora. The anaerobic decomposition of the plant material is facilitated by the presence of a water saturated environment, which restricts oxygen accessibility. There generally exists two classes of peaty soils: fibrous peats and amorphous peats. Due to its greater commonality with woody biomass, the subsequent review will focus primarily on the properties of fibrous peats. However, some discussion of amorphous peats will be provided.

Fibrous peats generally refer to peats in which plant elements (such as stems, leaves and root fragments) are fairly distinguishable. The dimensions of such plant elements typically range from 20 μm to 1200 μm in length, 100 μm to 1200 μm in width, and 10 μm to 15 μm in thickness (Landva and Pheeney 1980; Mesri and Ajlouni 2007). Unlike amorphous peats, fibrous peats tend to be surficial and subjected to smaller overburden pressures (Lea and Brawner 1963). This results in fibrous peats generally having lower ash percentages than amorphous peats. The ash percentage of a peaty soil is the mass percentage of inorganic residue that remains after complete combustion of a sample. This value ranges from 2% to 50% and generally increases with the ground sampling depth (Bell 2013). Additionally, ash percentage is also greatly affected by the geographic location from which the sample is obtained. While this property is not directly relevant to wood fibre processing, the ash percentage of a peaty soil can significantly affect other peat properties such as compressibility.

2.2.3.1.1. Permeability

The permeability of soil is a measure of its fluid-transmitting capacity. This property is dependent on the soil's void ratio (the ratio of interstitial void volume to solid matrix volume), and the average size and shape of the flow channels formed from its constituent elements. In general, the soil permeability increases with an increase in void ratio (or porosity) and with an increase in the number of large, straight flow channels within its matrix. Alternatively, soil hydraulic conductivity can be used to describe the ease with which water is transmitted within the soil. In addition to soil permeability, the hydraulic conductivity depends on the density and viscosity of the flowing liquid. Fibrous peats are characterized by a large, initial hydraulic conductivity (Mesri and Ajlouni 2007). This is primarily due to the presence of large voids within the soil (consequent from the small overburden pressures attributable to shallow depths), and the very porous nature of the composing organic material. The initial hydraulic conductivity of fibrous peats typically ranges from 10^{-7} m/s to 10^{-4} m/s, while that of amorphous peats can be as small as 10^{-8} m/s (Lea and Brawner 1963; Huat et al. 2014). For fibrous peats, these values correspond to permeabilities ranging from 10^{-11} m^2 to 10^{-8} m^2 if the permeating fluid is water at 20°C.

2.2.3.1.2. Compressibility

While the initial permeability of fibrous peat is considerably large at low pressures, it quickly decreases with the application of moderate loads due to its extreme compressibility. The soil compressibility is evaluated by measuring the volume change that occurs due to an applied change in its overburden pressure. The large compressibility of fibrous peats arises from several distinctive peat properties related to the nature and orientation of its organic content (Lea and Brawner 1963; Mesri and Ajlouni 2007; Huat et al. 2014). While variations exist between different plant types, the organic portion of a peaty soil is in itself compressible due to its material composition and the hollowness of its constituting fibres. Additionally, the average fibre alignment within the soil has been shown to influence peat compressibility (as well as other parameters such as permeability) due to the anisotropic nature of the fibrous network (Yamaguchi et al. 1985a, b; Mesri and Ajlouni 2007). The large peat compressibility is also attributed to the very large initial permeabilities and void ratios of this specific soil. The initial void ratio for fibrous peats can be as high as 25, while that for amorphous peats can be as high as 9 (Bell 2013).

The consolidation of a peaty soil involves several stages (Coduto 1999). The first consolidation stage, denoted as primary consolidation, occurs when the vertical pressure on a steady state soil sample is suddenly increased. During this process, the volume of voids in the soil is continuously reduced and the pore fluid is continuously expelled. This process continues until the soil matrix is compressed enough to completely support the additional vertical pressure and enter a new steady-state. After primary consolidation is completed, significant settlement can still be experienced in some soils without the application of additional vertical pressures. This type of consolidation is denoted secondary consolidation, and occurs as a result of creep, particle rearrangement and the decomposition of soil organics. With respect to the extrusion pre-treatment of woody biomasses, the primary consolidation behaviour of fibrous peats is most relevant. This behaviour is characterised by the compression index when the vertical pressure on the soil is increased, and by the recompression index when the vertical pressure is decreased. Due to the wide variability in the composition and equilibrium rest states of fibrous peats, the compression and recompression coefficients can show great variation. However, the recompression index-to-compression index ratio for fibrous peats has been found to range from 0.1 to 0.3 (Mesri and Ajlouni 2007).

2.2.3.1.3. Friction Coefficient (Inter-Particle)

The shear strength of soil is a measure of its resistance to failure. In geotechnical engineering, failure occurs when shear planes form within a soil, causing internal slippage. While several different theories have been developed to explain this phenomenon, the Mohr-Coulomb theory (Coduto 1999; Das 2009) is most widely utilised. According to this theory, material failure only occurs for critical combinations of soil pressure and shear stress, which can be collectively described as the failure envelope for the material. The failure envelope can be approximated by a straight line, permitting mathematical description through the Mohr-Coulomb Failure Criterion. In this criterion, critical shear stresses are related to their respective critical pressures through an intercept and a proportionality constant. The intercept is termed cohesion, and indicates the soil strength when subjected to an applied pressure equal to zero. Cohesion is attributed to the attractive electrostatic and electromagnetic forces between soil particles, or the result of chemical reactions. The proportionality constant is termed the coefficient of internal friction, and provides a relationship between the shear stress and applied pressure at soil failure. For fibrous peats, the coefficient of internal friction typically ranges from 0.700 to 1 when measured using the direct shear box method, and 0.839 to 1.732 when measured using the triaxial shear method. These values correspond to angles of internal friction ranging from 35° to 45° and 40° to 60° respectively (Mesri and Ajlouni 2007). The coefficient of friction of fibrous peats is quite high when compared to that of other more common geotechnical materials. This is attributed to extensive particle interlocking between the high tensile strength fibres that compose the peat. The magnitude of the coefficient of internal friction has also been found to depend on the average orientation of the fibres within test samples due to the anisotropic nature of the soil matrix (Yamaguchi et al. 1985a, b; Coduto 1999; Mesri and Ajlouni 2007).

2.2.3.2. Terzaghi’s Consolidation Theory (for Primary Consolidation)

Terzaghi’s one-dimensional consolidation theory was developed by Karl von Terzaghi, and describes the relationship between stresses (pressures) in a soil (Fredlund and Rahardjo 1993, p. 419; Coduto 1999, p. 422 - 434; Osipov 2015, p. 35). To develop this theory, Terzaghi acknowledges the existence of three stresses – total stress (σ), effective stress (σ') and pore water pressure (u_w) – the relationship between which can be described by Equation 52. This equation shows that the external stresses applied to a soil (i.e. the total stress) are completely opposed by the counteracting solid stresses (i.e. the effective stress) and liquid pressures (i.e. the pore water pressure) in a soil. When in equilibrium, the pore water pressure and effective stress both work to oppose the current total stress, and equal it. If this equilibrium is disrupted (typically by an event increasing the externally applied pressure on a saturated soil to a new, constant value), the change in total stress initially generates an excess pore water pressure within the soil (in addition to the existing pore water pressure) of equal but opposite magnitude. Due to the porous nature of soil and the presence of an excess pore water pressure, water continuously drains from the soil site. While the continuous loss of water causes a continuous reduction in the excess pore water pressure, the effective stress experiences a continuous increase which equals the excess pore water pressure already dissipated. As the effective stress increases, the soil skeleton compresses, resulting in settlement. This process continues until all the excess pore water pressure is dissipated and a new equilibrium state is reached. In the end, the pore water pressure in the soil is unchanged, however the effective stress is increased by an amount equal to the change in total stress. It should be pointed out that if the derivative of Equation 52 is taken, an expression relating changes in pore water pressure (i.e. excess pore water pressure) to changes in effective stress is obtained. This expression is shown in Equation 53.

Equation 52: Terzaghi's Consolidation Theory

$$\sigma = \sigma' + u_w$$

Equation 53: Terzaghi's Consolidation Theory (differential form)

$$d\sigma' = -du_w$$

Naturally, Terzaghi's one-dimensional consolidation theory plays a major role in the development of his one dimensional consolidation equation, along with several major assumptions. To start, Terzaghi assumes that a fully saturated soil may be considered a homogenous continuum composed of solid soil particles and liquid water. Both phases are assumed incompressible, and both flow and consolidation are assumed to occur in the vertical direction. The flow of fluid through the soil is assumed to follow Darcy's law, which states that the rate of flow through a porous medium is equal to the product of hydraulic gradient, the cross-sectional area through which the flow is occurring and the intrinsic hydraulic conductivity of the medium. Lastly, soil characterizing coefficients such as permeability and the coefficient of volume compressibility are assumed constant throughout the consolidation process.

The derivation of Terzaghi’s Consolidation equation begins by acknowledging a sustained, instantaneous increase in the external pressure on an infinitesimal soil volume. As mentioned earlier, this change in the externally applied pressure is entirely resisted by a corresponding increase in pore water pressure initially (i.e. the excess pore water pressure). The elevated pore water pressure gradually dissipates to its original value as water begins to flow out of the control volume, as depicted in Figure 17. Based on this theory, it is evident that the rate of volume change of the soil element with time is only dependent on the net flow of water from the control volume. As a result, the most intuitive first step to deriving Terzaghi’s model is a balance on the liquid entering and leaving the control volume. A liquid mass balance on the control volume reduces to a ‘volume balance’ due to the liquid phase incompressibility assumption made earlier. This yields Equation 54.

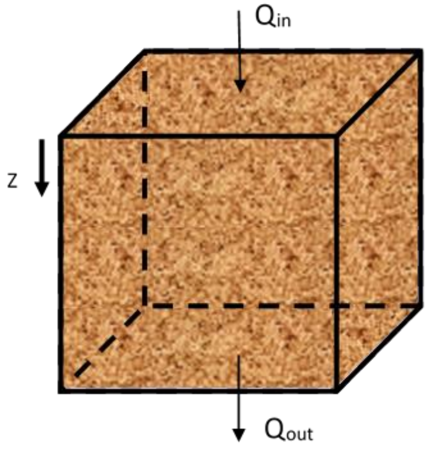

Figure 17: Control volume in saturated porous materials

Equation 54: Continuity on Expressed Liquid Phase

$$\frac{\partial V}{\partial t} = -\frac{\partial Q}{\partial z} dz$$

where V is volume, t is time, Q is flow rate and z is depth (vertical). Flow from the control volume may be related to instantaneous pressure through Darcy's Law which is shown in Equation 55. In this equation, k_v is hydraulic conductivity, h_w is hydraulic head, A_c is cross-sectional area, ρ_w is the density of water, g is acceleration due to gravity, u_w is pore water pressure, dx is discrete width and dy is discrete across length. The substitution of Equation 55 into Equation 54 yields Equation 56, which is the first expression for rate of volume change.

Equation 55: Darcy's Law

$$Q = -k_v\left(\frac{\partial h_w}{\partial z}\right)A_c = -k_v\left(\frac{1}{\rho_w g}\frac{\partial u_w}{\partial z}\right)dxdy$$

Equation 56: First Expression for Rate of Volume Change

$$\frac{\partial V}{\partial t} = \frac{k_v V}{\rho_w g}\frac{\partial^2 u_w}{\partial z^2}$$

The second expression for rate of volume change can be obtained from the constitutive relations for saturated soils. The first constitutive relationship of interest relates void ratio (e_r) to effective stress (σ') through the compression index (C_c) of the soil. In derivative form, this expression is given by Equation 57. Equation 57 also makes use of the relationship between changes in effective stress and changes in pore water pressure described in Equation 53.

Equation 57: Comprssibility Constutive Relationship

$$\partial e_r = -C_c \partial \log(\sigma') = C_c\frac{-\partial\sigma'}{\sigma' * \ln(10)} = C_c\frac{\partial u_w}{\sigma' * \ln(10)}$$

The second constitutive relation of interest is that relating void ratio to the volumetric strain of the soil. In derivative form, this relationship is given by Equation 58. Substitution of Equation 57 into Equation 58 and taking the time derivative of the resulting expression yields Equation 59, the second expression for rate of volume change.

Equation 58: Void Ratio/Volumetric Strain Constutive Relationship

$$\frac{\partial V}{V} = \frac{\partial e_r}{1 + e_r}$$

Equation 59: Second Expression for Rate of Volume Change

$$\frac{\partial V}{\partial t} = -\frac{C_c V}{(1 + e_r)(\sigma' ln(10))} \frac{\partial u_w}{\partial t}$$

The final step in developing Terzaghi's 1D consolidation equation is to equate Equation 56 and Equation 59. This yields Equation 60 in which C_v is the coefficient of consolidation, and is given by Equation 61. In Equation 61, the term m_v is the coefficient of volume compressibility, and it is defined in Equation 62. This parameter was obtained by collecting and simplifying the coefficients leftover from equating Equation 56 and Equation 59 (less k_v, ρ_w and g), and by substituting out C_c using Equation 57.

Equation 60: Terzaghi's 1D Consolidation Differential Equation

$$\frac{\partial u_w}{\partial t} = C_v \frac{\partial^2 u_w}{\partial z^2}$$

Equation 61: Coefficient of Consolidation

$$C_v = \frac{k_v}{(\rho_w g) m_v}$$

Equation 62: Coefficient of Volume Compressibility

$$m_v = \frac{C_c}{(1 + e_{r0})(\sigma' ln(10))} = \frac{-\partial e_r \Big/ \left(\dfrac{\partial \sigma'}{\sigma' \ln(10)} \right)}{(1 + e_{r0})(\sigma' ln(10))} = \frac{-\partial e_r \big/ \partial \sigma'}{(1 + e_{r0})}$$

Terzaghi's one dimensional consolidation equation can be solved by Fourier series since it is a second order, partial differential equation. Its solution is shown in Equation 63, in which u_v is the degree of consolidation, T_v is dimensionless time or 'time factor' (given by Equation 64), t is time, h_v is dimensionless depth (given by Equation 65) and d is maximum drainage path. The graphical solution to this differential equation can be seen in Figure 18 below.

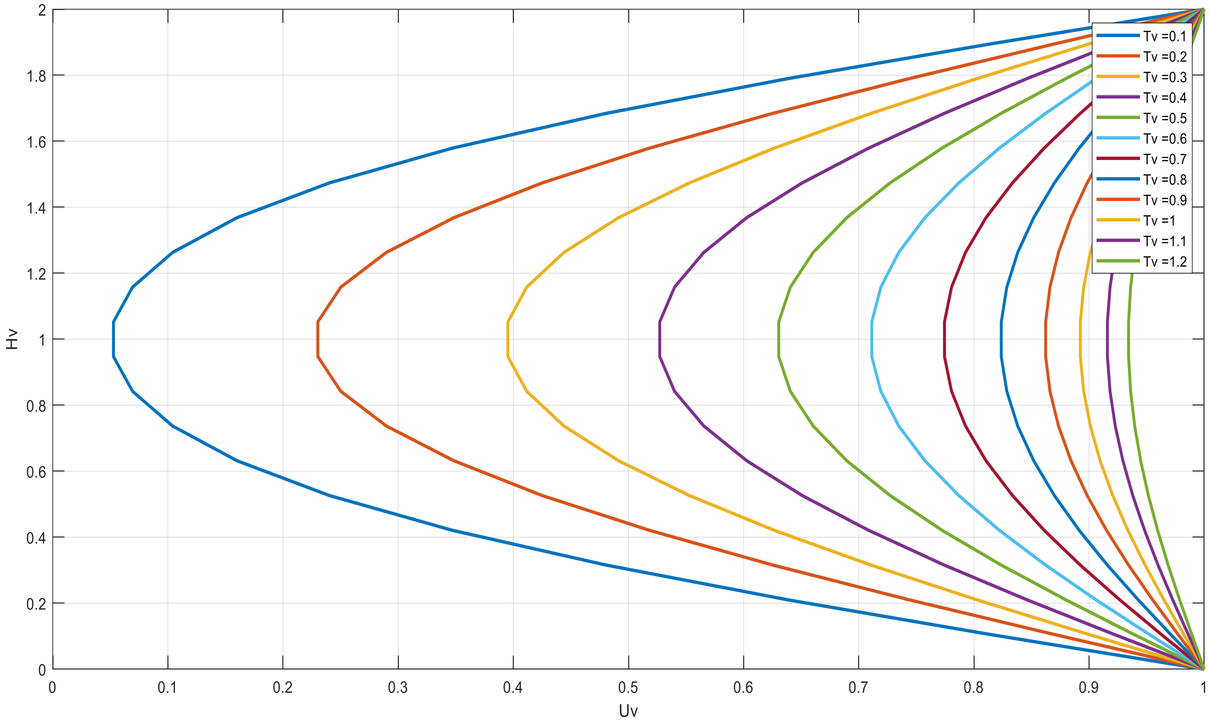

Figure 18: Graphical solution to Terzaghi's 1D consolidation equation

Equation 63: Degree of consolidation (vertical) from Terzaghi's Equation

$$u_v = 1 - \sum_{i=0}^{\infty} \left(\frac{4}{(2i+1)\pi} \sin\left[\frac{(2i+1)\pi}{2} h_v\right] e^{-\left[\left(\frac{(2i+1)\pi}{2}\right)^2 T_v\right]} \right)$$

Equation 64: Dimensionless time or Time Factor (vertical)

$$T_v = \frac{t c_v}{{H_v}^2}$$

Equation 65: Dimensionless Depth (vertical)

$$H_v = \frac{z}{d}$$

It should be pointed out that there are two types of maximum drainage paths in a consolidating system. If liquid is allowed to leave the consolidating medium at both ends (i.e. at both its top and bottom), double-drainage conditions exist and the maximum drainage path is half the depth of the consolidating medium. However, if liquid is only allowed to leave the system at one end of the consolidating medium, single-drainage conditions exist and the maximum drainage path equals the entire depth of the consolidating medium.

The degree of consolidation indicates the percentage completion of consolidation (reflected as soil settlement or strain) at any time and at any location within a consolidating soil. Recalling that the degree of consolidation depends on the rate of excess pore water pressure dissipation, the degree of consolidation may also represent the percentage of excess pore water pressure that has dissipated at a given time and at a specific location. Naturally, the difference between the degree of consolidation and unity gives the percentage of settlement that has not yet occurred, and the percentage of excess pore water pressure still undissipated. As implied earlier, the maximum excess pore water pressure in a consolidating medium equals the change in total stress that the medium is subjected to. The maximum strain the medium can experience (ε_{max}) is given by Equation 66. In geotechnical practice however, consolidation is often thought to be complete at 90% since its rate experiences a considerable decrease subsequently.

Equation 66: Ultimate Consolidation Strain

$$\varepsilon_{max} = m_v \sigma^{'}$$

The average value for degree of consolidation at a specific time into the consolidation process can be obtained by calculating the degree of consolidation at multiple locations for the corresponding time factor, and then averaging those values. Table 3 summarizes the relationship between average degree of consolidation and time factor for selected values.

Table 3: Depth-averaged degree of consolidation for specific time factors

Avg. Degree of Consolidation, %	Time Factor	Avg. Degree of Consolidation, %	Time Factor
0	0.0000	55	0.2389
5	0.0020	60	0.2864
10	0.0078	65	0.3404
15	0.0177	70	0.4029
20	0.0314	75	0.4767
25	0.0491	80	0.5671
30	0.0707	85	0.6838
35	0.0962	90	0.8481
40	0.1257	95	1.1290
45	0.1591	100	∞
50	0.1967		

2.3. Concluding Remarks

This literature review summarizes research relevant to two major areas. The first area focused on extruder modelling techniques for polymer processing applications, and reviewed methods for describing the geometry of a twin-screw extruder. Additionally, the relevant equations for describing the momentum and temperature changes of a polymer melt during transport were also discussed. The second area focused on understanding the material behaviour of an aqueous fibre suspension under flow and consolidation conditions, and required review of the botany, materials and geotechnical engineering literature. Together, the research from both areas provides significant insight into the problem of suspension extruder modelling and forms the foundation for the novel algorithm developed and presented in Section 4.2.

3. Experimental

The following section summarizes the preparation methods and analytical techniques used to investigate the material properties of extruded, wet poplar samples obtained from Greenfield's twin-screw extruding system.

3.1. Fibre Preparation

The natural fibre suspensions used in this study were mixtures of shredded poplar woods and water. The suspensions were prepared in the following manner. Steamed poplar wood chips obtained from ECOSTRAT Inc. were sized using a stainless steel extruder belonging to the Omega 75 series from Steer. The total length of this extruder was 3000 mm long and had a diameter of 75 mm. The screw profile for this extruder consisted of both slit and non-slit forward conveying screw elements with lengths ranging from 30 to 90 mm. This extruder was operated at a consistent speed of 105 rpm (corresponding to 60% maximum speed) and a dry biomass throughput of 0.05 kg/s. After sizing, the poplar fibres were transferred to a reactor operating at a temperature of about 180^{o}C and pressure of 830 kPa (gauge). The biomass was 'cooked' at those conditions for about 75 minutes. Upon cooking completion, the poplar fibres were transferred to a second extruder also belonging to the Omega 75 series from Steer. This extruder was 4500 mm in length and had a diameter of 75 mm. The screw elements composing the screw profile were forward conveying, reverse conveying and flight-less screw elements with lengths ranging from 15 to 90 mm. Ports located at various points along the extruder's barrel facilitated fluid addition and removal as found necessary. The operating speed of this extruder was 315 rpm (corresponding to 90% maximum speed) and its dry biomass throughput was 0.05 kg/s. The second extrusion stage was followed by a second cooking stage in a reactor operating at a temperature of about 205^{o}C and pressure of 1600 kPa (gauge). The biomass was 'cooked' at those conditions for about 9 minutes. This preparation process is shown schematically in Figure 19.

The poplar samples analysed in this study were obtained from two points in the above-described process. The samples termed 'coarse poplar' (subscripted $'R1'$ in equations) were obtained at the end of the first cooking stage and before the second extrusion stage. This biomass had an average 'natural' water content of 331%. The samples termed 'fine poplar' (subscripted $'R2'$ in equations) were obtained at the end of the second cooking stage and had an average 'natural' water content of 153%. Variations in the water content of both the coarse and fine poplar biomass were obtained by adding deaerated water to previously oven-dried samples. The amount of water added depended on the target water content desired and the mass of the dried biomass being prepared. The resulting mixtures were left for two days at room temperature and pressure before further tests were carried out. A conservative wait period of two days was selected to ensure that the new equilibrium water contents had been reached despite the highly absorbent nature of wood fibres. The target 'artificial' water contents for the coarse poplar suspensions were 100%, 200%, 400% and 500%, while the target water contents for the fine poplar suspensions were 100%, 200% and 300%.

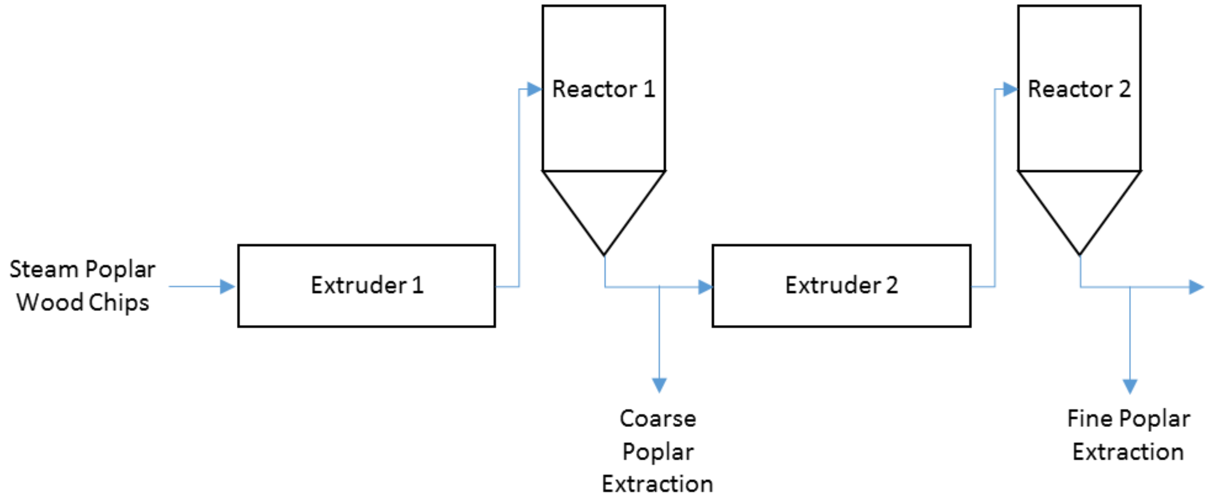

Figure 19: Schematic of poplar fibre preparation in Greenfields's extruding system

3.2. Water Content Measurement

The water content of the biomass was determined in accordance with the procedure outlined in ASTM D 2216 (2010). Known masses of wet poplar were placed in a Despatch LBB2-12-1 oven maintained at about 101°C for at least 6 hours. The lowered oven temperature (when compared to that stipulated in the standard) was used to minimize biomass burning during drying. For this procedure, the term 'sample' refers to a known mass of poplar fibres that has been placed in a foil pan (also of known mass) in either a dry or wet state. After drying, the mass of water in each sample was determined by taking the difference between its pre- and post-oven-dried mass. The mass of the dry biomass was obtained by subtracting the respective tin pan mass from that of the oven-dried sample. The water content, WC, of each sample was then calculated using Equation 67.

Equation 67: Water Content

$$WC = 100\% \times \frac{m_w}{m_{f|o.d.}}$$

where m_w is the total mass of water (both absorbed and interstitial), and $m_{f|o.d.}$ is the mass of fibres (oven dried).

3.3. Oedometer Tests

Oedometric testing was carried out using the Automatic Consolidation System II (ACONS II) by VJ Tech, along with the Combined Laboratory Integrated Software Package (CLISP) Studio Module (Version 2.5.1.1929) in accordance with the procedure outlined in ASTM D 2435 (2011a). Dedicated compressibility tests were carried out using a circular compression cell with a depth of 20 mm and diameter of 70 mm for unsaturated fine and coarse poplar suspensions at three different water contents. For the fine poplar, the investigated water contents were 108%, 226% and 324%, while that for the coarse poplar were 116%, 213% and 331%. Each sample was subjected to an incremental pressure loading cycle for 2 minutes, immediately followed by an incremental pressure unloading cycle for 1 minute. These relatively quick loading and unloading rates were selected to be comparable to the conditions experienced in the second extruder from the bioenergy production process summarized in Figure 19. The specific loading cycle applied was 100 kPa, 200 kPa, 400 kPa, 800 kPa and 1600 kPa, while the specific unloading cycle applied was 800 kPa, 400 kPa, 200 kPa and 100 kPa. Each test was replicated twice.

To evaluate the compression and recompression ratios, the total vertical strain achieved during each loading (and unloading) stage was plotted with the instantaneous pressure applied by the oedometer for each sample. An example of such a plot is shown in Figure 20, which displays the results obtained for all replicates of the coarse poplar suspensions at 116% water content. From those plots, best fit lines fitted to the respective loading and unloading portions of each replicate were used to determine the compression and recompression ratios, respectively.

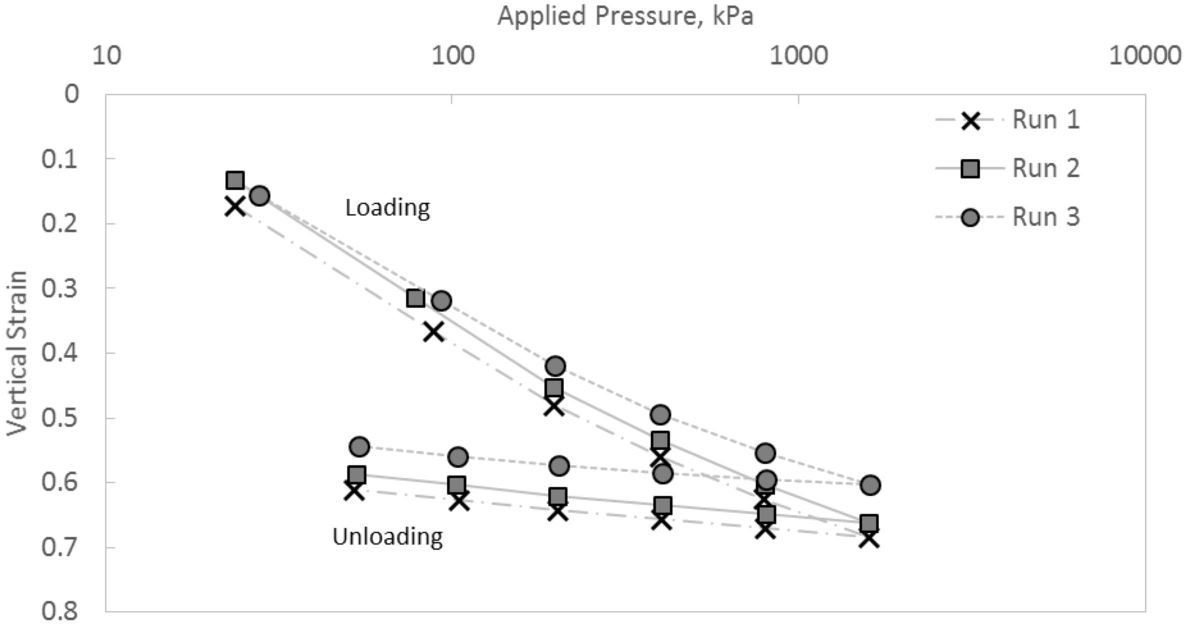

Figure 20: Vertical strain vs. applied pressure for coarse poplar suspensions at 116% water content

The compression ratio ($C_c{}'$) was calculated for each test by substituting the values at two different points on the loading curve into Equation 68.

Equation 68: Compression/Recompression Ratio

$$C_c{}' = -\frac{\varepsilon_2 - \varepsilon_1}{log\left(\frac{P_2}{P_1}\right)}$$

where ε is the instantaneous vertical strain and P is the instantaneous applied pressure. The recompression ratio ($C_r{}'$) for the fibres was calculated in a similar manner*;* however*,* two points from the unloading curve were substituted instead. Confidence intervals were constructed for triplicate averages of each compressibility coefficient using a confidence level of 95%.

The instantaneous permeability of the samples at the end of each loading stage was determined from theoretical relationships (Germaine and Germaine 2009), and soil parameters, such as the coefficient of vertical consolidation and the coefficient of volume compressibility, obtained from the CLISP software. To calculate instantaneous permeability, the instantaneous hydraulic conductivity, k_v, was first determined from Equation 69 below.

Equation 69: Hydraulic Conductivity

$$k_v = c_v m_v \rho_w g$$

where c_v is the instantaneous coefficient of consolidation, m_v is the instantaneous coefficient of volume compressibility, ρ_w is the density of the expressed liquid and g is the acceleration due to gravity. The instantaneous intrinsic permeability, K, at the end of each loading stage for each replicate was given by Equation 70.

Equation 70: Permeability

$$K = \frac{k_v \mu_w}{\rho_w g}$$

where μ_w is the viscosity of the expressed liquid. The viscosity and density properties of the expressed liquid were comparable to the properties of water at 20 ^{o}C. Error bars were determined based on the standard deviation of triplicate values for both the compressibility and permeability data.

3.4. Direct Shear Test

Direct shear testing was carried out using a direct shear box apparatus from ControlsGroup (model number: 27-T2060) along with the Data Acquisition System Laboratory (DASYLab) 2016 (Version 14.0.0) in accordance with the procedure outlined in ASTM D 3080 (2011b). All tests were carried out using a 60 mm by 60 mm shear box at a shear rate of 0.0334 mm/s. This relatively large shear rate was selected to ensure that shearing was comparable to that of the second extruder from the bioenergy process summarized in Figure 19. The direct shear test was used to determine both the coefficient of internal friction of the dried coarse and fine poplar fibres, and the coefficient of interface friction of each fibre type with stainless steel at a variety of water contents. The coefficient of internal friction was obtained by performing the test on a shear box that was completely filled with biomass. The coefficient of interface friction was obtained by performing the test on a shear box in which the bottom half was filled with a stainless steel block and the top half filled with biomass. For the coarse poplar suspensions, interface friction tests were carried out at water contents of 0% (i.e. oven dried fibres), 117%, 329% and 392% while for the fine poplar suspensions, tests were carried out at 0% (i.e. oven dried fibres), 49%, 144% and 225%. To obtain a single value for either friction coefficient, three different samples were prepared and sheared under pressures of 16.3 kPa, 31.3 kPa and 46.2 kPa. This was replicated twice for all fibre and water content variants investigated.

To obtain values for the friction coefficients, the measured shear stresses were plotted against their respective applied pressures for each sample. Figure 21 shows the results obtained for the coefficient of internal friction replicates of dried coarse poplar fibres, as an example. For all replicates, best fit lines were fitted to the data to obtain the regression gradients, which were the friction coefficients for the assessed samples. Error bars were constructed based on the standard deviation of triplicate runs for each friction coefficient. The corresponding frictional angles were obtained by taking the arc-tangent of each friction coefficient.

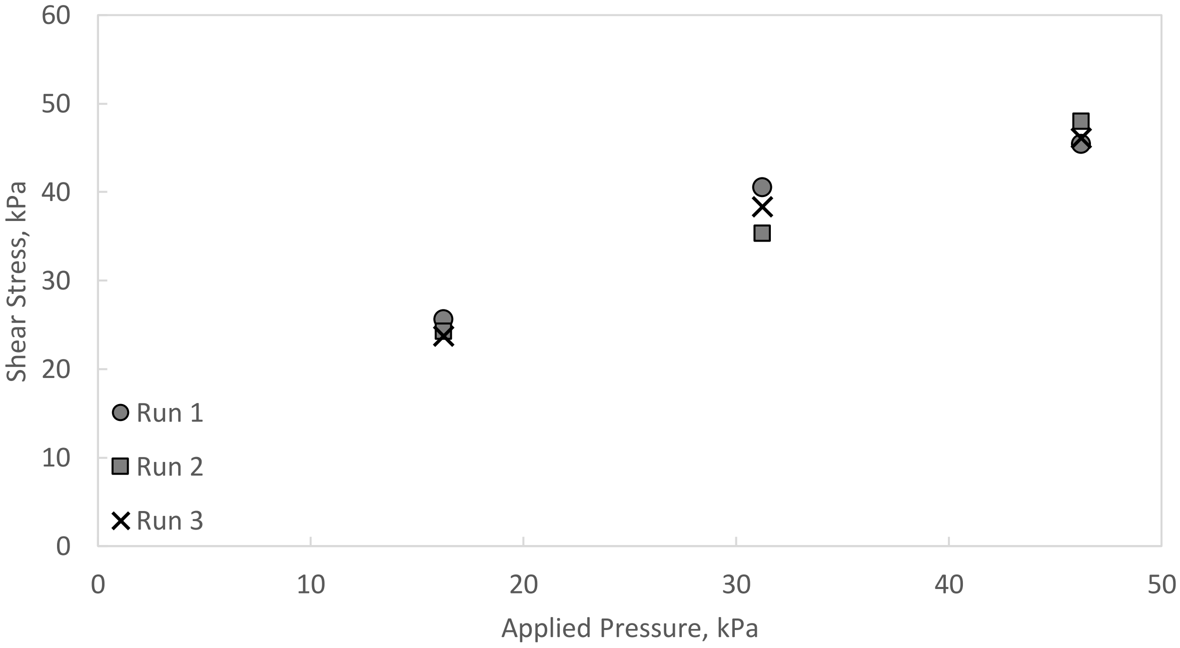

Figure 21: Shear stress vs. applied pressure for dried coarse poplar fibres in a fully-filled direct shear box

3.5. Torvane Test

The yields stress of the fibres was determined using ASTM D 2573 (2018) and ASTM D 4648 (2016). Measurements were made on samples of known water contents using a torvane from Solidtest.Inc. Two different water contents were investigated for each of the fibre suspensions. For the fine poplar, the investigated water contents were 151% and 204%, while for the coarse poplar, the values were 381% and 530%. All tests were replicated twice for each fibre/water content variant stated.

3.6. Microscopy

The fibre length distribution and average fibre lengths of the coarse and fine poplar fibres were obtained through microscopy carried out at Biotron, Western University. An AxioImager Z1 Upright Microscope equipped with an AxioCam MRc camera from Carl Zeiss Canada was utilized together with the ZEN Pro 2012 software (Blue Edition). All images were taken in greyscale at a magnification of 10x, and the lengths of the fibres in those images were measured using ImageJ (Version 1.51) by Fiji. In total, 228 images were obtained, at least 100 images were taken of each fibre type. From these images, 295 individual coarse poplar fibres and 396 individual fine poplar fibres were measured.

Scanning Electron Microscopy (SEM) was carried out using the S-3400N Microscope from Hitachi, along with its associated software (operation version: 2.10, evacuation version: 2.6). Images were taken of dried fibres that had been treated with an Ar/Pd coating using the Hummer VI Sputter Coat Unit from Technics.

3.7. Mass Spectrometry (MS) and High Pressure Liquid Chromatography (HPLC)

MS and HPLC measurements were carried out on the lignin of both poplar samples with the kind help of Dr. Mamdouh M. Abou-Zaid. While the full procedure used can be found in his publication (Qazi et al. 2017), a summary of the procedure will be presented here. Lignin was extracted from the poplar fibres using iso-propanol. After extraction, HPLC was performed on the lignins using Thermo Scientific's LTQ Orbitrap Discovery equipped with a Syncronis C18 column that was 50 mm long with an internal diameter of 2.1 mm. The particle size of the stationary phase was 1.7

µm, and the liquid injection volume was 10 µL. The mobile phase was circulated at a rate of 0.2mL/min, and was a mixture of AcN and water, both acidified with 0.1 vol % of formic acid. The relative concentrations of the two liquids in the mobile phase varied throughout each run using the gradient technique, and the total elution time was 22 mins. Mass spectroscopy was carried out using Thermo Scientific's LTQ Orbitrap MS at a mass resolution power of 30,000 (m/△m) at m/z 400. Data analysis was performed using multi-group method of XCMS online bioinformatics platform.

4. Results and Discussion

4.1. Material Characterisation

The following section summarizes the results from the chemical, physical and material characterisations of extruded, wet coarse and fine poplar suspensions. Most of the utilised techniques have been standardized within the geotechnical engineering discipline, and have been used for the analysis of many different soil types. This includes soils such as fibrous peats, which share many physical similarities with processed, high consistency wood pulps and suspensions. Although a few methods are available for the characterisation of high consistency pulps, research in this area is lacking when compared to that for more diluted pulp mixtures. To minimize this knowledge gap, use of certain relevant geotechnical techniques have been suggested and applied as alternative methods for the characterisation of high consistency pulps. Within each of the subsequent subsections, the results from each test are compared with literature values that are typical of fibrous peats. Such comparisons were made to assess the suitability of the different geotechnical techniques used for the characterisations. Additionally, the effect of various process parameters, such as water content and fibre type, was assessed using statistical techniques. It should be pointed out that the two poplar fibres differed from each other due to differences in their preparation procedures - the fine poplar fibres underwent an additional extruder and reactor stage while the coarse poplar fibres did not. The additional extrusion phase is expected to significantly contribute towards the physical differences observed between the two fibres. The conditions in the additional reactor stage are not aggressive enough to create significant chemical differences between the two fibres. This assumption is validated by the fact that the highest temperatures in the reactors was 205°C, which is the low end for thermal degradation of woody biomasses in a non-aqueous environment (Schniewind 1989, p. 271 - 237).

4.1.1. Dimensions of Fibres

The length distributions of the course and fine poplar fibres are summarized in Figure 22. It is observed from Figure 22 that most of the fibres in both poplar samples have lengths ranging from 0 mm to 0.6 mm. However, a much larger fraction of the fine poplar fibres had lengths within the aforementioned range (about 89%) when compared to that of the coarse poplar fibres (about

69%). Another obvious feature of both distributions was a positive skew, which indicated a more prominent, longer fibre presence than that typically expected from a normally distributed sample. Although both the coarse and fine poplar fibre distributions had distinctive positive skews, that of the coarse poplar fibres was more significant. Approximately 17% of the coarse poplar fibres had lengths that equalled or exceeded 1 mm, of which the maximum fibre length was about 2.3 mm. Only 5% of the fine poplar fibres had lengths that equalled or exceeded 1 mm, of which the maximum was about 1.8 mm. The distinctive differences in the distributions of the two fibres is easily justified when their specific preparation procedures are considered. The fine poplar fibres were subjected to further shearing from a second extrusion stage, which provided additional opportunities for breakage. This had a two-fold effect since breakage reduces the lengths of longer fibres while simultaneously increasing the number of shorter fibres. Although not completely representative, the average fibre length for both fibres was evaluated. For the coarse poplar fibres, the average fibre length was about 0.5 mm, while that for the fine poplar fibres was about 0.3 mm.

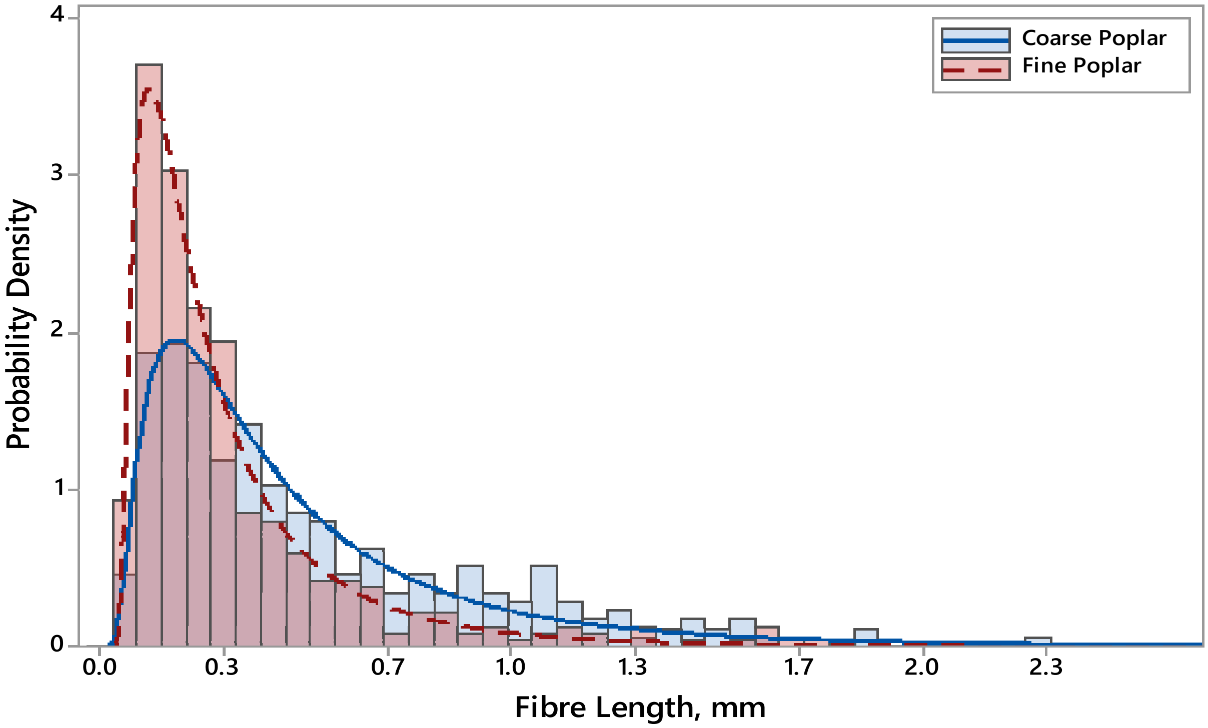

Figure 22: Histogram of Poplar Fibre Lengths

The coarse and fine poplar samples were composed mostly of fibres with lengths comparable to that of fibrous peats. Fibrous peats refer to peaty soils that are composed of plant elements such as stems, leaves and root fragments that are still quite distinct due to little anaerobic decomposition. These elements typically range from 0.020 mm to 1.2 mm in length, 0.1 mm to 1.2 mm in width, and 0.010 mm to 0.015 mm in thickness (Landva and Pheeney 1980; Mesri and Ajlouni 2007). For both the coarse and fine poplar fibres, about 87% had lengths within this range. It was difficult to obtain the average diameter distribution of the fibres since the average diameter of a single fibre would require many measurements due to the dependence of the instantaneous fibre diameter on fibre length. However, for both the coarse and fine poplar, the instantaneous diameter at any point along the measured fibres remained within the range of 0.005 mm to 0.065 mm. When upper-range dimension comparisons are made with those typical to fibrous peats, and the instantaneous 'depth' and 'width' of the fibres are assumed about equal to their instantaneous diameters, the width of the poplar fibres could be about 18 times smaller than that of a single peat element, while its thickness can be up to 4 times larger.

4.1.2. Chemical Characterisation

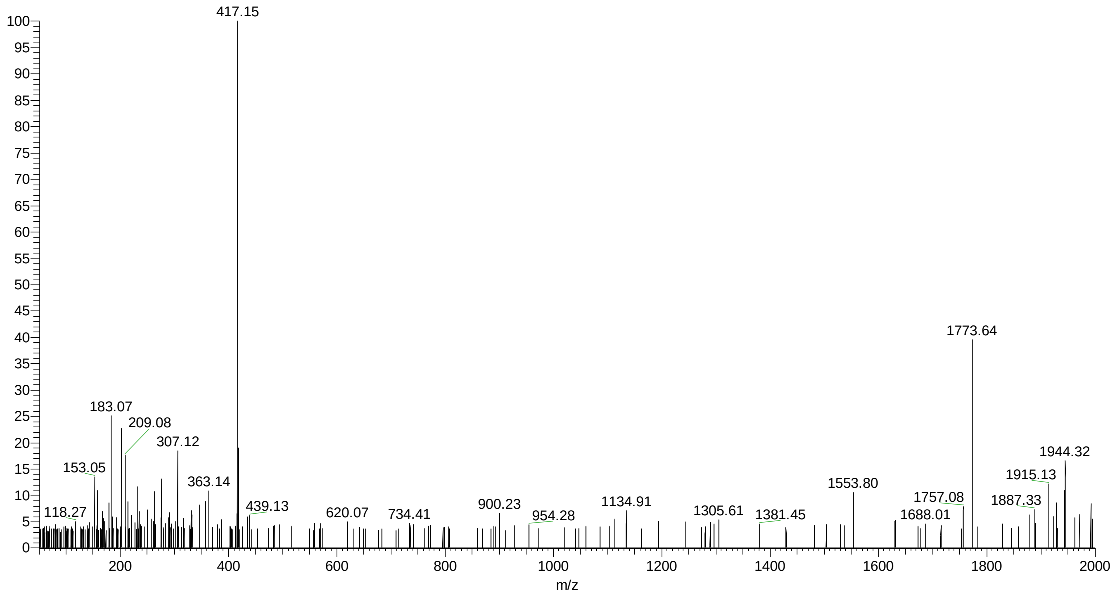

Figure 23: Mass Spectrum for Poplar R1 (Coarse Poplar) Lignin

Mass Spectrometry (MS) and High Performance Liquid Chromatography (HPLC) were carried out to determine whether significant chemical dissimilarity can be found between the lignin of the fine and coarse poplar fibres. Analysis of the lignin was selected over cellulose and hemicellulose because the lignin component had the greatest potential for chemical variations in its structure. Based on this, it was concluded that a similar lignin composition was evidence for similar chemical compositions between the two fibres. Figure 23 and Figure 24 show the mass spectrums of the two fibres up to a mass-to-charge ratio of 2000, and from those figures, it could be seen that both mass spectrums show many peaks at comparable mass-to-charge ratios. This suggests chemical similarity between the two poplar samples. Figure 25 and Figure 26 show the chromatograms for the lignins of the coarse and fine poplar fibres respectively. Again, there is evidence to support great similarity between the two fibres since both chromatograms share numerous pivotal peaks at similar retention times. For instance, between retention times of 4 to 6 minutes, both chromatograms contain three peaks – two 'minor' peaks at about 4.50 and 4.86 minutes respectively, and a 'major' peak at about 5.32 minutes. Several other regions of great similarity can be found at retention times ranging from 3 to 17 minutes, and 18 to 19 minutes.

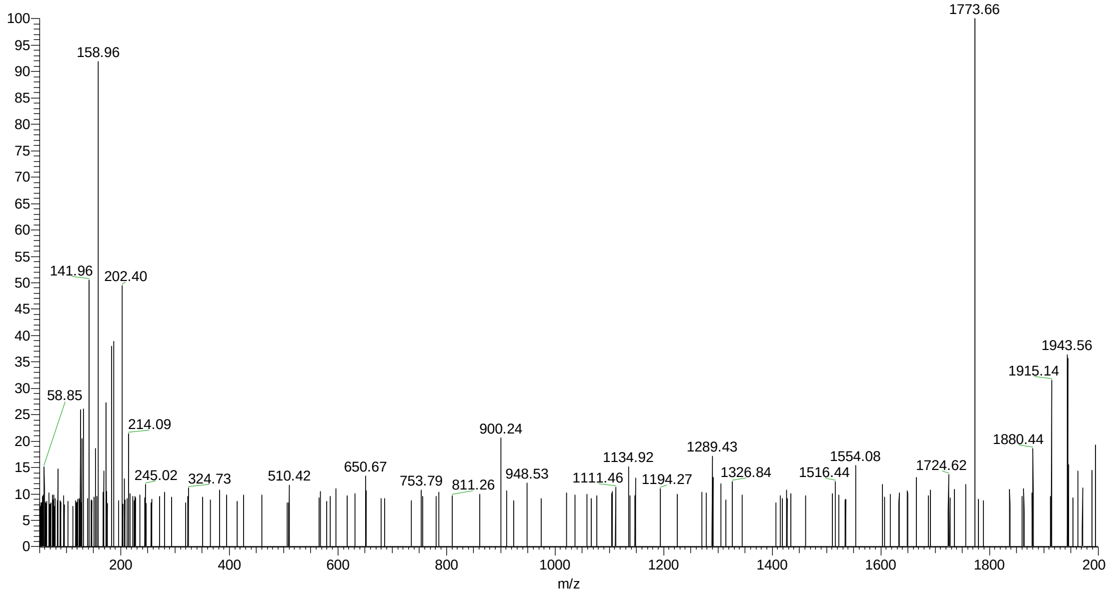

Figure 24: Mass Spectrum for Poplar R2 (Fine Poplar) Lignin

Although very similar, there are regions between the two chromatograms that are quite different. The two most obvious regions are located at retention times ranging from 0.5 to 2 minutes, and 17 to 18 minutes. The retention time period ranging from 0.5 to 2 minutes indicates the presence of a compound with a high affinity for the mobile phase in the fine poplar chromatogram. However, this fragment cannot be found in the chromatogram of the coarse poplar. The absence of this peak may be due to slight differences in the structure of the coarse and fine poplar fibres due to the natural variations that exist in wood cells (as discussed in Section 2.2.1.1), but may also be due to an unmatched impurity between the two samples. Additionally, this absence may be attributed to the detector's inability to identify the fragment in the coarse poplar samples because it might exist in much smaller concentrations. The coarse poplar chromatogram has a significantly larger number of peaks during the retention time period ranging from 17 to 18 minutes when compared to that for the fine poplar. From the high activity in this region, there is a strong possibility that the missing compounds are present in the fine poplar chromatogram, but their signals were not properly separated, resulting in data overlap.

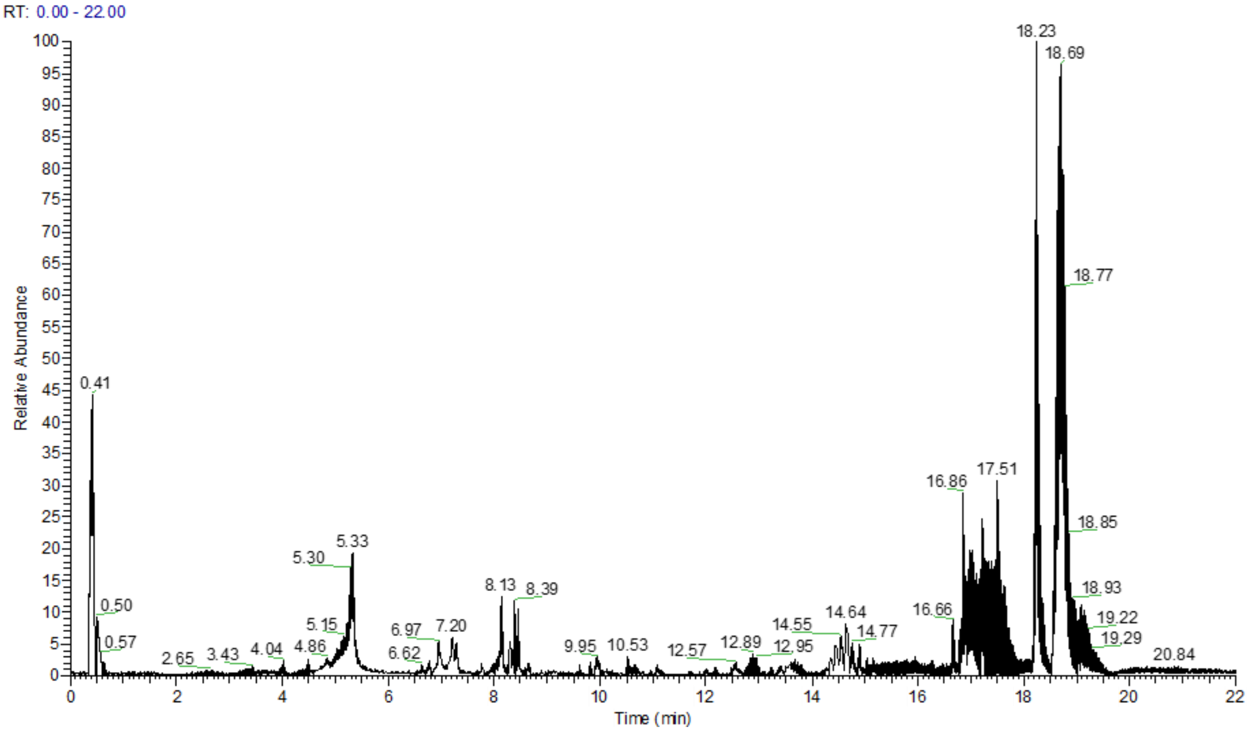

Figure 25: Chromatogram for Poplar R1 (Coarse Poplar) Lignin

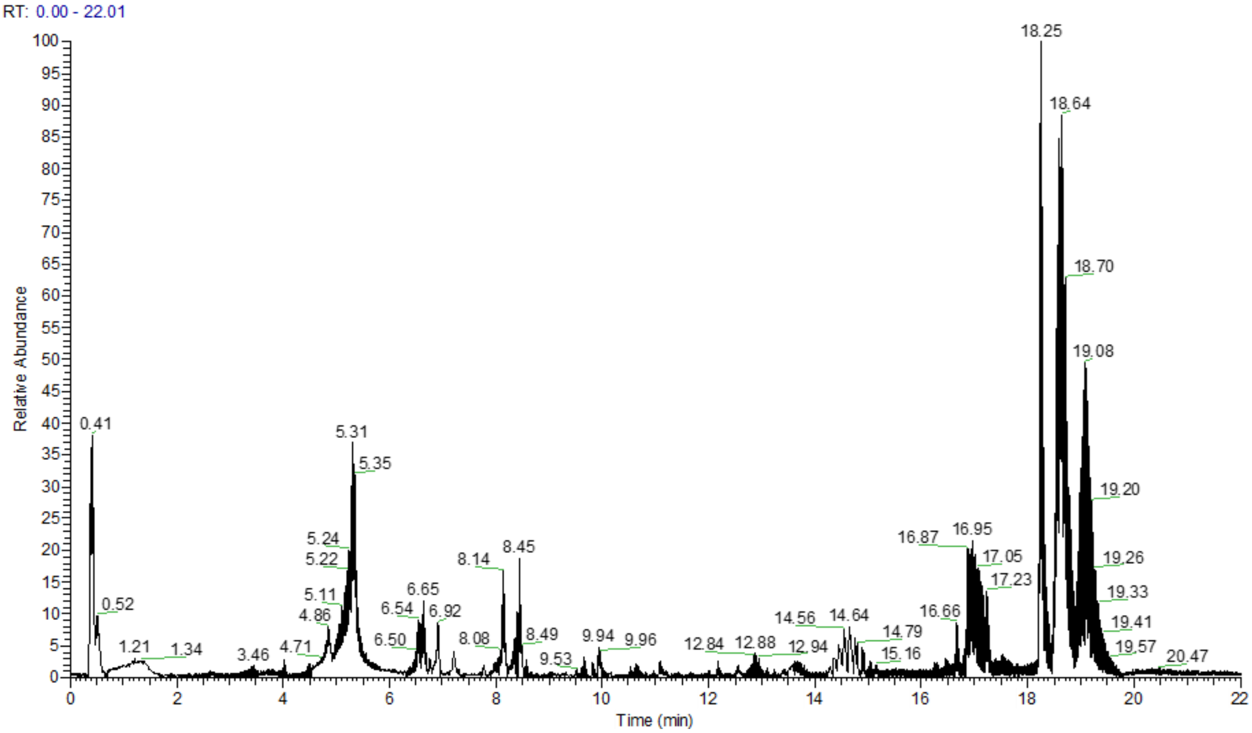

Figure 26: Chromatogram for Poplar R2 (Fine Poplar) Lignin

Although the mass spectrum and chromatogram pairs share many of the same peaks, the relative abundance tend to vary between the respective figure-pairs. Those differences, while quantifiable, were difficult to accurately assess since standard calibration curves would be required for each individual compound identified in the figures. To create a standard curve, a target compound would need to be purified and a series of runs would need to be carried out using different concentrations each run. A standard could then be prepared by plotting the intensities detected by the device during each run with the respective injection concentration. This work is beyond the scope of this project, but would be an interesting phenomenon to investigate in another study. Regardless, comparable peak locations between the two graphs strongly suggest significant chemical similarity between the coarse and fine poplar fibres, despite their differences in processing treatments. For the current study, this evidence is sufficient to eliminate chemical differences as a relevant factor in the subsequent material characterisations.

4.1.3. Surface Characterisation

The coefficient of friction provides a relationship between the critical shear stress and applied pressure pairs which result in slippage at the interface between two surfaces. The coefficients of interface friction for the coarse and fine poplar suspensions (at various initial water contents) and stainless steel were determined using a modified direct shear box technique, and have been summarized in Figure 27. From this figure, it can be observed that the coefficient of interface friction seems to depend on neither fibre type nor initial water content due to significant overlap in the plotted error bars, which is the standard deviation of the data. To validate this, several difference-in-mean hypothesis tests were carried out. The first hypothesis test assessed the effect of initial water content on the interface friction for each poplar type. For both poplar fibres, differences in interface friction due to variations in initial water content were statistically insignificant at a confidence level of 95%. The second hypothesis test assessed the differences between the average interface friction coefficients of the coarse and fine poplar samples. This test revealed that the differences in interface friction due to poplar type were statistically insignificant at a confidence level of 95%. Based on these conclusions, and average value for the coefficient of interface friction (under drained conditions) between stainless steel and poplar fibres with initial water contents ranging from about 0% to 400% can be proposed. The average coefficient of interface friction was found to be 0.68, which corresponds to an interface friction angle of 34^{o}.

The coefficient of internal friction was determined for oven-dried samples of both the fine and coarse poplar fibres. The test was only carried out on dried fibres since initial water content was found to have a negligible effect on the interface friction coefficients obtained from prior testing, and because the dried fibre tests were easier to reproduce. For the fine poplar fibres, the average coefficient of internal friction was found to be 0.86 ± 0.08, while the average coefficient of internal friction for the coarse poplar fibres was found to be 0.73 ± 0.07, corresponding to average internal friction angles of 40.7^{o} and 36.3^{o} respectively. These values are in good agreement with that expected of fibrous peats which typically ranges from 35° to 45° when measured using the direct shear box method (Mesri and Ajlouni 2007). Like fibrous peats, the large friction coefficients of the fine and coarse poplar fibres can be attributed to extensive fibre interlocking (Mesri and Ajlouni 2007). However, these large friction coefficients may also be encouraged by the roughened surfaces of the fibres, as seen in Figure 28 and Figure 29. Although the surfaces of both fibres were quite rough, it can clearly be seen that the coarse poplar fibres have the greater surface texture. The surface of the coarse poplar fibres also contained a significantly larger number of ‘filaments’ when compared to that of the fine poplar fibres. Again, this difference in surface appearance may be justified when the specific preparation process of both fibres is considered. The additional shearing from the second extrusion stage not only provided additional opportunities for breakage, but also smoothed the surfaces of the fibres by shearing them against each other. This resulted in a less-textured, fine poplar fibre surface when compared to that of the coarse poplar fibres.

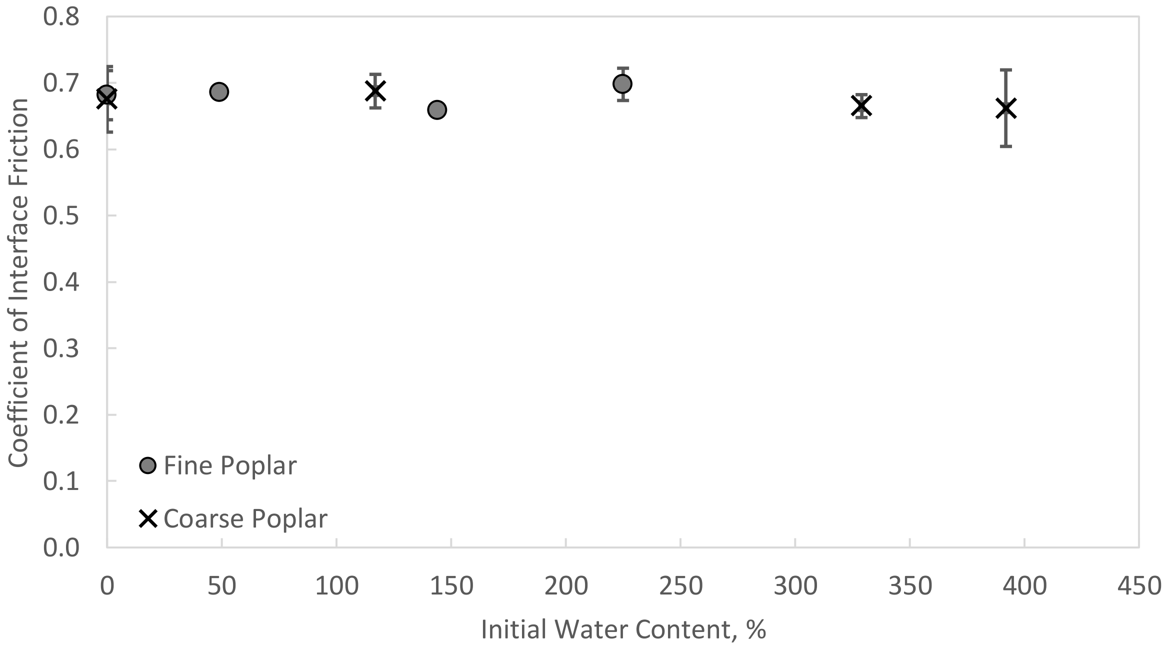

Figure 27: Coefficient of Interface Friction vs. Initial Water Content for Fine and Coarse Poplar Suspensions

While the values for the coefficient of internal friction for both the fine and course poplar fibres are quite agreeable with that measured for fibrous peats, the difference between these averages is fairly large considering both of the fibres belong to the *populus genus*. The source of this discrepancy may be due to unavoidable differences in the void ratio of the sheared samples since variations in void ratio lead to differences in the degree of interlocking at the shear plane (Coduto 1999; Das 2009). Thus, it is likely that there was less severe fibre interlocking for the coarse poplar fibres due to less regular packing from their longer fibre lengths and consequent fibre flocs. This deficiency reduced the shear strength of the coarse poplar samples, which ultimately led to the measurement of a smaller coefficient of internal friction when compared to that obtained for the fine poplar samples.

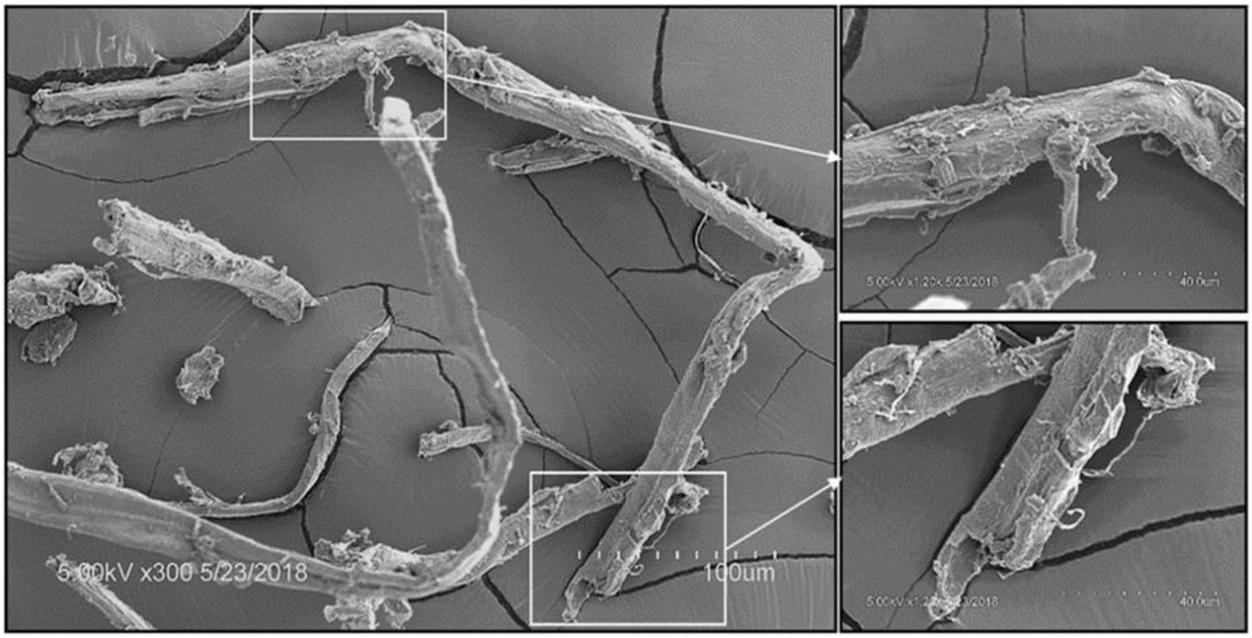

Figure 28: SEM Images of Coarse Poplar Fibres

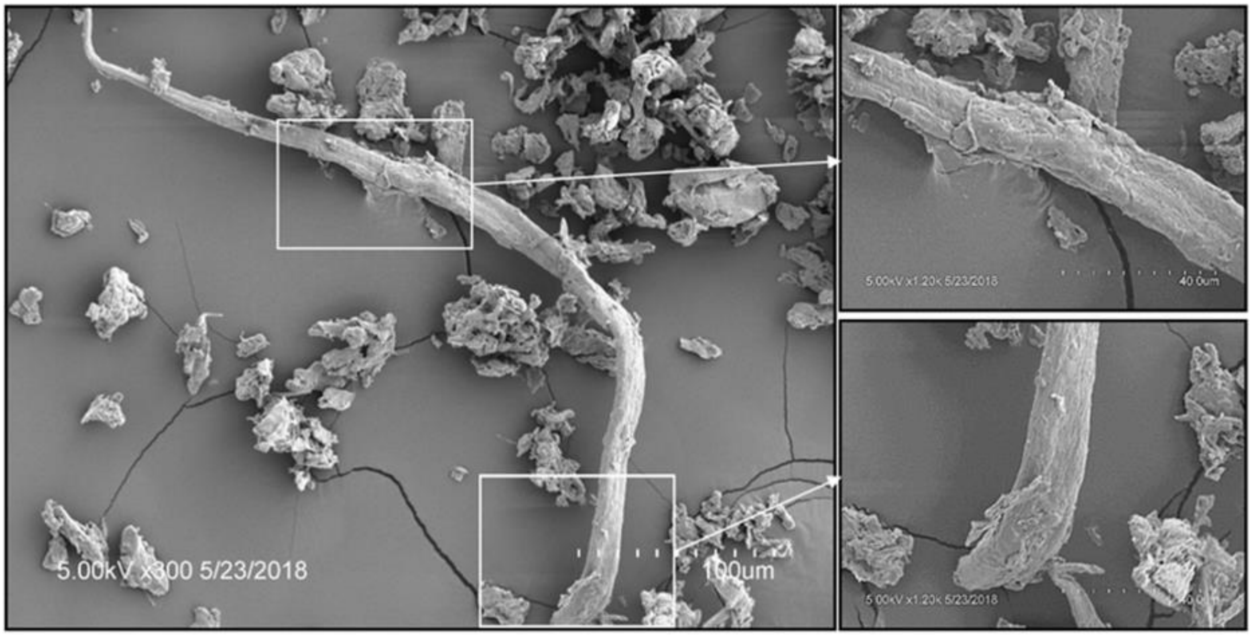

Figure 29: SEM Images of Fine Poplar Fibres

4.1.4. Material Characterisation

4.1.4.1. Permeability and Porosity

The permeability (K) of a material is a measure of its fluid-transmitting capacity. This property is dependent on the amount of hallow spaces that are inherent to the material's structure (i.e. porosity), as well as the average size and shape of the flow channels they form. In general, the permeability of a material tends to increase with its porosity and with an increase in the number of large, straight flow channels within its matrix. The effect of applied pressure on the permeability of the poplar fibres is shown in Figure 30. From this figure, both plots seem to be logarithmically shaped while converging to similar permeabilities at larger applied pressures. Further investigations were carried out using several difference-in-mean hypothesis tests. The first hypothesis test assessed the effect of initial water content on the permeability of each poplar type. This test revealed that the differences due to variations in the initial water content of each poplar suspension were statistically insignificant at a confidence level of 95%. The second hypothesis test assessed the differences between the average permeabilities of the coarse and fine poplar samples. This test revealed that differences in permeability due to poplar type were statistically significant at a confidence level of 95% for all pressures, excepting the case at 200 kPa. For all cases, the permeabilities of the fine poplar samples were smaller than those of the coarse poplar samples, an occurrence attributed to differences in the initial void ratios of the fibres. As demonstrated in Figure 22, the fibres constituting the coarse poplar were generally longer than those of the fine poplar, and were more prone to entanglement. Consequently, the coarse poplar samples tended to contain a significant number of flocs that were larger in size. The presence of those flocs prevented regular packing and resulted in the coarse poplar samples having larger initial void ratios. The shorter fibre lengths of the fine poplar did not encourage the formation of large flocs, allowing samples to be regularly and more tightly packed. As a result, the void ratios of the fine poplar samples were smaller than those of the coarse poplar samples, ensuing their smaller permeabilities. Correlations relating applied pressure to permeability for both the fine and coarse poplar suspensions are shown in Equation 71 and Equation 72.

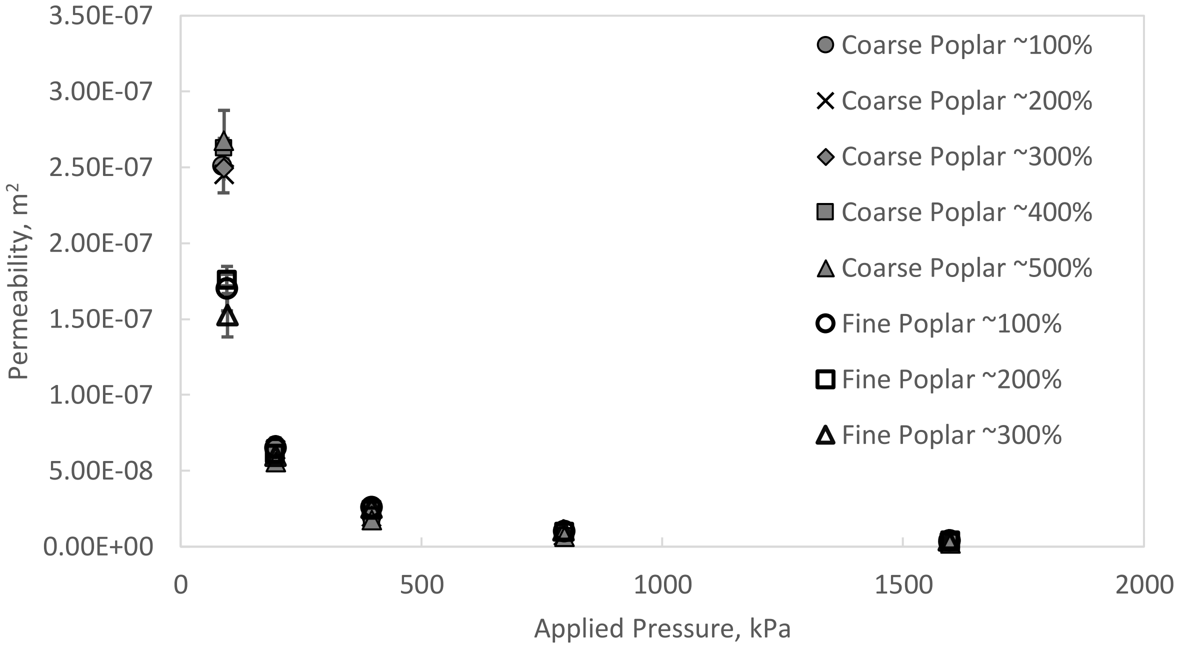

Figure 30: Permeability vs. Applied Pressure for Fine and Coarse Poplar Suspensions

Equation 71: Applied Pressure/Permeability Correlation for Coarse Poplar Suspensions

$$K_{R1} = 3 \times 10^{-4} \left(\frac{P}{1000}\right)^{-1.609}$$

Equation 72: Applied Pressure/Permeability Correlation for Fine Poplar Suspensions

$$K_{R2} = 7 \times 10^{-5} \left(\frac{P}{1000}\right)^{-1.321}$$

It should be pointed out that the initial permeabilities of both the course and fine poplar suspensions were about an order of magnitude larger than that typically observed in fibrous peats. For fibrous peats, values generally range from 10^{-11} m^2 to 10^{-8} m^2 if the permeating fluid is water at 20^{o}C (Mesri and Ajlouni 2007). While fibrous peats tend to be surficial, they are still subjected to small amounts of overburden pressures that can lower their initial porosities (or void ratios) and ultimately, their initial permeabilities. This is not the case for the coarse and fine poplar samples which had not been subjected to any pressures before testing, and had only been exposed to pressures during processing at least three weeks prior. Coarse and fine poplar permeabilities comparable to those of fibrous peats were observed when small pressures of about 200 kPa were applied during testing, as seen in Figure 30.

In addition to the permeability data, the effect of applied pressure on the porosity of the coarse and fine poplar suspensions during loading and unloading was measured by the CLISP software package during experimentation. Correlations detailing the relationships are listed below, from Equation 73 to Equation 76.

Equation 73: Applied Pressure/Porosity Correlation during Loading for Coarse Poplar Suspensions (Normally Consolidated Fibres)

$$n_{p,\,R1} = 0.5983e^{-0.001\left(\frac{P}{1000}\right)}$$

Equation 74: Applied Pressure/Porosity Correlation during Unloading for Coarse Poplar Suspensions (Over-consolidated Fibres)

$$n_{p,\,R1} = -0.049\log\left(\frac{P}{1000}\right) + 0.4623$$

Equation 75: Applied Pressure/Porosity Correlation during Loading for Fine Poplar Suspensions (Normally Consolidated Fibres)

$$n_{p,R2} = 1\times10^{-7}\left(\frac{P}{1000}\right)^2 - 4\times10^{-4}\left(\frac{P}{1000}\right) + 0.659$$

Equation 76: Applied Pressure/Porosity Correlation during Unloading for Fine Poplar Suspensions (Over-consolidated Fibres)

$$n_{p,\,R1} = -0.022\log\left(\frac{P}{1000}\right) + 0.5089$$

4.1.4.2. Compressibility and Volume Compressibility

A material's compressibility parameters show the relationship between the changes in the volume of a material when its pressure environment changes. In the geotechnical engineering discipline, these parameters are the compression ratio (C_c), which describes the behaviour of previously-uncompressed soil, and recompression ratio (C_r), which describes the behaviour of previously compressed soil. The compressibility of the fine and coarse poplar suspensions during the loading and unloading phases of oedometer tests have been summarized by their compressibility ratios in Figure 31 and Figure 32 respectively. For both compressibility ratios, it could be seen that the error bars, which is the standard deviation for the data, generally overlap for all investigated initial water contents and for both fibre types. This is a strong indication of statistical insignificance in the obtained data. To validate this, a series of difference-in-mean hypothesis tests were carried out. The first hypothesis test assessed the effect of initial water content on the compressibility coefficients of each poplar type. For each poplar, the test revealed that the differences due to variations in the initial water content were statistically insignificant at a confidence level of 95%. The second hypothesis test assessed the differences between the average compressibility coefficients of the coarse and fine poplar. This test revealed that differences in the compressibility coefficients due to poplar type were also statistically insignificant at a confidence level of 95%. Based on these conclusions, average compressibility coefficients that describe the behaviour of poplar fibres during compression and recompression can be proposed. The average compression ratio for poplar fibres during loading was found to be 0.260, and the average recompression ratio for poplar fibres during unloading (and reloading) was 0.046. From these values, it should be pointed out that the recompression index-to-compression index ratio for the poplar fibres was 0.177, falling within the 0.1 to 0.3 range (which is typical for fibrous peats (Mesri and Ajlouni 2007)).

Despite the clear statistical conclusions that were reached, it is observed that there exists some variability in the compressibility data obtained during both the loading and unloading phases. Such behaviour could be explained through classical elastic/plastic soil mechanics (Oswell 1991) as follows. There are two types of deformations that take place during the consolidation of the fibres: an unrecoverable plastic deformation and a recoverable elastic deformation. During loading, the fibres undergo both types of deformation and experience maximum volume change. Since the magnitude of the plastic deformation is generally much larger than the magnitude of the elastic deformation, it is likely that the variabilities in the calculated compression ratios are due to variations in the sources of plasticity of the prepared samples. A well-known factor that can influence the measured plastic deformations of fibrous peats is the anisotropic nature of its fibrous network (Mesri and Ajlouni 2007) due to variations in average fibre orientation. During unloading, the fibres only undergo elastic deformation, which is affected by the inherent elasticity of the poplar wood. Consequently, it is likely that the variations in the recompression ratios are due to variations in the quality (composition and porosity) of the poplar woods from which the fibres were obtained, as discussed in Section 2.2.1.1.

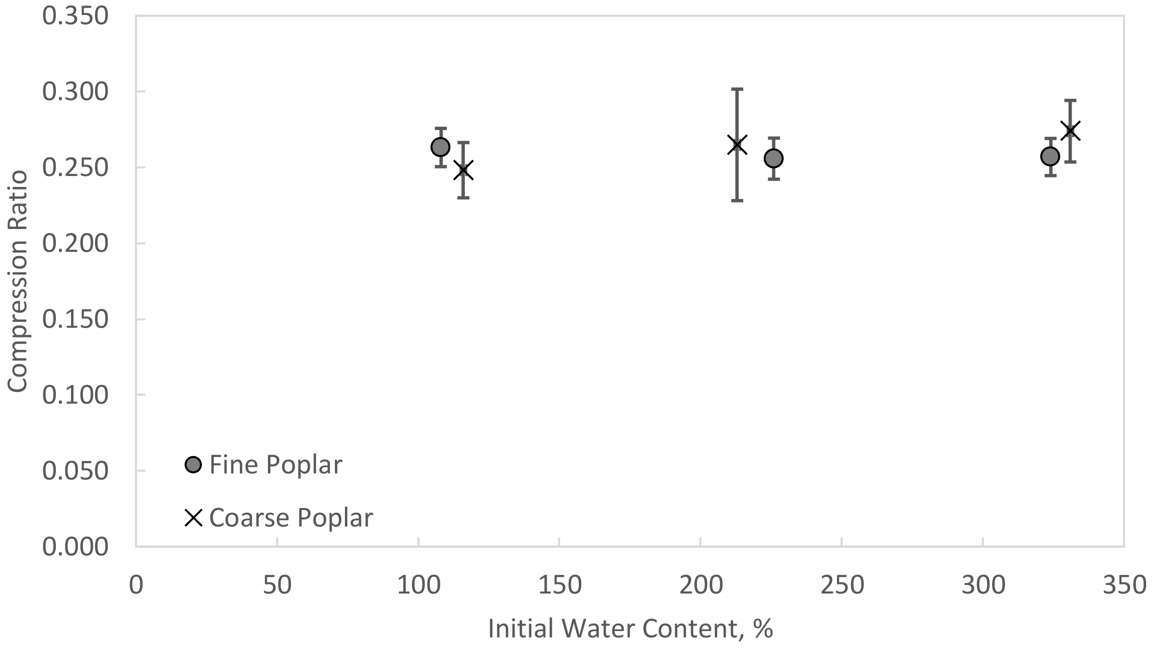

Figure 31: Compression Ratio vs. Initial Water Content for Fine and Coarse Poplar Suspensions

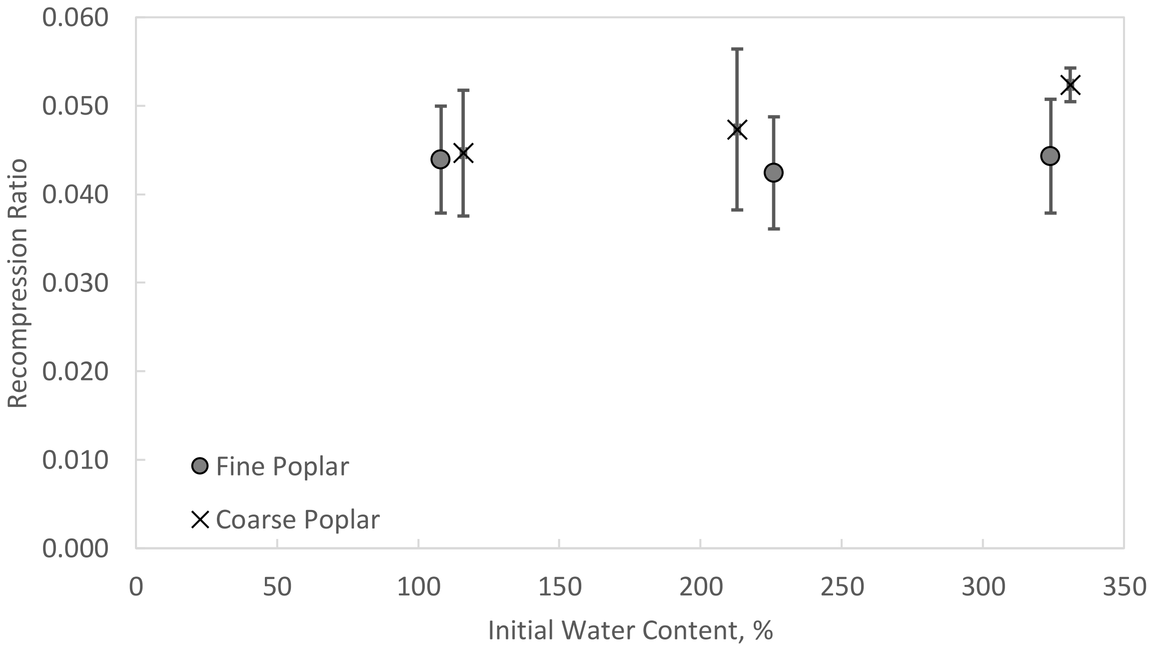

Figure 32: Recompression Ratio vs. Initial Water Content for Fine and Coarse Poplar Suspensions

In addition to the compression and recompression ratios, the coefficient of volume compressibility was obtained from direct measurements by the CLISP software package during experimentation. The coefficient of volume compressibility describes the change in volumetric strain per unit volume ($\Delta V/V$, or $\Delta e_r/(1+e_r)$ and $\Delta\varepsilon/\varepsilon$ for the case of soil mechanics) associated with a specific pressure change (ΔP, or $\Delta\sigma'$ again for the case of soil mechanics). Naturally, the coefficient of volume compressibility decreases with a decrease in initial permeability (via an increase in applied pressure). In general, the greater the initial permeability of a material, the greater its coefficient of volume compressibility (for the same solids material composition), since it experiences a greater volume change when subjected to an applied pressure. The effect of applied pressure on the coefficient of volume compressibility for the coarse and fine poplar suspensions is shown in Figure 33, and their specific correlations can be found in Equation 77 and Equation 78.

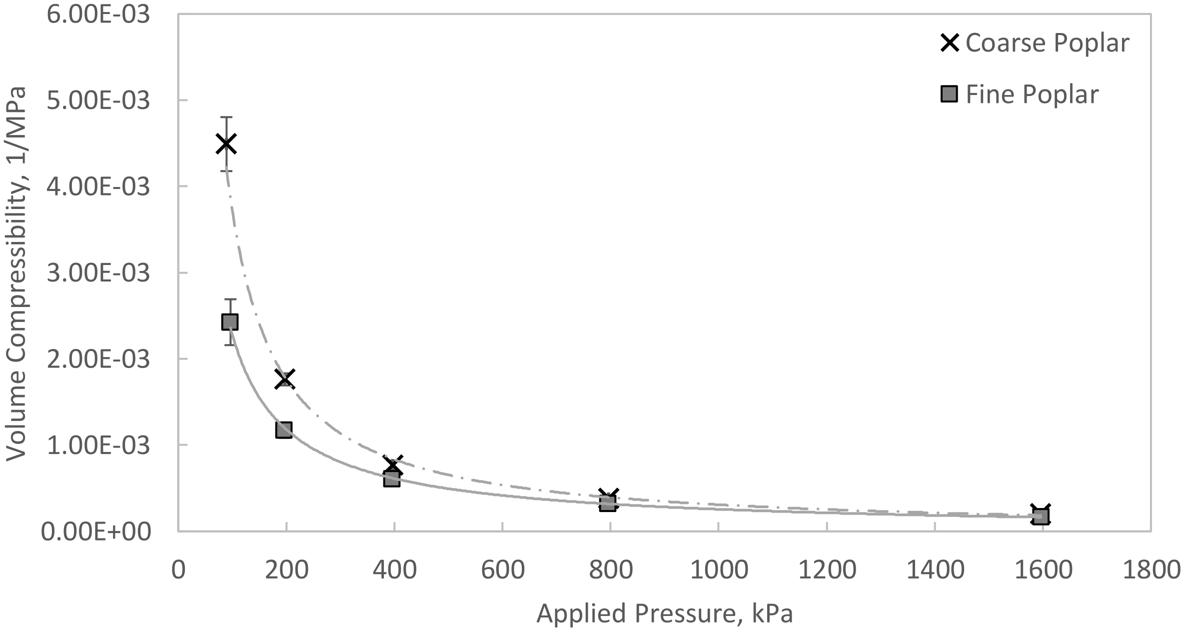

Figure 33: Volume Compressibility vs. Applied Pressure for Fine and Coarse Poplar Suspensions

Equation 77: Applied Pressure/Volume Compressibility Correlation for Coarse Poplar Suspensions

$$m_{v,\,R1} = 0.539\left(\frac{P}{1000}\right)^{-1.08}$$

Equation 78: Applied Pressure/Volume Compressibility Correlation for Fine Poplar Suspensions

$$m_{v,\,R2} = 0.1814\left(\frac{P}{1000}\right)^{-0.95}$$

4.1.4.3. Coefficient of Consolidation (Primary)

The coefficient of consolidation is a parameter that indicates how quickly a soil experiences compaction during consolidation. The coefficient of consolidation was obtained from direct measurement by the CLISP software package during experimentation. Figure 34 shows the indirect effect of initial material permeability (via applied pressure) on the coefficient of consolidation for both the coarse and fine poplar suspensions. From this figure, it could be seen that the coefficient of consolidation decreases with increases in applied pressure (i.e. decreases in initial permeability). This is mainly due to more compacted soils having reduced water drainage rates which slows down the speed at which a soil can settle. Consequently, the rate of consolidation will be slower than that occurring in a more permeable version of the same soil, and translates to a smaller coefficient of consolidation. Correlations capturing this relationship can be seen in Equation 79 and Equation 80.

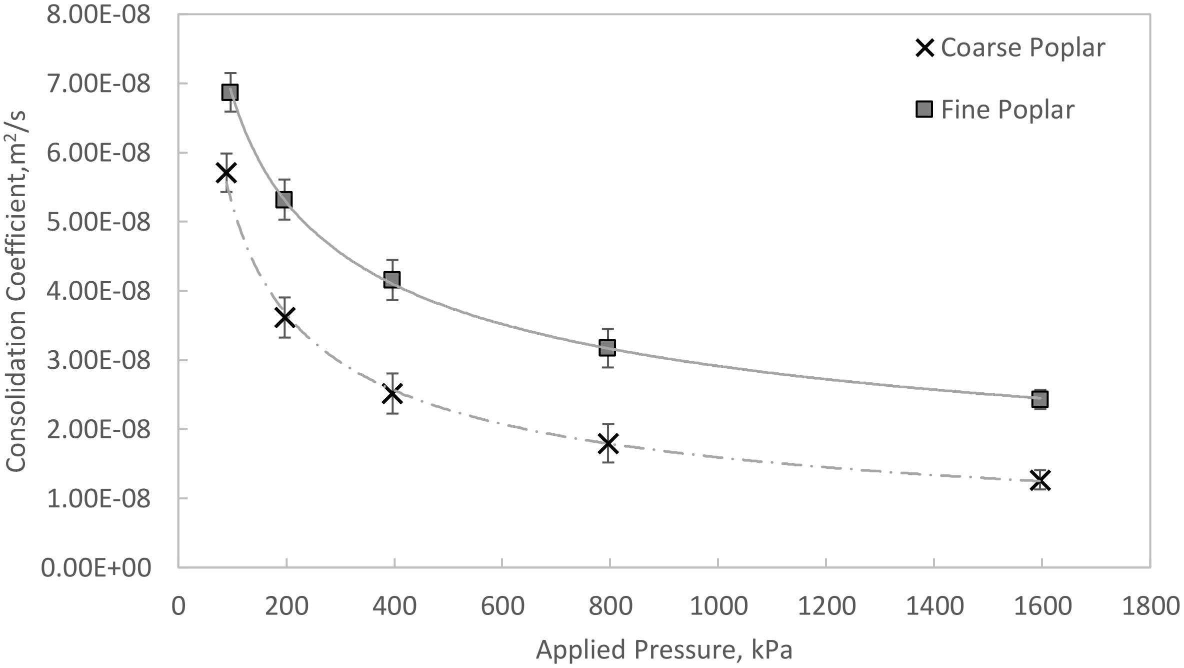

Figure 34: Consolidation Coefficient vs. Applied Pressure for Fine and Coarse Poplar Suspensions

Equation 79: Applied Pressure/ Consolidation Coefficient Correlation for Coarse Poplar Suspensions

$$c_{v,\,R1} = 0.6 \times 10^{-7} \left(\frac{P}{1000}\right)^{-0.518}$$

Equation 80: Applied Pressure/ Consolidation Coefficient Correlation for Fine Poplar Suspensions

$$c_{v,\,R2} = 0.4 \times 10^{-7} \left(\frac{P}{1000}\right)^{-0.37}$$

4.1.4.4. Yield Stress

The yield stresses of the coarse and fine poplar suspensions have been summarized in Table 4, along with the measurements made by Daoxing and Hong (2016) at similar fibre consistencies.

Table 4: Yield stress comparisons with the current study and Daoxing and Hong (2016)

This Study					Daoxing and Hong (2016)			Ratio
Fibre	Consistency	Water Content	Yield Stress (Pa)		Consistency	Yield Stress (Pa)		
POR1	0.21	3.81	4628.4		0.238	529		8.7
	0.16	5.30	1117.2		0.143	416		2.7
POR2	0.40	1.51	5426.4		n/a	n/a		-
	0.33	2.04	2234.4		0.317	853		2.6

Comparing the yield stress results obtained from Daoxing and Hong (2016) to those made on the coarse and fine poplar suspensions, both data show that the yield stress of the fibres increase with increases in fibre consistency. However, the measured yield stresses of the poplar wood fibres were 2.6 to 8.7 times higher than those of the unbleached Kraft pulp wood used in Daoxing and Hong's experiments. Although there seems to exist a sizable discrepancy between the poplar wood fibre measurements and the observations made by Daoxing and Hong (2016), such differences are not uncommon due to the dependence of yield stress on the specific method and technique used for measurement. This is especially evident in methods which rely on curve fitting and methods which rely on direct measurement, as explained by Derakhshandeh et al. (2011), and as demonstrated in a study by Leong-poi and Allen (1992).

In this study, Leong-poi and Allen (1992) measured the yield stress of filamentous broths directly using a lab vane, and indirectly by fitting both the Herschel-Bulkley and Casson models to their shear stress/shear strain data. When comparing the directly measured and fitted yield stress data, the yield stress from the Herschel-Bulkley model was 1.2 to 35.0 times smaller than those from the vane measurements. Based on these observations, the pair proposed that there exists both a static yield stress and a dynamic yield stress. The static yield stress is the yield stress (and corresponding shear rate) that needs to be applied in order to disrupt the fibre network and initiate fibre flow. Once in motion however, a fibrous suspension can continue to flow even below the static yielding shear rate since the rigid network structures in the stagnant suspension are no longer present. If the shear rate is further lowered, the fibrous suspension returns to rest at a new shear rate (and corresponding shear stress) called the dynamic yielding shear rate. This new, dynamic yielding condition is expected to always be lower than the initial, static yielding condition since it does not include the shear required to overcome the network strength of stagnant fibres. With respect to the yield behaviour of coarse and fine fibres, dynamic yield stress measurements were an impossibility due to equipment limitations. However, since the static/dynamic yield ratios were found to be comparable to the findings of Leong-poi and Allen (who noted sizable differences between their static and dynamic yield stress measurements for the same suspension), it was assumed that the poplar suspensions possess the same rheological behaviour as the Kraft pulp fibres experimented upon by Daoxing and Hong (2016), allowing use of their correlations for simulation purposes.

4.2. Simulator Modelling, Validation and Study

4.2.1. Development of TSESimFibre

While significant progress has been made in the development of models and simulators for the mixing and compounding applications of plasticating twin-screw extruders, model development has been significantly slower for those dedicated to fibre-processing and phase-separating. A first attempt at developing a global, composite model and accompanying simulator (TSESimFibre) has been developed for co-rotating, fully intermeshing, phase-separating twin-screw extruders used in wet fibre applications. The model was structured similarly to that proposed by Vergnes et al. (1998) using the cylindrical co-ordinate system, but has been modified to account for the varying rheological differences between liquid polymers and fibrous suspensions, and extended to describe the continuous filtering which occurs in the phase separating sections of the extruder. The resulting model is capable of predicting the down-channel variations of pressure, suspension consistency, filling ratio, mass flow rate (swollen fibre, filtrate) and residence time for a particular set of operating conditions, extruder dimensions and suspension material properties. The simulator was developed in MATLAB 2018b (version 9.5.0.944444), and was based off of Greenfield's fully intermeshing, co-rotating twin-screw extrusion system for wood pulp processing. Validation of TSESimFibre was performed using a commercial twin-screw extruder simulator for plasticating applications (Ludovic, version 6.0.6) in conjunction with trial data from Greenfield. The following subsections detail the logic behind this model and simulator, and also highlight the literature sources used in its creation.

The first step to developing this novel algorithm (and simulator) was to recreate a suitable plasticating extruder algorithm in MATLAB. The plasticating extruder algorithm selected was that proposed by Vergnes et al. (1998), which has been extensively discussed in Section 2.1, and will serve as the basis for modification. Validation was carried out by comparing the results from the MATLAB simulator with the observations recorded in Vergnes et al. (1998), as well as through comparisons with a commercial simulator called Ludovic (version 6.0.1), for the simulation conditions described in Vergnes et al. (1998). These conditions are shown in Figure 35 and Table 6, and the details of the specific screw profile use can be found in Table 5. In Table 5, 'FCSE' indicates forward conveying screw elements and 'RSE' indicates reverse screw elements. The performance of TSESim was found comparable to that obtained by Vergnes et al. (1998), and to the predictions of Ludovic. Graphical comparisons between TSESim and Ludovic can be seen in Figure 36, while

Table 7 allows for comparison of key performance parameters between Ludovic, TSESim and the Vergnes et al. (1998) predictions. From those figures and tables, it could clearly be seen that the MATLAB generated model was capable of yielding predictions comparable to that of other accepted extruder simulators.

TSESim begins calculation at the extruder's exit and proceeds in a manner that opposes the flow direction. This 'back-calculating' technique was employed by Vergnes et al. (1998), and facilitates easier calculation since the parameters at the extruder's exit are generally more defined in contrast to those at its entrance. Consequently, the same technique is used in the design and development of TSESimFibre.

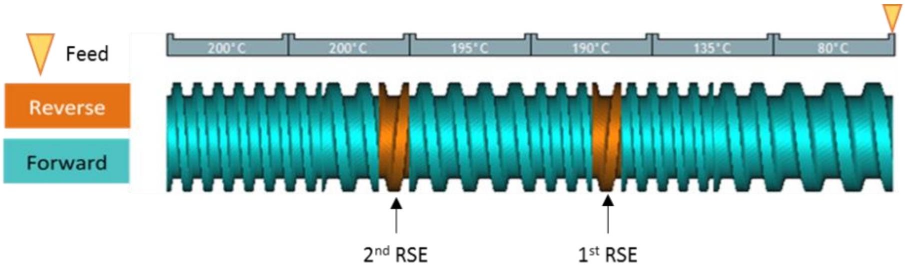

Figure 35: TSESim validation screw profile (Clextral BC 21)

Table 5: Summary of screw elements in validation screw profile (Clextral BC 21)

	Element Type	Pitch/Length(mm/mm)
(die)	FCSE	16.6/25
	FCSE	25/50
	RSE	25/25
	FCSE	25/100
	FCSE	16.6/50
	RSE	25/25
	FCSE	16.6/75
	FCSE	25/50
(hopper)	FCSE	33.3/100

Table 6: TSESim validation parameters: material and operating conditions

Operating Conditions	Mass Flow Rate, kg/min	10
	Rotation Speed, rev/s	4.17
	Exit Pressure, Pa	5,300,000
Material Properties: polypropylene (Vergnes et al. 1998; Ellis and Smith 2008, p.816)	Density, kg/m^3	905
	Consistency, Pa.s^n	2710
	n	0.47
	Heat Capacity, J/kg.K	1926
	Thermal Conductivity, W/m.k	0.117

Table 7: Summary of key performance parameter predictions

Simulator	Outlet Temperature, ^{o}C	Pressure at 2nd Reverse Screw Element, kPa	Pressure at 1st Reverse Screw Element, kPa	Cumulative Residence Time, s
TSESim	234.4	4.0	5.1	20.8
Ludovic	212.2	4.8	5.7	21.4
Vergnes et al. (1998)	~215.0	3.3	4.0	22.0

4.2.1.1. Inputs to TSESimFibre

TSESimFibre requires several different pieces of information before initiation. There are four major information categories that need to be entered:

I. Extruder Specifications – This included definition of the external radius, centreline, and extruder screw profile. A properly define screw profile included the pitch, handedness, screw start and total section length for a series of screw elements of like properties, ordered from the extruder's exit to its entrance.

II. Operating Conditions – This included the mass flow rate of the material, the volumetric flow rate of the wash liquid at the filters, the screw's frequency of rotation and the pressure at the exit of the extruder.

III. Material Properties – This included the composition, consolidation and absorption properties of a fibrous suspension, as well as its rheology. The parameters associated with the suspension's composition were the densities of the constituent fibre (both swollen and dry) and water phases, and the consistency of the resulting mixture they formed. Most of the consolidation parameters were obtained from correlations derived from experiments on the fibrous suspension. Correlations were specified for the coefficient of consolidation (Section 4.1.4.3), the coefficient of volume compressibility (Section 4.1.4.2) and for porosity (Section 4.1.4.1), all of which depended on the instantaneous pressure environment. The liquid absorption coefficient was the only absorption parameter that had to be specified. The rheology of the fibre suspension was governed by correlations proposed by Daoxing and Hong (2016).

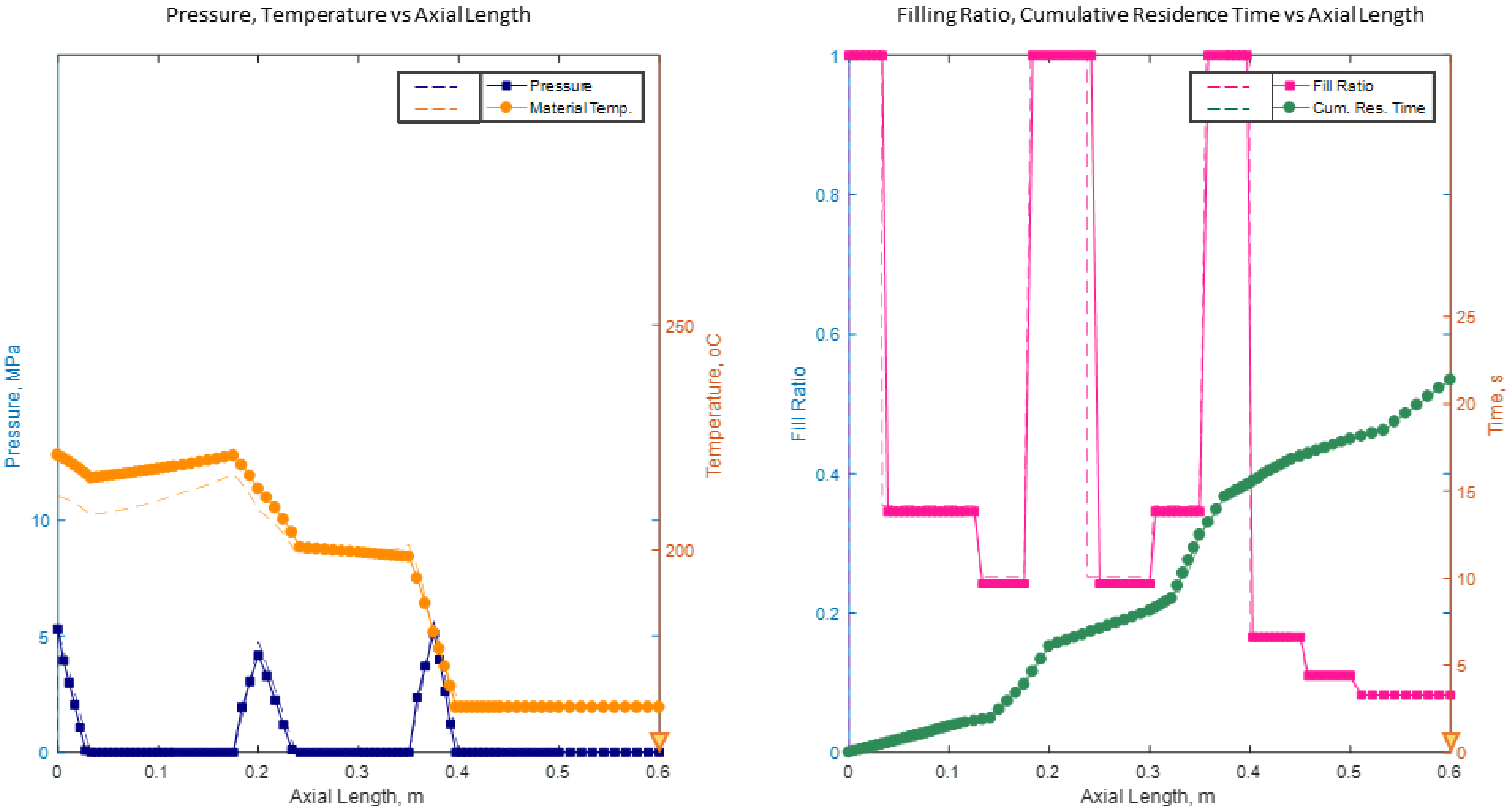

Figure 36: TSESim (markered) vs. Ludovic (dashed) for the conditions outlined in Vergnes et al. (1998)

IV. Loop Controls – This included the Fourier number, step-size, maximum iteration controls and tolerance. For all simulations, the Fourier number selected was 5 since the first five terms were found to be the most impactful on the numerical solution of Terzaghi's Equation. Tolerance was maintained at 0.1 Pa, and a maximum iteration count of 100 was chosen. A step-size of 5 was deemed sufficient to obtain accurate results without excessive computation. This value was selected from a convergence study carried out on the simulator.

4.2.1.2. Step-Size Adjustment

The first step in the simulation was to reinterpret the screw profile in terms of the step size required by the user. The term 'screw profile' refers to the specific arrangement of screw elements that compose the screw of an extruder and for TSESimFibre, it is defined from the extruder's exit and continues to its hopper. The step-size is determined from a 'steps-per-pitch' value selected by the user, and it is obtained by dividing instantaneous pitch by the specific step-per-pitch value specified. The general algorithm used to refine the step-size is shown in Figure 37 below. The algorithm is composed of two loops – an outer loop that controls the section of the screw profile to be sectionalized, and an inner loop that carries out the 'sectionalisation' (the process of adding consecutive step sizes until a required screw section length is reached). Sectionalisation was carried out for all screw elements with the exception of the filtering spacer screw elements, for which calculations were performed over their entire lengths.

4.2.1.3. Conveying Function

Assumptions

1. The fibrous suspension behaves like a non-Newtonian fluid during the extrusion process. This assumption is reasonable based on the observations of numerous researchers (Ventura et al. 2007; Derakhshandeh et al. 2011; Sumida 2013; Daoxing and Hong 2016; Kerekes 2017).

2. The fibrous suspension is composed of the solid (swollen fibres) and liquid (water) phases only; the gaseous phase is completely segregated from the suspension.

3. The rheological properties of the fibrous suspension are accurately captured by the Herschel-Bulkley Model. This model is typically used to describe the rheological properties of fibrous suspensions in the literature (Leong-poi and Allen 1992; Daoxing and Hong 2016).

4. The parameters of the Herschel-Bulkley Model are dependent on the fibre consistency (or water content) and strain rate only. All temperature dependences are ignored.

5. During conveying, most of the water in the fibrous suspension exists as absorbed and free water. While the fraction of interstitial water in the suspension is sufficient to lubricate the fibres and facilitate flow, the amount is small enough to ignore occurrences of liquid backflow in the system. This assumption was validated by observations made from Greenfield’s trial data.

6. No liquid absorption takes place during conveyance.

7. The bulk consistency of the fibrous suspension is assumed equal to the swollen fibre density. This is reasonable when assumptions 2 and 5 are considered.

The material transport in the forward and reverse conveying screw elements was modelled in a manner similar to that used by Vergnes et al. (1998), with some modification. As demonstrated in Section 2.1.2.1 (in particular Figure 9), the equations used for the calculation of upstream pressures, pressure gradients, filling ratios and residence times depended on screw element type (reverse or forward conveying), the presence of upstream restrictive screw elements, and the pressure state. For TSESimFibre, only two of those factors were considered relevant – the screw element type and pressure state. The absence or presence of an upstream restrictive element (i.e. a reverse screw element) dictates the phase of the polymer in Vergnes' model and thus, the type of equations that should be used to calculate a particular parameter. For the case of TSESimFibre however, the wet fibres are always assumed to behave like a non-Newtonian fluid, making such assessments irrelevant.

Another major modification made to the Vergnes model was the removal of temperature and power related calculations due to the assumption of temperature-independent rheological parameters. While studies have shown that the thermal properties of the wood fibres are affected by temperature (MacLean 1941; Radmanović et al. 2014; Kazi et al. 2015), the correlations provided by the literature were only valid for fairly narrow temperature ranges and were not compatible with the operation range of Greenfield’s extruding system. Additionally, measurement of the thermal properties of the biomass was not an available option.

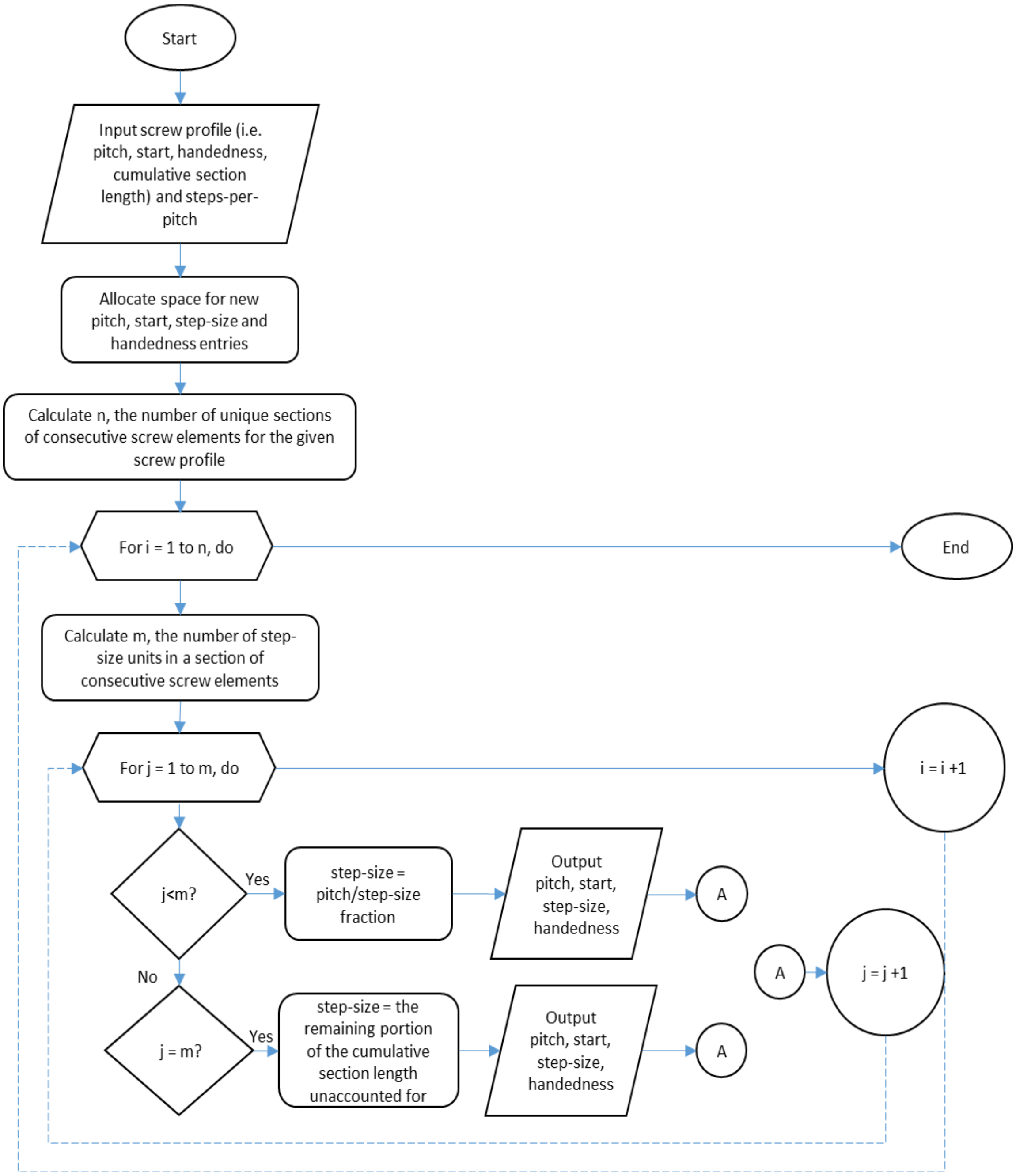

Figure 37: General algorithm for the step-size control function

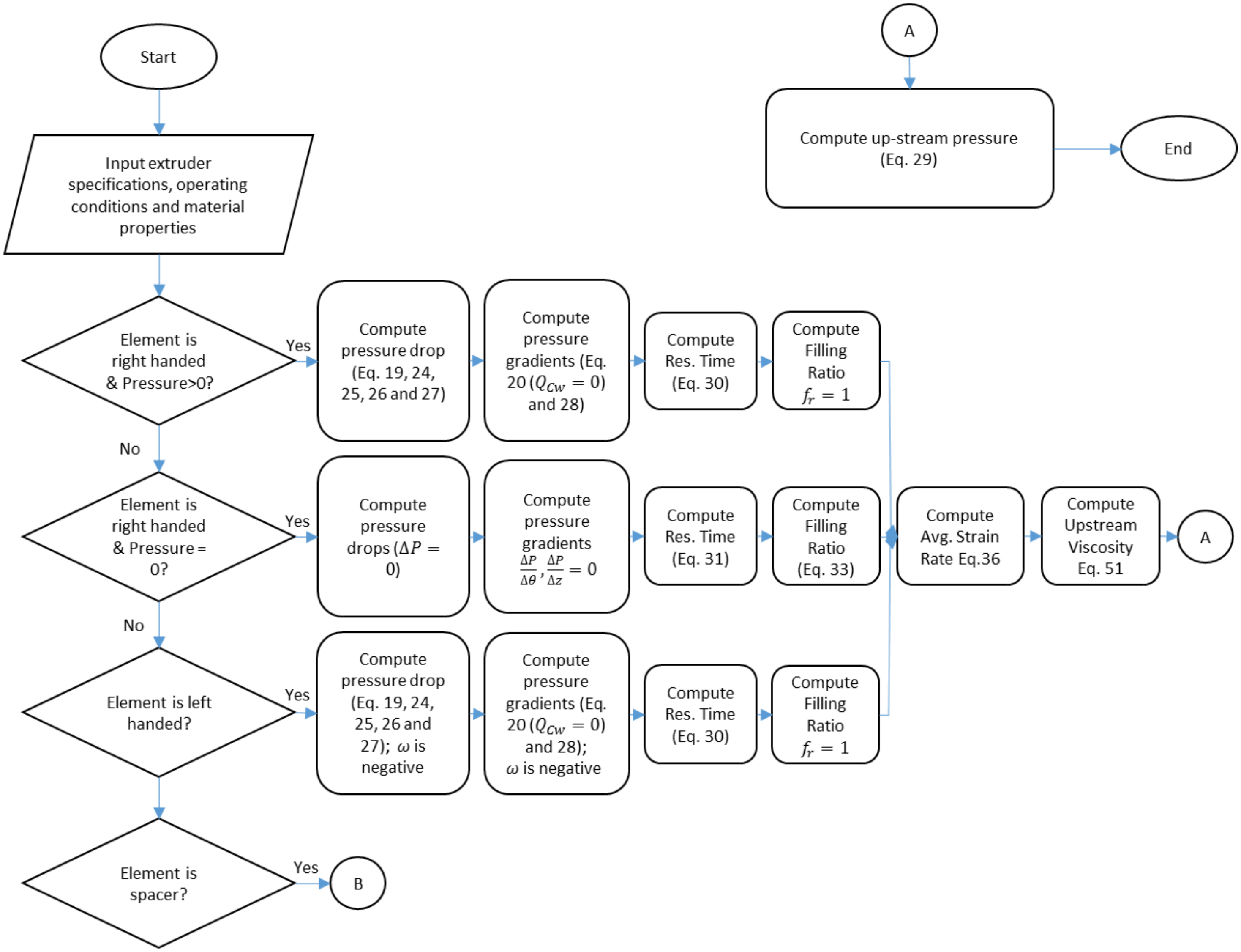

Figure 38: Algorithm for pressure calculations performed by TSESimFibre (part 1) - screw element analysis

The final, modified flow diagram for fibrous suspension conveyance in TSESimFibre is shown in Figure 38 above, and the relevant equations utilized have been included subsequently for convenience. The flow diagram indicates a third, new screw element type – the spacer – which is associated with the filtering aspects of the simulator. The following subsection discusses the workings of the filtering function and its role in TSESimFibre.

Equation 19: Down-channel Volumetric Flow for C-chamber (Ch. 2)

$$Q_{Cv} = f_d \frac{(\omega\, r_E \cos(\beta)) W_C r_E}{2}\left[1 - \left(\frac{r_I^2}{r_E^2 - r_I^2}\right)\left(\ln\left(\frac{r_E}{r_I}\right)\right)^2\right] - f_p \frac{W_C (r_E^2 - r_I^2)}{8\eta}\frac{\Delta P_C}{\Delta\theta_C}\left[1 - \left(\left(\frac{2 r_E r_I}{r_E^2 - r_I^2}\right)\ln\left(\frac{r_E}{r_I}\right)\right)^2\right]$$

Equation 20: Cross-channel Volumetric Flow for C-chamber (Ch. 2)

$$Q_{Cw} = f_d (\omega r_E \sin(\beta)) W_C r_E \left[1 - \left(\frac{1 - \frac{r_I}{r_E}}{\ln\left(\frac{r_E}{r_I}\right)}\right)\right] - f_p \frac{W_C}{4\eta}\frac{\Delta P_C}{\Delta z_C}\left[\frac{2}{3}(r_E^3 - r_I^3) - \left(\frac{r_E^3 + r_I^3 - r_I r_E^2 + r_E r_I^2}{\ln\left(\frac{r_E}{r_I}\right)}\right)\right]$$

Equation 24: Length of C-chamber (Ch. 2)

$$\Delta\theta_C = 2\pi - 2\varphi$$

Equation 25: Volumetric Flow for Intermeshing Region (Ch. 2)

$$Q_{Iv} = f_p \frac{W_I (r_E^2 - r_I^2)}{8\eta}\frac{\Delta P_I}{\Delta\theta_I}\left[1 - \left(\left(\frac{2 r_E r_I}{r_E^2 - r_I^2}\right)\ln\left(\frac{r_E}{r_I}\right)\right)^2\right]$$

Equation 26: Length of Intermeshing Region (Ch. 2)

$$\Delta\theta_I = 2\varphi$$

Equation 27: Pressure Drop across a Single Screw Element (Ch. 2)

$$\Delta P = \frac{1}{2}\left(\frac{V_I \Delta P_I + V_C \Delta P_C}{V}\right) \times \frac{S_S}{B}$$

Equation 28: Pressure Gradient in Complementary Pair of Screw Elements (Ch. 2)

$$\frac{\Delta P}{\Delta \theta} = \frac{\frac{1}{2}\left(\frac{V_I \Delta P_I + V_C \Delta P_C}{V}\right)}{2\pi - \varphi}$$

Equation 29: Up-channel Pressure for Succeeding Pair of Complementary Screw Elements (Ch. 2)

$$P_i = P_{i+1} - \Delta P$$

Equation 30: Residence Time for Fully Filled Screw Channel (Liquid) (Ch. 2)

$$t_R = \frac{V}{Q_{Cv}}$$

Equation 31: Residence Time for Partially Filled Screw Channel (Ch. 2)

$$t_R = \frac{2}{(\cos(\beta))^2}\frac{S_S}{\omega B}$$

Equation 33: Filling Ratio for Partially filled Screws (Ch. 2)

$$f_R = \frac{\dot{m} t_R}{\rho V}$$

Equation 36: Average Strain Rate (for Specified Assumptions) (Ch. 2)

$$\dot{\gamma} = \frac{2}{r_E^2 - r_I^2}\int_{r_I}^{r_E}\left(\left(\frac{dv}{dr} - \frac{v}{r}\right)^2 + \left(\frac{dw}{dr}\right)^2\right)^{\frac{1}{2}} r dr$$

Equation 51: Apparent Viscosity for Herschel-Bulkley Model (Ch. 2)

$$\eta_a = \frac{\tau_0 + K_n \dot{\gamma}^n}{\dot{\gamma}}$$

4.2.1.4. Filtering Function

Another major modification made to the Vergnes et al. (1998) model was the development of an algorithm to predict the behaviour of the filtering sections in Greenfield's twin-screw extruder. The algorithm consisted of two parts - a function that determined the liquid extraction rate associated with a specific inlet filter pressure, and an iterative loop that sought the inlet filter pressure that corresponded to a specific exit filter pressure. These concepts and algorithms are further developed in the successive subsections.

4.2.1.4.1. The bisection Loop

The aim of the iterative portion of the filter function is to determine the inlet pressure that corresponds to the known pressure at the filter's end. The pressure at the beginning of the filter is unknown because TSESimFibre starts calculation at the die of the extruder rather than its hopper. The rational for this unique approach is that there are generally less unknowns at the end of the extruder than at its beginning, making development of a simulator much easier. Of the many iterative schemes available, a 'modified' version of the bisection method was selected for the iteration. The modified bisection method is a variant of the root seeking method which tries to identify the axial location of a particular non-zero response (unlike traditional bisection, which seeks the axial location of zero-valued responses only). Regardless, the premise of both methods is identical. Both methods require the selection of an interval of x-axis values which encloses the axial location of the sought-after response (referred to as the root henceforth), and the successive evaluation of the responses corresponding to the upper, middle and lower points of the interval. A comparison is made between the upper/middle and lower/middle response pairs obtained to determine which half of the x-axis interval contains the root. The section of the axial range within which the root is absent is then disregarded, leaving the remaining portion of the interval for continued assessment. The process of assessing and bisecting is repeated, with each iteration depleting the range of the previous iteration by a factor of two. This process is carried out until the root of the function is obtained within a specified tolerance.

The major advantage of the (modified) bisection method is its guaranteed convergence once a root-enclosed, x-axis interval is provided. Additionally, this method does not require the calculation or estimation of the gradient of the function, which can be impractical at times. Due to its lack of dependence on function gradients, the bisection method is unaffected by the presence of turning points which have been known to cause difficulties for gradient-dependent root-seeking schemes, such as Newton's Method and the Secant Method. However, the bisection method is not without its limitations. A major drawback to its use is that it requires some prior knowledge of a root's location in order to reliably select a suitable x-axis range for assessment. This is particularly the case for even functions (such as the quadratic equation), where the presence of roots may be easily overlooked since these functions cross the x-axis an even number of times. A second drawback is that the bisection method tends to be slower than other root-seeking methods which could be particularly disadvantageous if large, complicated functions need to be assessed.

With respect to TSESimFibre, the modified bisection method was employed to locate the inlet filter pressure (or axial location) corresponding to the exit filter pressure (or root) previously calculated by the conveying function. Calculations were performed at three points over a pre-set bisection range which spanned 0 MPa to 100 MPa. This range was selected because pressures were not expected to exceed 100 MPa in Greenfield's extruding system. The three points selected for evaluation were the extremes of the bisection range, as well as the pressure equalling two times the exit pressure of the filter. The third was selected (in favour of the traditional mid-point assessment) to reduce computation time since the inlet pressure of the filter is not expected to exceed two times the value of its final pressure. Calculations were performed in the manner consistent with the bisection method described earlier, and the specific algorithm used is shown in Figure 39.

To calculate the exit filter pressure associated with a particular inlet filter pressure, a dedicated function was developed. This function considers the effect of both consolidation and absorption, and will be further discussed in the following subsection.

4.2.1.4.2. Consolidation and Absorption

The filter function was a slightly challenging feature to model since filtration is typically a 'batch process', and it has been embedded into a continuously-processing extrusion system. However, the challenge was overcome by realising that for steady state operation, the swollen fibres can spend a maximum amount of time in the filters, which is the residence time (t_R). Therefore, if batch calculations are performed for a time basis equal to the swollen fibre residence time (i.e. calculations are performed on batch quantities obtained from the product of the swollen fibre residence time with the relevant flow rates), effective rates can be determined by simply dividing the final calculated batch quantities by the swollen fibre residence time.

The filter function's major aim is to fulfill two, simple mass balances – the swollen fibre mass balance shown in Equation 81, and the filtrate mass balance shown in Equation 82. The swollen fibre mass balance states that the upstream mass flow rate ($\dot{m}_{sf,i}$) is equal to the downstream mass flow rate ($\dot{m}_{sf,i+1}$) plus the 'mass flow rate' of the water expressed from consolidation ($\dot{m}_{Consolidation}$) less the 'mass flow rate' of the water gained from absorption ($\dot{m}_{absorbed}$). The filtrate mass balance states that the filtrate leaving the spacer ($\dot{m}_{filterate}$) is equal to the mass flow rate of the wash liquid added at the filter ($\dot{m}_{wash\ liquid}$) plus the 'mass flow rate' of the water expressed from consolidation ($\dot{m}_{Consolidation}$) less the 'mass flow rate' of the water gained from absorption ($\dot{m}_{absorbed}$). The unique assumptions and equations used to determine the effective expressed and absorbed liquid flow streams are reviewed in greater detail in the subsequent subsections.

Equation 81: Swollen Fibre Mass Balance

$$\dot{m}_{sf,i} = \dot{m}_{sf,i+1} + \dot{m}_{Consolidation} - \dot{m}_{absorbed}$$

Equation 82: Filterate Mass Balance

$$\dot{m}_{filterate} = \dot{m}_{wash\ liquid} + \dot{m}_{Consolidation} - \dot{m}_{absorbed}$$

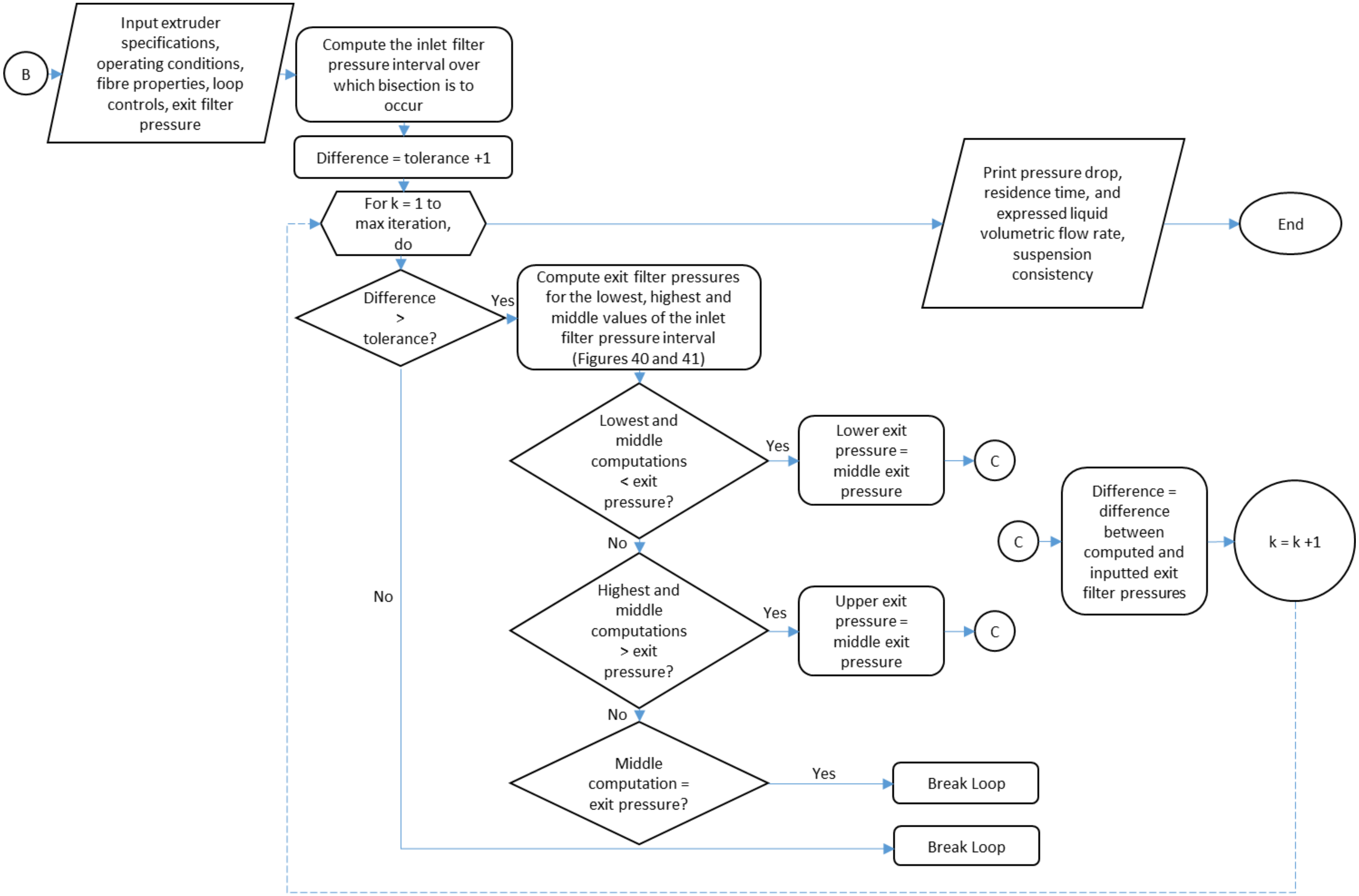

Figure 39: Algorithm for pressure calculations performed by TSESimFibre (part 2) – filter iterative loop

Consolidation

Assumptions

1. The mechanical properties of the fibrous suspension is comparable to fibrous peats, allowing it to be modelled in a similar manner.

2. Terzaghi's Consolidation Theory can accurately describe the consolidation behaviour of the fibrous suspension in the spacer screw elements.
    a. Assumptions of Terzaghi's Consolidation Theory
        - The fully-saturated fibre suspension is homogeneous (i.e. permeability and composition are uniformed throughout).
        - The parameters of the equation (i.e. coefficient of volume compressibility and the coefficient of consolidation) are independent of time.
        - The density of the liquid (water) and solid (swollen fibres) are constant during consolidation.
        - Liquid expression is one dimensional (vertical).
        - Volume changes due to consolidation are small compared to the filter volume.

3. The fibrous suspension behaves like a normally consolidated soil up until the first restrictive screw element (reverse screw element or spacer) is reached. The suspension behaves like an over-consolidated soil in all subsequent downstream screw elements.

4. Primary consolidation is assumed complete at 90% consolidation.

5. Secondary consolidation within the filter is negligible.

From the oedometer and direct shear box tests carried out, it was proven that processed wood fibres shared several commonalities with fibrous peats (Sections 4.1.3 and 4.1.4). Besides their appearance, they share many mechanical similarities which allows for crossover of modelling techniques. To describe the consolidation behaviour of the fibrous suspensions in the filtering screw elements, Terzaghi's consolidation theory (Section 2.2.3.2) was directly borrowed from the geotechnical engineering discipline, despite the existence of its variants in the screw pressing literature (Section b). This decision was made because of the ease with which Terzaghi's theory could be applied, and the ease with which its necessary parameters could be determined.

The underlying assumptions of Terzaghi's Theory also aligned with the assumptions of the continuous filtering section of the twin-screw extruder. The spacers (i.e. the filtering screw elements) are resistive screw elements that do not actively encourage downstream material transport. Consequently, such elements would be fully filled during steady state operation. Although residence time in the spacer varies with the operating conditions of the extruder, it is generally quite small (a few seconds). As a result, time sensitive parameters such as the coefficients of consolidation and volume compressibility are not expected to vary significantly during the consolidation process. The extremely short residence time also allows one to assume a near-constant suspension volume and swollen fibre density in the filter, and the existence of negligible internal porosity and suspension consistency gradients. These are reasonable assumptions since only a small amount of fluid will be expressed per 'batch' of consolidated fibres.

The assumption of normally and over-consolidated soil has been applied to account for the stress history of the fibrous suspension during processing. It is assumed that before reaching the first restrictive screw element in the screw profile, the pressure history of the fibrous suspension is negligible, allowing it to be modelled as a normally consolidated soil experiencing both plastic and elastic deformation upon compression. After surpassing the first restrictive screw element however, the suspension has been compressed and relaxed, and now has a history of prior stress exposure. This prior compression history means that recompression of the suspension downstream only causes elastic deformation to occur (if the magnitude of the previously applied pressure is not surpassed). To account for this occurrence, the suspension is modelled as an over-consolidated soil. This assumption only affects consolidation modelling in the filter, and is reasonable since the pressures associated with the filters are small compared to the pressures generated elsewhere in the extruder.

The last two assumptions are commonly made in geotechnical engineering consolidation problems. Secondary consolidation is generally much smaller than primary consolidation, and is therefore ignored during phases of significant primary consolidation. Primary consolidation is generally taken to be complete at 90% since it takes an infinite amount of time for a material to be 100% consolidated, in theory. The final flow diagram for the consolidation calculations can be seen in Figure 40 below, and the relevant equations utilized have been included subsequently for convenience.

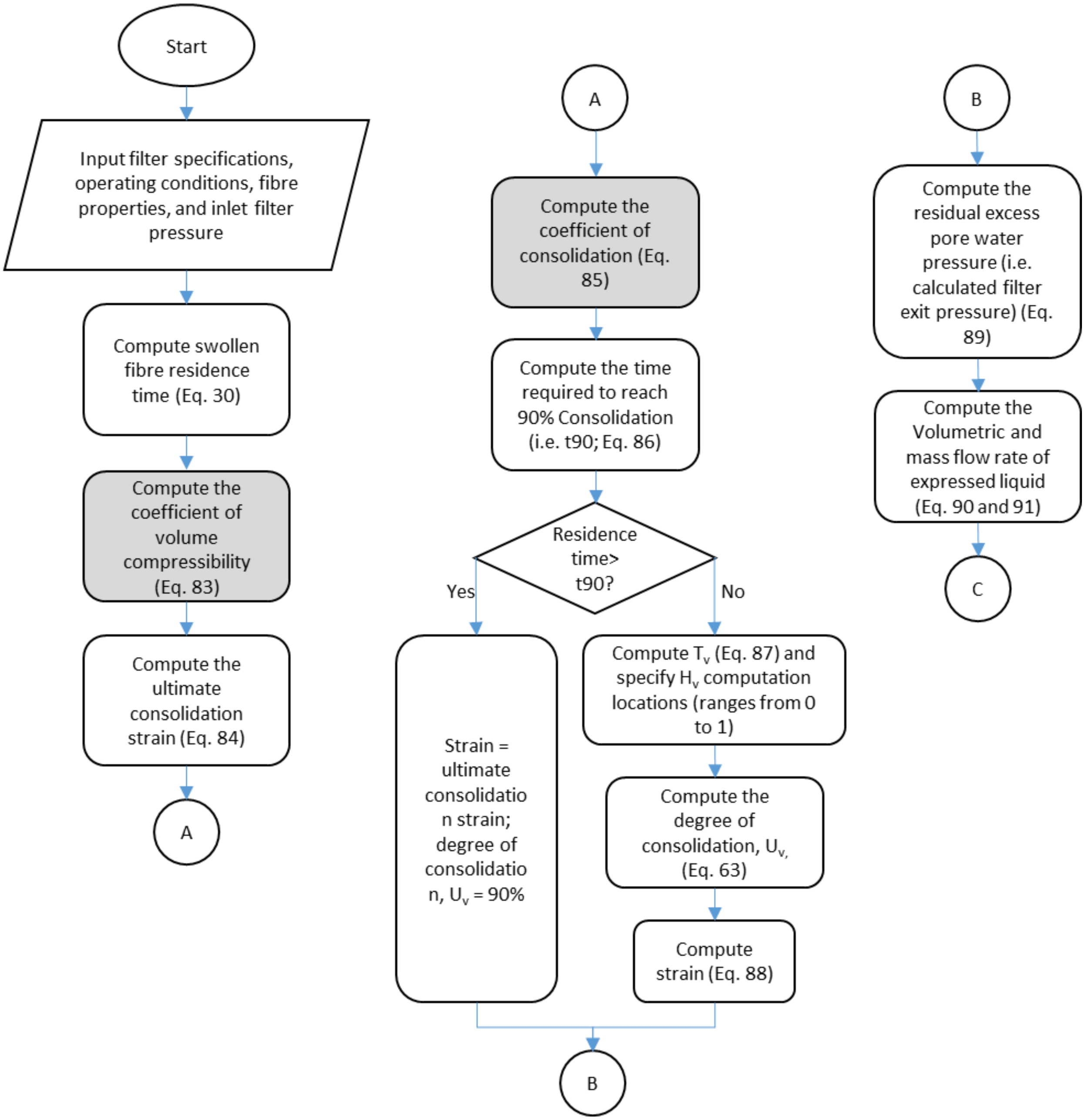

Figure 40: Algorithm for pressure calculations performed by TSESimFibre (part 3) – liquid expression from consolidation

Equation 63: Degree of consolidation (vertical) from Terzaghi's Equation (Ch. 2)

$$u_v = 1 - \sum_{i=0}^{\infty}\left(\frac{4}{(2i+1)\pi}\sin\left[\frac{(2i+1)\pi}{2}h_v\right]e^{-\left[\left(\frac{(2i+1)\pi}{2}\right)^2 T_v\right]}\right)$$

Equation 83: Correlation for coefficient of volume compressibility (PO R1)

$$m_v = \frac{m_{v,R2}w + m_{v,R1}(L-w)}{L}$$

$$where\ m_{v,R1} = 0.539\left(\frac{P_v}{1000}\right)^{-1.08}$$ *(Equation 77, Ch. 4)*

$$and\ m_{v,R2} = 0.1814\left(\frac{P_v}{1000}\right)^{-0.95}$$ *(Equation 78, Ch. 4)*

Equation 84: 90% consolidation strain

$$\gamma_{max} = 0.90m_v\left(\frac{P_v}{1000}\right)$$

Equation 85: Correlation for coefficient of consolidation (PO R1)

$$c_v = \frac{c_{v,R2}w + c_{v,R1}(L-w)}{L}$$

$$where\ c_{v,R1} = 0.6\times10^{-7}\left(\frac{P_v}{1000}\right)^{-0.518}$$ *(Equation 79, Ch. 4)*

$$and\ c_{v,R2} = 0.4\times10^{-7}\left(\frac{P_v}{1000}\right)^{-0.37}$$ *(Equation 80, Ch. 4)*

Equation 86: Time to Reach 90% Consolidation

$$t_{90} = \frac{T_v(2r_E)^2}{c_v}$$

$$where\ T_v\ is\ 0.848\ at\ 90\%\ \text{consolidation}$$

Equation 87: Compute dimensionless time, T_v

$$T_v = \frac{t_R c_v}{(2r_E)^2}$$

Equation 88: Instantaneous strain (at consolidation < 90%)

$$\gamma = u_v \gamma_{max}$$

Equation 89: Residual pore water pressure

$$P_{exit} = (1 - u_v)P_v$$

Equation 90: Effective Volumetric flow rate of expressed liquid

$$Q_{Consolidation} = \frac{\gamma S_s (A_{AB} - \pi r_I^2)}{t_R}$$

$$where\ S_s(A_{AB} - \pi r_I^2)\ is\ the\ volume\ of\ the\ filter$$

Equation 91: Effective mass flow rate of expressed liquid

$$\dot{m}_{Consolidation} = \rho_l Q_{Consolidation}$$

NB: The subscripts ‘$R1'$ and $'R2'$ denote the coarse and fine poplar suspensions respectively.

Absorption

<u>Assumptions</u>

1. The absorption behaviour of the fibrous suspension is comparable to that of wood.

2. The wood fibres are randomly oriented in the fibrous suspension.

The mass of water absorbed by wood fibres can easily be determined from a correlation by Krus & Kunzel (Lepage 2012), as discussed in Section 2.2.1.2. Use of this correlation to model absorption in the filters is not unreasonable since the processed material is a suspension of wood fibres in water only. The correlation yields the mass of water absorbed per unit area of wetted surface when the absorption coefficient and wetting time of the wood is known. To obtain the wetted surface area of the fibres, the Kozeny-Carman Equation (for calculation of specific surface area) was solicited along with knowledge of the total mass of swollen fibres in the filter. The Kozeny-Carmen Equation requires the specification of a Kozeny constant, which depends on both the shape and orientation of the particles. Assuming that the wood fibres are randomly oriented fibres, a Kozeny constant valued at 4.5 may be utilized. The assumption of 'random orientation' is not unreasonable for the fibres being processed in the shear-intensive extruding environment, and has been made elsewhere (Westenbroek 2000).

Figure 41 shows the flow diagram used to determine the mass of water absorbed by the fibres while in the filter. The flow diagram goes on to integrate the mass balances in Equation 81 and Equation 82 discussed earlier, and also determines the upstream, pre-filtration consistencies and densities. Again, the relevant equations utilized have been included subsequently for convenience.

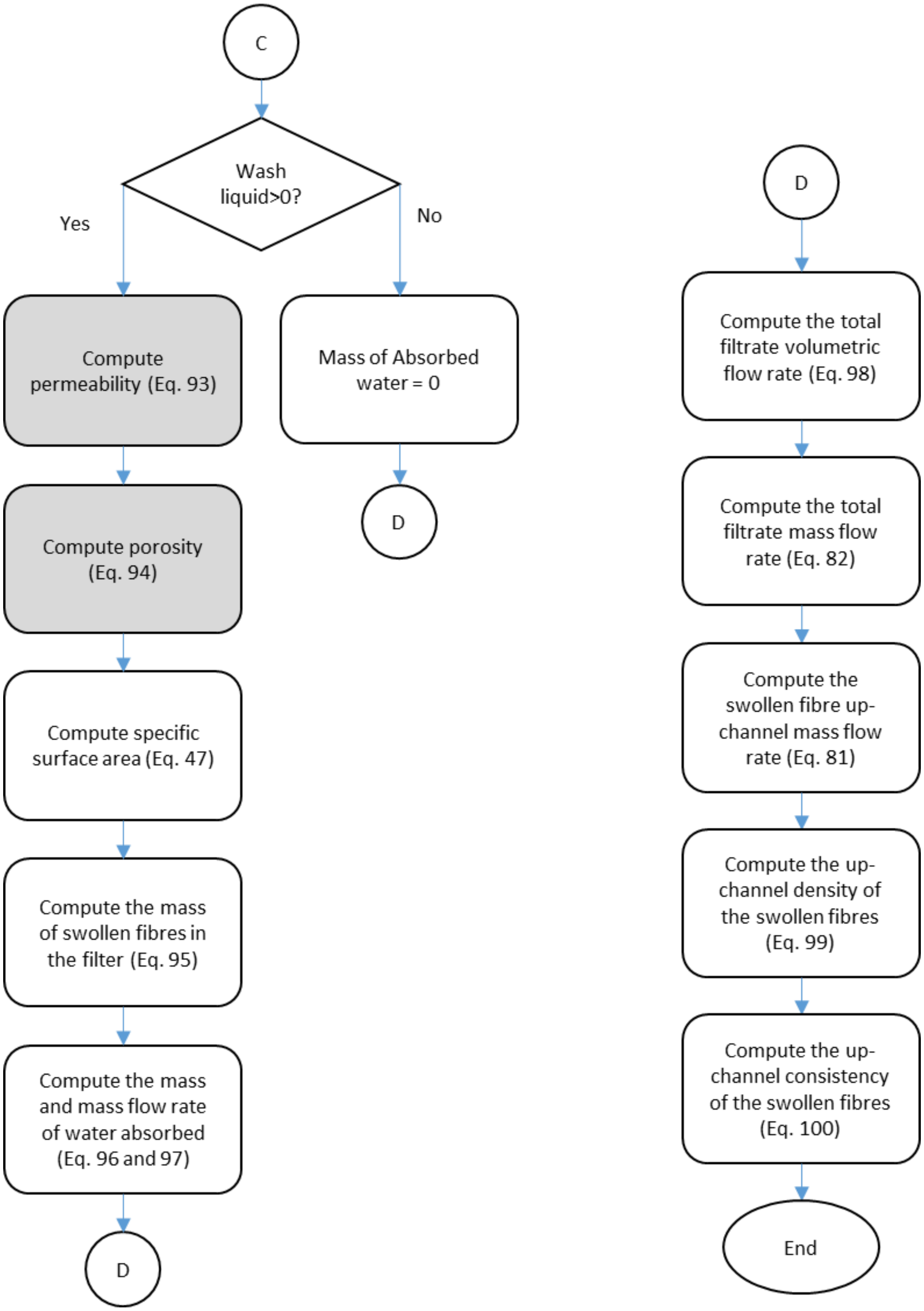

Figure 41: Algorithm for pressure calculations performed by TSESimFibre (part 4) – wash liquid fibre absorption

Equation 47: Kozeny-Carman Equation (Ch. 2)

$$K = \frac{n_p^3}{k_{kc} S_a^2 (1 - n_p)^2}$$

$$where\ k_{kc}\ is\ 4.5\ assuming\ randomly\ oriented\ fibres$$

Equation 81: Swollen Fibre Mass Balance (Ch. 4)

$$\dot{m}_{sf,i} = \dot{m}_{sf,i+1} + \dot{m}_{Consolidation} - \dot{m}_{absorbed}$$

Equation 82: Filterate Mass Balance (Ch. 4)

$$\dot{m}_{filtrate} = \frac{Q_{filterate}}{\rho_l} = \dot{m}_{wash\ liquid} + \dot{m}_{Consolidation} - \dot{m}_{absorbed}$$

Equation 92: Correlation for permeability coefficient (PO R1)

$$K = \frac{K_{R2} w + K_{R1}(L - w)}{L}$$

$$where\ K_{R1} = 3 \times 10^{-4} \left(\frac{P_v}{1000}\right)^{-1.609}$$ *(Equation 71, Ch. 4)*

$$and\ K_{R2} = 7 \times 10^{-5} \left(\frac{P_v}{1000}\right)^{-1.321}$$ *(Equation 72, Ch. 4)*

Equation 93: Correlation for porosity (PO R1)

$$n_p = \frac{n_{p,R2} w + n_{p,R1}(L - w)}{L}$$

If normally consolidated

$$where\ n_{p,R1} = 0.5983 e^{-0.001\left(\frac{P_v}{1000}\right)}$$ *(Equation 73, Ch. 4)*

$$and\ n_{p,R2} = 1 \times 10^{-7} \left(\frac{P_v}{1000}\right)^2 - 4 \times 10^{-4} \left(\frac{P_v}{1000}\right) + 0.659$$ *(Equation 75, Ch. 4)*

If over consolidated

$$where\ n_{p,R1} = -0.049\log\left(\frac{P_v}{1000}\right) + 0.4623 \quad \text{(Equation 74, Ch. 4)}$$

$$where\ n_{p,R1} = -0.022\log\left(\frac{P_v}{1000}\right) + 0.5089 \quad \text{(Equation 76, Ch. 4)}$$

Equation 94: Swollen Fibres in Filter

$$m_{sf} = \dot{m}_{sf}t_R$$

Equation 95: Mass of Absorbed Wash Liquid

$$m_a = k_{asb}(S_a m_{sf})\sqrt{t_R}$$

$$'S_a m_{sf}'\ is\ the\ surface\ area\ of\ the\ fibres$$

Equation 96: Effective absorbed liquid mass flow rate

$$\dot{m}_{absorbed} = \frac{m_a}{t_R}$$

Equation 97: Filtrate volumetric flow rate

$$Q_{filterate} = Q_{wash\ liquid} + Q_{Consolidation} - \frac{\dot{m}_{absorbed}}{\rho_l}$$

Equation 98: Up-channel Swollen Fibre Density

$$\rho_{sf,i} = \rho_{sf,i+1} + \frac{\dot{m}_{Consolidation}t_R}{S_s(A_{AB} - \pi r_I^2)} - \frac{m_a}{S_s(A_{AB} - \pi r_I^2)}$$

$$where\ S_s(A_{AB} - \pi r_I^2)\ is\ the\ volume\ of\ the\ filter$$

Equation 99: Up-channel Swollen Fibre Consistency

$$x_{c,i} = \frac{\rho_{f,dry}}{\rho_{sf,i}}$$

NB: The subscripts '$R1$' and '$R2$' denote the coarse and fine poplar suspensions respectively.

4.2.1.5. Initialization of TSESimFibre

Initialization of the TSESimFibre simulator mandates the calculation of four major variables – viscosity, down-channel pressure drop and the down- and cross-channel pressure gradients. All calculations are based on the geometry of the screw element fraction that is first assessed, which is the screw element at the extruder's exit. Initialization begins by calculating the intermeshing, flight land and helix angles using Equation 1, Equation 2 and Equation 3 respectively. With these angles defined, the c-chamber and intermeshing region volumes and widths can be calculated using Equation 4, Equation 5, Equation 9 and Equation 11. To calculate an initial viscosity, flow through the c-chamber is likened to the one dimensional flow through a pair of parallel plates. In this analogy, the barrel is representative of the top plate while the average screw channel depth is representative of the gap between the plates. The average shear rate can finally be calculated from Equation 100. This value is assumed identical to the average strain rate since fluid expansion is zero for the parallel plate assumption. With the average strain rate defined, an initial fluid viscosity can be calculated using Equation 51. The average down-channel pressure drop and the down- and cross-channel pressure gradients can finally be obtained using Equation 19, Equation 20 and Equation 24 to Equation 28.

Equation 100: Shear Rate Calculation for Initialization of the TSE Function

$$\dot{\gamma} = \frac{\omega r_E}{h}$$

4.2.2. Twin-screw Extruder Geometry, Screw Profile, Operating Conditions and Materials (Extruder 2)

4.2.2.1. Extruder Geometry

1. Outer screw radius: 35 mm
2. Mechanical flight clearance: 0 mm
3. Outer radius/Inner radius ratio: 1.71
4. Inner radius: 20.5 mm
5. Maximum channel depth: 35 – 20.5 = 14.5 mm
6. Centerline distance: 70 – 14.5 = 55.5 mm

4.2.2.2. Operating Conditions

7. Extruder length, screw configuration 18: 4357.5 mm
8. Extruder length, screw configuration 21: 4352.5 mm
9. Screw rotational frequency: 315 rpm (max: 350 rpm)
10. Pressure at hopper: 85 – 120 psig (currently 85 psig or 586 kPa)
11. Pressure at die: 210 – 230 psig (currently 210 psig or 1448 kPa)
12. Temperature at hopper: 155 ^{o}C (428.15 K)

4.2.2.3. Materials

13. Average dry fibre mass flow rate: 91.5 kg/s
14. Dry fibre density (based on swollen fibre volume): 201.5 kg/m^3
15. Swollen fibre density at die: 730.0 kg/m^3
16. Extruder surface material: stainless steel

The screw profiles for screw configuration 18 and 21 can be seen in Table 8, where ‘FCSE’ indicates forward conveying screw elements, ‘RSE’ indicates reverse conveying screw elements and ‘S’ indicates spacer screw elements.

Table 8: Summary of Greenfield's screw configurations (Extruder 2)

	Screw Configuration 18				Screw Configuration 21					
	First Variant		Original		First Variant		Second Variant		Original	
	Element Type	Pitch/Length (mm/mm)	Element Type	Pitch/Length (mm/mm)	Element Type	Pitch/Length (mm/mm)	Element Type	Pitch/Length (mm/mm)	Element Type	Pitch/Length (mm/mm)
(Die)	FCSE	45/225	FCSE	45/225	FCSE	45/100	FCSE	45/100	FCSE	45/100
	FCSE	60/360	FCSE	60/360	FCSE	60/450	FCSE	60/450	FCSE	60/450
	FCSE	90/180	FCSE	90/180	RSE	60/75	RSE	60/75	RSE	60/75
	RSE	60/60	RSE	60/60	FCSE	60/65	FCSE	60/65	FCSE	60/65
	FCSE	60/35	FCSE	60/35	FCSE	90/180	FCSE	90/180	FCSE	90/180
	FCSE	45/45	FCSE	45/45	FCSE	60/30	FCSE	60/30	FCSE	60/30
	FCSE	90/90	FCSE	90/90	FCSE	90/90	FCSE	90/30	FCSE	90/90
	FCSE	60/155	FCSE	60/30	FCSE	60/215	FCSE	90/30	FCSE	60/60
	FCSE	45/450	S	10/70	FCSE	45/450	FCSE	90/30	S	10/40
	FCSE	60/720	FCSE	60/30	FCSE	60/660	FCSE	60/30	FCSE	60/30
	FCSE	90/180	S	10/10	FCSE	90/90	FCSE	60/30	S	10/85
	FCSE	60/85	FCSE	45/450	FCSE	60/155	S	10/40	FCSE	45/450
	FCSE	45/250	FCSE	60/720	FCSE	45/45	FCSE	60/115	FCSE	60/660
	FCSE	60/510	FCSE	90/180	FCSE	60/510	FCSE	45/450	FCSE	90/180
	FCSE	90/180	FCSE	60/30	FCSE	90/180	FCSE	60/660	FCSE	60/60
	FCSE	135/67.5	S	10/55	FCSE	135/67.5	FCSE	90/180	S	10/40
	FCSE	180/765	FCSE	45/45	FCSE	180/765	FCSE	60/155	FCSE	60/30
			S	10/25			FCSE	45/180	S	10/25
			FCSE	45/180			FCSE	60/510	FCSE	45/180
			FCSE	60/510			FCSE	90/180	FCSE	60/510
			FCSE	90/180			FCSE	135/67.5	FCSE	90/180
			FCSE	135/67.5			FCSE	180/765	FCSE	135/67.5
(hopper)			FCSE	180/765					FCSE	180/765

4.2.3. Validation

The validation of TSESimFibre was carried out at various stages during its programming. This multistage validation process was necessary since the relevant data required for comparison with the completed simulator could not be obtained by Greenfield due to operation limitations. Data, such as axial pressure measurements and cumulative residence time, were impractical to measure due to the unique nature of the material being processed and because the extruder could not be isolated from Greenfield's pre-treatment system for dedicated testing. The multistage validation process was performed in two stages. In the first stage, TSESimFibre's ability to predict the transport of a two-phased fibrous suspension for the hypothetical screw profiles shown in Figure 42 are compared to the prediction capabilities of the commercial extrusion simulator, Ludovic, for comparable testing conditions. Additionally, the dependence of the simulation results from TSESimFibre on step-size was investigated. The second stage of the validation focused on the unique spacer screw element arrangements that Greenfield utilized to achieve phase separation of their fibrous suspensions. This stage of the validation process was also carried out in two phases, the first of which being a parameter fitting exercise to estimate an unmeasurable fibre absorption coefficient, and the second, comparisons between the liquid extraction rates predicted by TSESimFibre and those measured from Greenfield's extrusion system.

4.2.3.1. Stage 1a: Comparisons with Ludovic

The simple transport predicting capabilities of TSESimFibre are compared with those of Ludovic for the two screw configurations shown in Figure 42, for the same testing conditions. It is important to emphasize that the filtering capabilities of TSESimFibre are not assessed at this moment. Both screw profiles were entirely composed of forward and reverse conveying screw elements, and had diameter and centreline dimensions of 70 mm and 55.5 mm in accordance with Greenfield's extruding system. All assessments were carried out at a fibrous suspension consistency of 20%, which was constant throughout the simulation. For a dry fibre density of 201.5 kg/m^3 and dry fibre mass flow rate of 92.7 kg/s, this corresponds to a swollen (and bulk) fibre density of 1007.3 kg/m^3 and swollen fibre mass flow rate of 463.3 kg/s. It should be pointed out that the dry fibre density presented above was calculated based on the swollen fibre volume (determined from the volumetric shrinkage value for yellow poplar presented in Ross (2010, p. 4-6)) instead of the dry fibre volume; the true dry fibre density for the poplar fibres is 230.8 kg/m^3.

The exit pressure for both cases was 1.45 MPa (gauge), while the inlet pressure was atmospheric (0 gauge). Viscosity was temperature independent and was dictated by the correlations provided by Daoxing and Hong (2016). All simulations were carried out using a screw speed of 315 rpm.

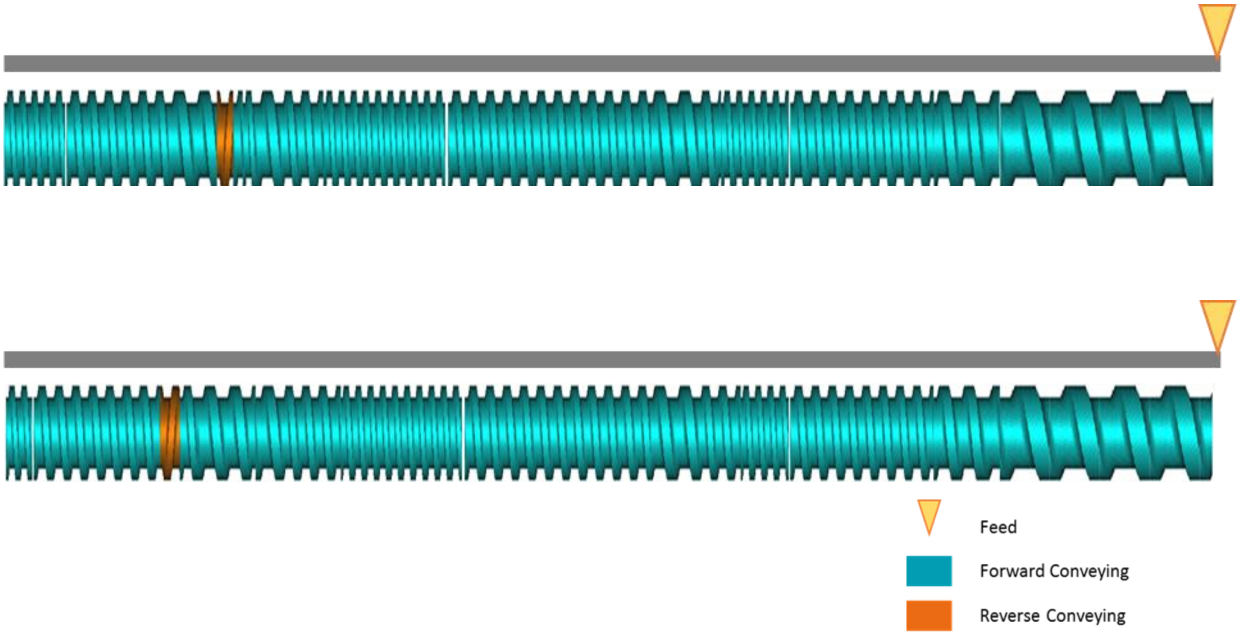

Figure 42: First variant of Greenfield's screw configuration 18 (top) and screw configuration 21 (bottom)

From Figure 43 and Figure 44, it could be seen that the two simulators give similar results, although the predictions from TSESimFibre varied at a few distinct locations. Most of the differences may be due to the use of additional shape factor correlations to help correct for nuances in the mathematical description of the screw's geometry. This is possibly the case for the difference observed between the two pressure profiles in the axial region located between 2.0 m and 2.5 m, since variables like the axial pressure profile are particularly sensitive to such. The differences in the predicted pressure profiles also affected other aspects of the simulation, such as the filling ratio profiles. A filling ratio of one is only assigned to pressurized screw elements and since TSESimFibre predicts a greater portion of the screw profile to be pressurized, it is only natural that it predicts a greater portion of the screw profile to be fully filled as well. The difference in filling ratio between the axial locations of 3.0 m and the beginning of the extruder may be due to a correction factor implemented by Ludovic to account for the initial uncompressed state of polymer powders or pellets fed into the extruding system. Such an assumption is not unreasonable when one remembers that Ludovic is a simulation software developed for predicting the performance of plasticating twin-screw extruders. However, TSESimFibre was developed on the assumption that the wet fibres fed into the extruder only contain two phases – a solid phase and a liquid phase – and does not account for the effect of a gaseous phase on the system, resulting in smaller filling ratio values in the same axial region.

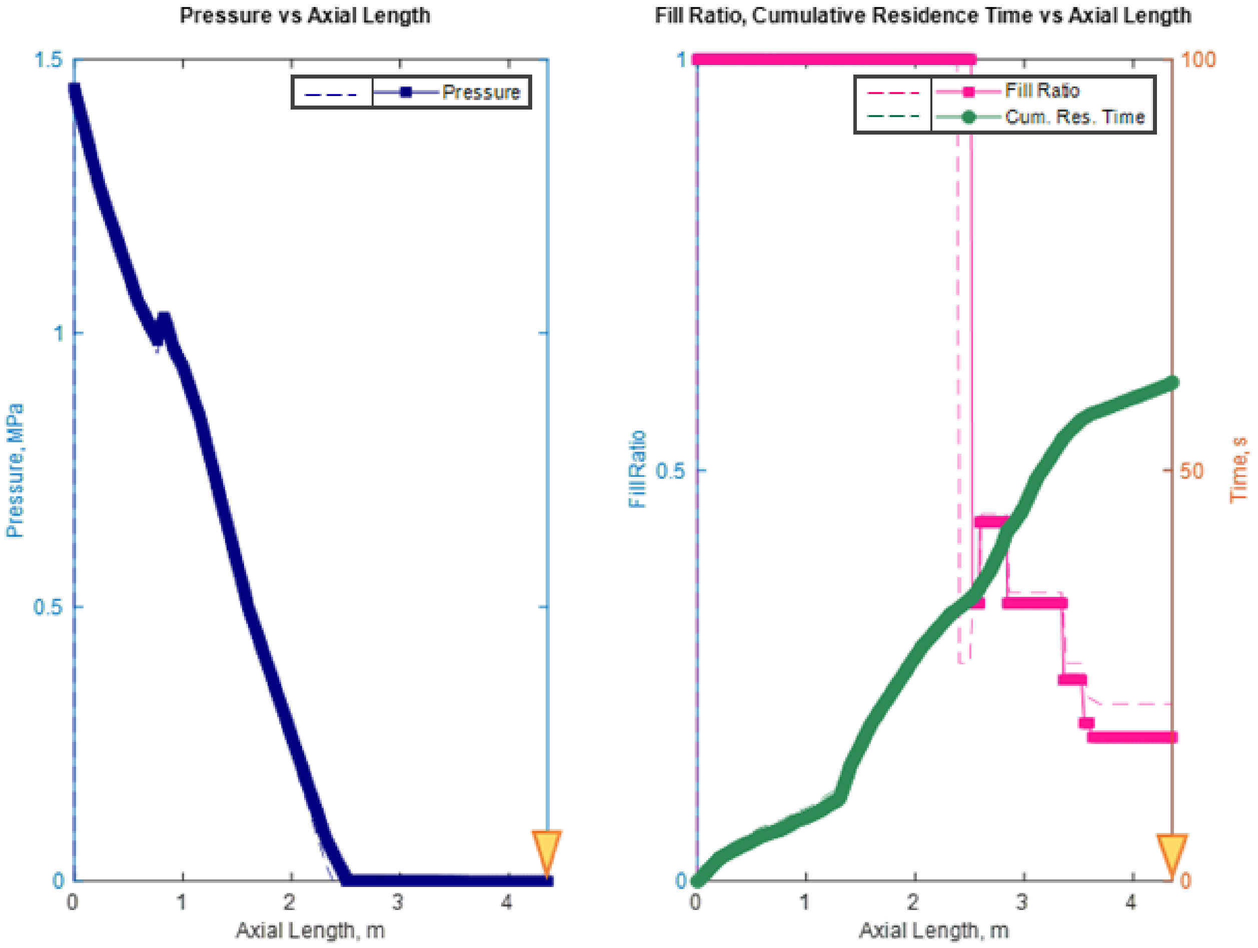

Figure 43: Ludovic (dashed) and TSESimFibre (markered) simulation comparisons for screw configuration 18, first variant

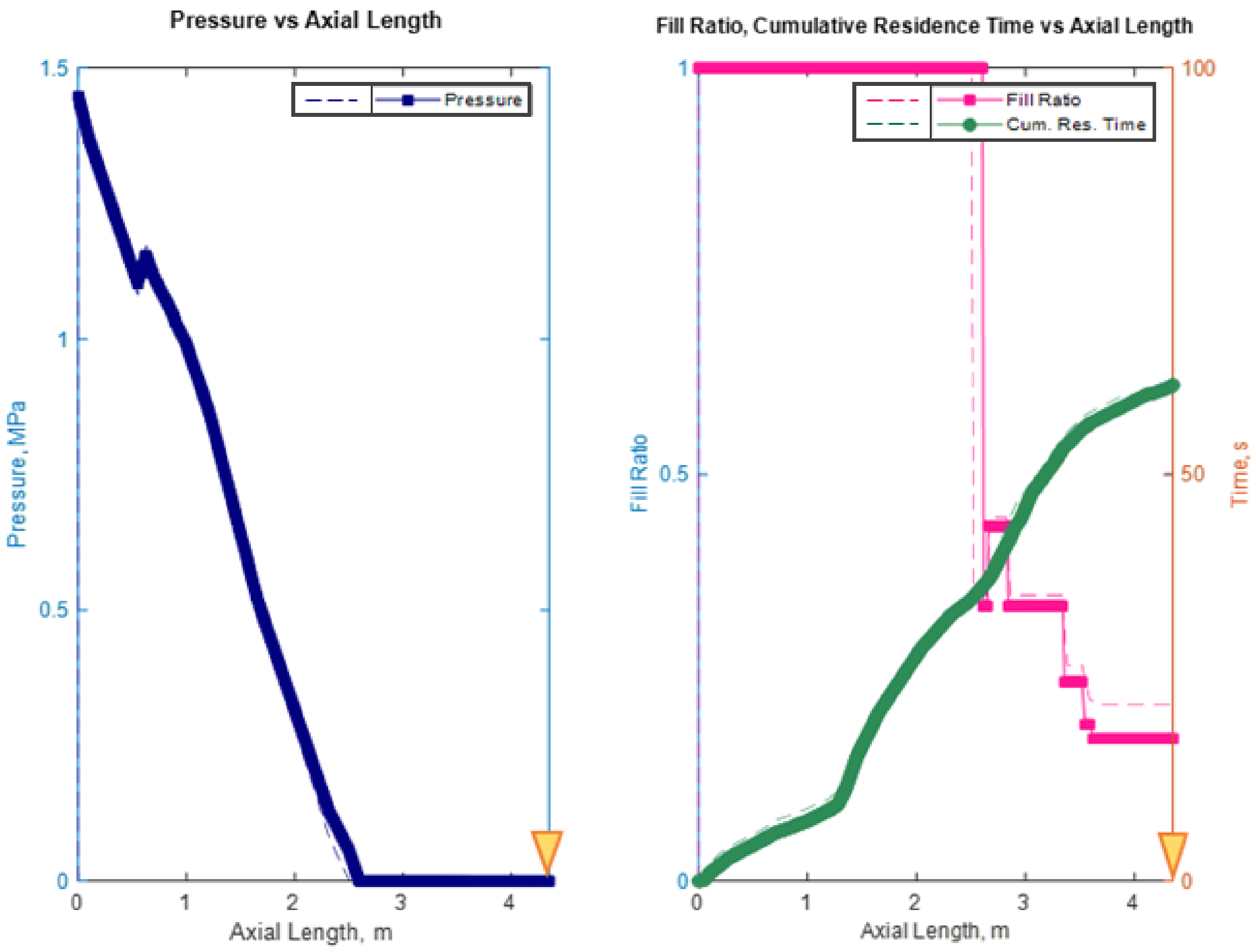

Figure 44: Ludovic (dashed) and TSESimFibre (markered) simulation comparisons for screw configuration 21, first variant

4.2.3.2. Stage 1b: Evaluating Step Size Independence

After validations with Ludovic, the effect of step size on the simulations was evaluated by noting how pivotal outputs were affected as step size was varied. The evaluations were carried out using the screw profiles shown in Figure 42, and using the conditions specified in the previous subsection. The monitored outputs were the cumulative residence time of the fibres within the extruder, and the maximum pressure at the reverse screw element. Step size was determined from the 'step-per-pitch' values inputted by the user. The evaluated step-per-pitch values were 1, 2, 5, 10, 15 and 30, and the step size in each case was obtained by dividing instantaneous pitch by the specific step-per-pitch value specified. From Figure 45 and Figure 46, it could clearly be seen that the predicted values for pressure and cumulative residence time became independent of step size, and converged to a single value as the number of steps-per-pitch increased. For both cases, the results obtained when using step-per-pitch values of 2 or higher yielded simulation results that fell within 10% of the step size independent result. Based on these observations, a step-per-pitch value of 5 was thought most suitable for further assessments, as it yielded results that were nearly step size independent without excessive computations.

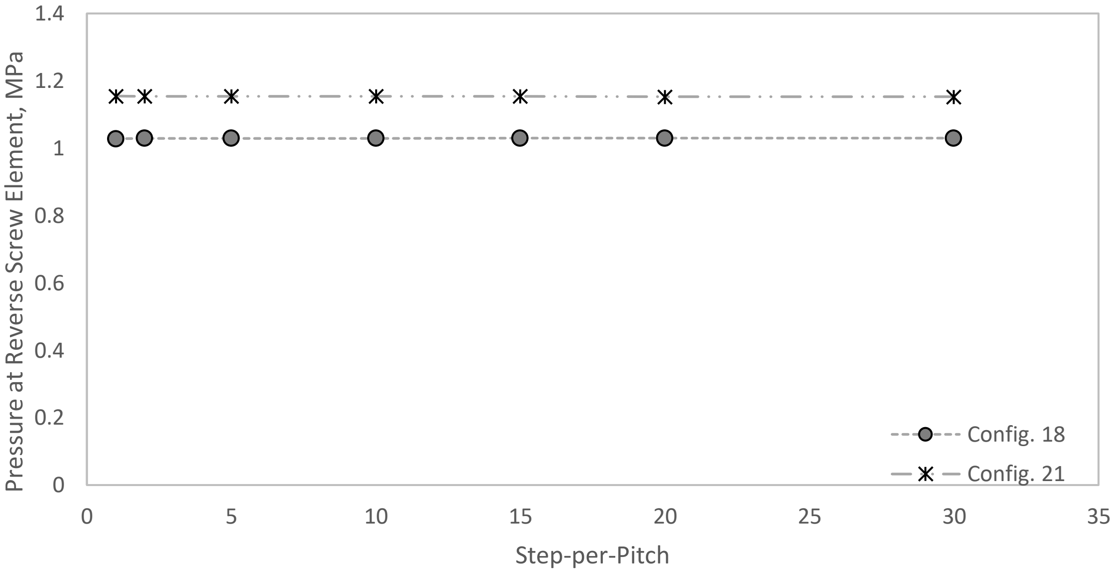

Figure 45: Effect of step size on reverse screw element pressure predictions

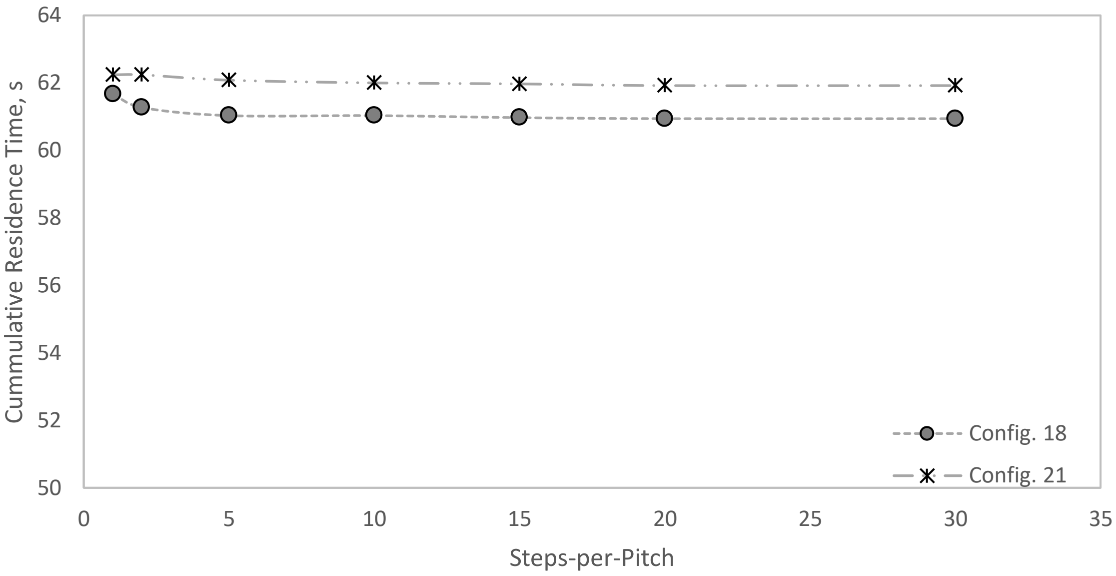

Figure 46: Effect of steps-per-pitch on cumulative residence time predictions

4.2.3.3. Stage 2a: Absorption Coefficient Fitting using Screw Configuration 21

The value of the liquid absorption coefficient was determined by ‘fitting’ the ‘TSESimFibre model’ to one of Greenfield’s trial datasets. The dataset selected was that corresponding to the screw configuration 21 trials, for which the accompanying configuration is shown in Figure 47. This trial data was selected over the alternative (the screw configuration 18 trial dataset) because it was the most complete of the available options, and would therefore provide a more accurate estimation of the desired absorption parameter to be determined. The trials carried out by Greenfield are a compilation of different cases which explore the effect of wash liquid flow rate (at the filters) on the filtrate flow rate. During each trial, the extruder dimensions, screw profile, screw rotational speed and inlet/outlet pressures are not varied. The monitored parameters relevant to this fitting include the dry matter mass flow rate (i.e. the mass flow rate of the dried fibres) and the rate at which liquid is extracted from the system from all filters (i.e. the net filtrate flow rate). These parameters were generally measured at one hour time intervals.

The wash liquid flow rate supplied to a single filter was constant for a specific case, but ranged from 0.5 L/min to 1.5 L/min between cases. The average dry matter mass flow rate measured for each case ranged from 83 kg/hr to 95 kg/hr. The liquid absorption coefficient for the poplar fibres was determined by iterating its value for the specific wash liquid/average dry matter flow rate combination associated with a particular case. This was carried out until the prediction from TSESimFibre matched the measured, filtrate flow rate recorded by Greenfield for the same case. The procedure was repeated for all eight cases and from the results of those simulations, an average liquid absorption coefficient of 3.2x10^{-5} kg/m^{2}·s$^{1/2}$ was determined. After determining this average liquid absorption coefficient, the value was used to predict filtrate flow rate for each of the eight cases in conjunction with their associated wash liquid/average dry matter flow rates. The results were later compared to those obtained from the Greenfield trial data, and the assessment is summarized in Table 9 below. Additionally, the simulation profiles for the best performing case (case 7) are shown in Figure 49 below.

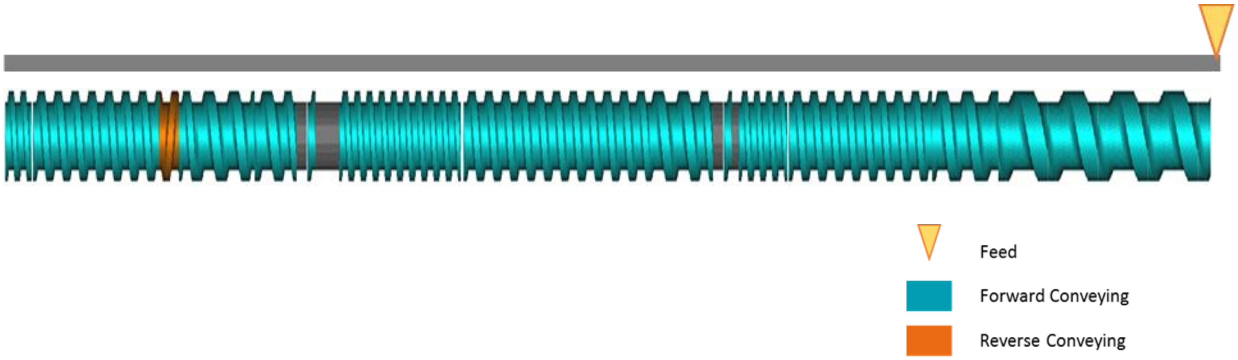

Figure 47: Greenfield's screw configuration 21

The last column of Table 9 shows the percent difference (absolute) between the filtrate flow rates recorded during Greenfield's trials, and those predicted by TSESimFibre. Percentages were calculated with respect to the measured filtrate flow rate values. The percent difference for most cases generally fell within the 0% to 30% range, excepting that of the first and last cases. Further examination of this data with a box plot revealed that neither the case one nor case eight percent differences were extreme enough to be considered outliers. Consequently, no case data was eliminated, and the average liquid absorption coefficient was accepted as 3.2x10^{-5} kg/m^{2}·s$^{1/2}$. When compared to values obtained for other hardwoods (see Section 2.2.1.2), the average fitted value for liquid absorption coefficient was an order of magnitude smaller. The value was still considered valid since the liquid absorption coefficient has been shown to vary by orders of magnitude within hardwood and softwood species, and since much smaller values for liquid absorption coefficients have been recorded in the literature.

Table 9: Comparisons between measured and predicted net filtrate flow rates for Greenfield's screw configuration 21

Case	Wash Liquid Flow Rate (Total), L/min	Net Filtrate Flow Rate (Measured), L/min	Net Filtrate Flow Rate (Predicted), L/min	Percent Difference (Absolute), %
1	2.00	1.13	0.71	37.8
2	2.00	0.77	0.62	19.2
3	2.50	0.97	1.11	14.9
4	2.00	0.78	0.63	19.0
5	2.75	1.14	1.36	19.5
6	2.50	0.92	1.11	20.9
7	2.75	1.20	1.10	8.3
8	2.75	1.04	1.37	32.1
			Average	21.5

4.2.3.4. Stage 2b: Validation with Screw Configuration 18

To further evaluate the quality of the average liquid absorption coefficient obtained from the previous subsection, the value was used to predict the net filtrate flow rates of various screw configuration 18 cases. Screw configuration 18 is shown schematically in Figure 48, and the results from its trials and simulations are summarized in Table 10. As done previously, the simulation results for the best performing case (case 2) are shown in Figure 50 below. From Table 10, it could clearly be seen that the predictions for screw configuration 18 were slightly poorer than those of screw configuration 21. The average absolute percent difference for the screw configuration 18 cases was 26.7%, which was about 20% higher than the average value recorded for screw configuration 21.

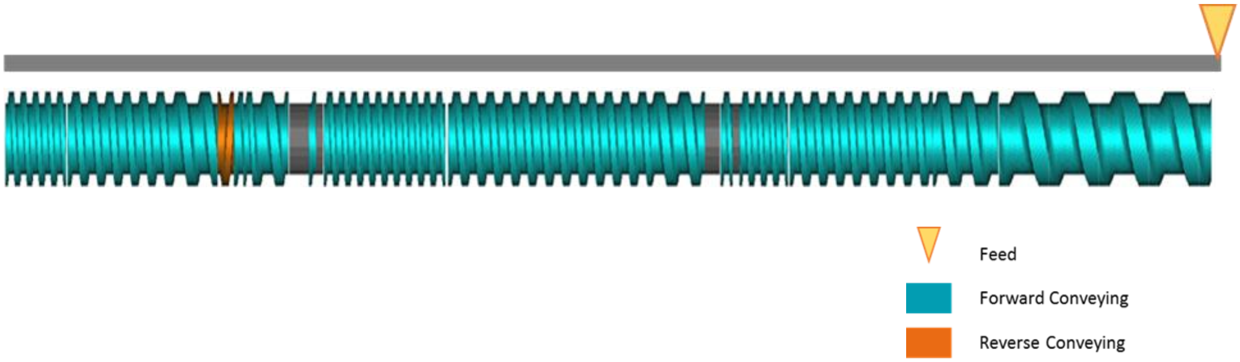

Figure 48: Greenfield's screw configuration 18

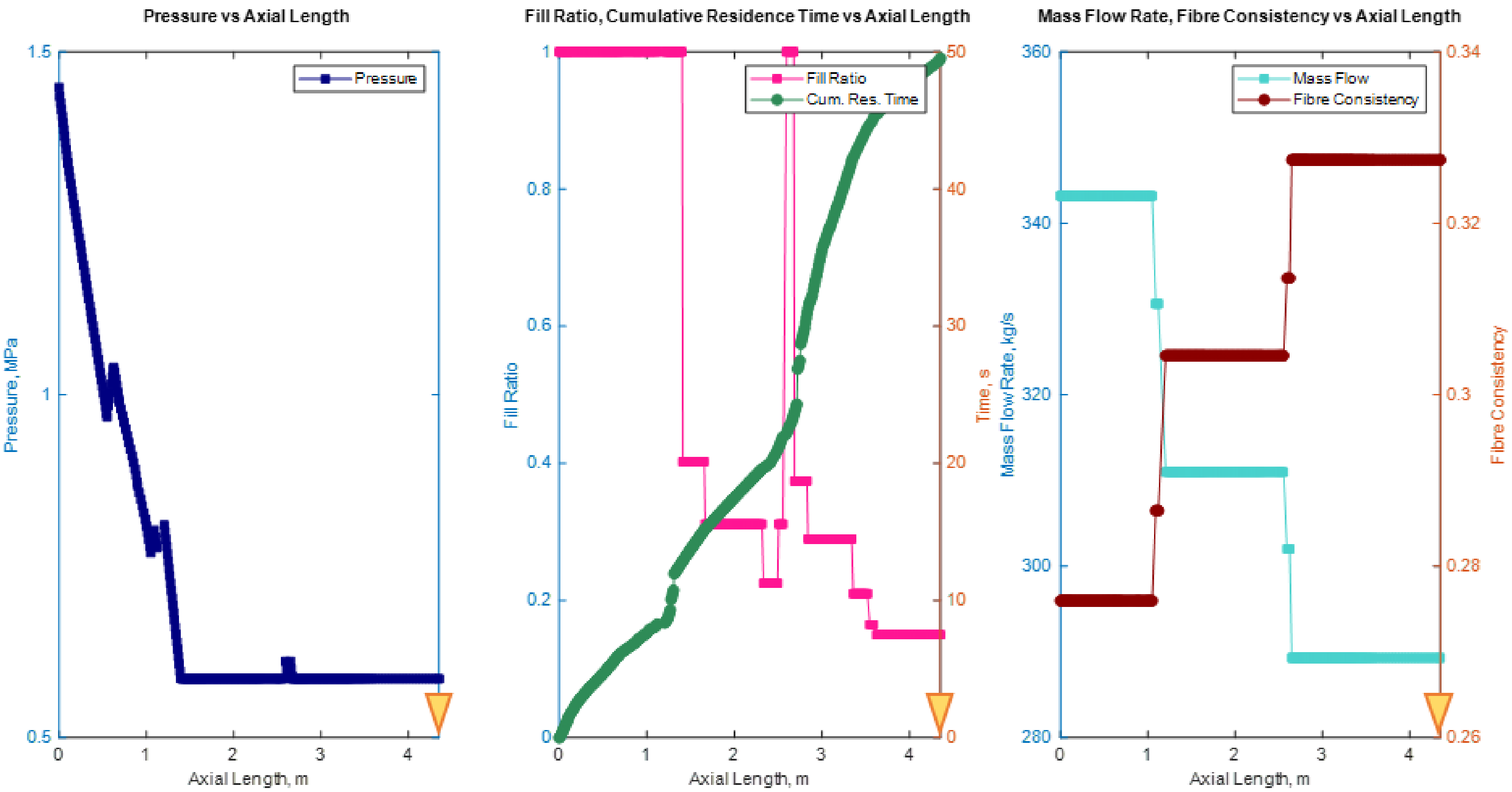

Figure 49: Simulation results for screw configuration 21, case 7

Table 10: Comparisons between measured and predicted net filtrate flow rates for Greenfield's screw configuration 18

Case	Wash Liquid Flow Rate (Total), L/min	Net Filtrate Flow Rate (Measured), L/min	Net Filtrate Flow Rate (Predicted), L/min	Percent Difference (Absolute), %
1	2.00	1.10	0.75	31.6
2	2.00	0.85	0.73	15.0
3	2.00	1.01	0.74	26.2
4	2.50	0.88	1.18	33.9
			Average	26.7

The poorer predictions with respect to the screw configuration 18 simulations can be attributed to numerous factors, including variations in material quality, process control challenges, and human error. With respect to material quality, it should be pointed out that the poplar fibres processed during screw configuration 21 trials (labelled PO#72) were not the same fibres processed during the screw configuration 18 trials (labelled PO#70 and PO#71). Although not explicitly stated, this implies that the fibres processed by the two screw configurations could have been ordered in different batches. If the poplar fibres processed by the two screw profiles belonged to different batches, it is possible that the woods may have been obtained from forest regions with very different soil properties, a factor known to affect the properties of wood (Karth 1967). It is also possible that the two wood batches were felled at different ages and during different seasons, which could have affected the dominant 'type of wood' of each batch (i.e. earlywood vs. latewood; heartwood vs. sapwood), as discussed in Section 2.2.1.1.

Differences in TSESimFibre's performance between the two screw configurations may also be due to unavoidable and unforeseen process control challenges. A major process control challenge faced during 'flowing' particulate transport is the maintenance of a constant flow rate in the system, particularly in funnel shaped reactors and silos. Such devices are susceptible to events such as bridging and ratholing which affect material transport. These challenges were likely faced by Greenfield due to the incorporation of those units in their biomass pre-treatment system, which made it difficult to maintain steady state conditions throughout. Another process control challenge is clogging of the extruder filtering sections from particulate accumulation in the filter. This build up changes the overall 'permeability' of the filter which increases flow resistance, and ultimately leads to lower filtrate flow rates. In addition to process control limitations, it should be pointed out that the trial data might not be free of common data entry errors which occur during the recording and transfer of data.

With respect to Greenfield's extruding system, the presence of any of the aforementioned factors in one trial (and its absence in the other) would affect the quality of the parameter fitting and simulation predictions performed. To determine a more representative value for liquid absorption coefficient, dedicated experiments should be planned and carried out for all possible poplar wood variants. Given the limitations of the project however, the absolute percent difference of 26.7% for the screw configuration 18 data was thought acceptable, and the liquid absorption coefficient of the poplar fibres was accepted to be 3.2×10^{-5} $kg/m^2 \cdot s^{1/2}$.

4.2.4. Parametric Study

The 'Design of Experiments' (DOE) and 'Change One Single variable at a Time' (COST) techniques were employed to investigate the effect of key operational parameters and extruder screw design on the extraction flow rate and liquid absorption properties of Greenfield's extrusion system. These parameters were selected due to Greenfield's need to maximize the amount of filtrate they received from the filters for further processing. The dry fibre mass flow rate and wash liquid mass flow rate were identified to be the most influential operation parameters, whilst spacer length and the axial location of neighbouring reverse screw elements were thought the most influential screw design parameters. For all investigations, the responding variables were the total liquid extraction rates from the filters, and the swollen density of the fibres exiting the extruder.

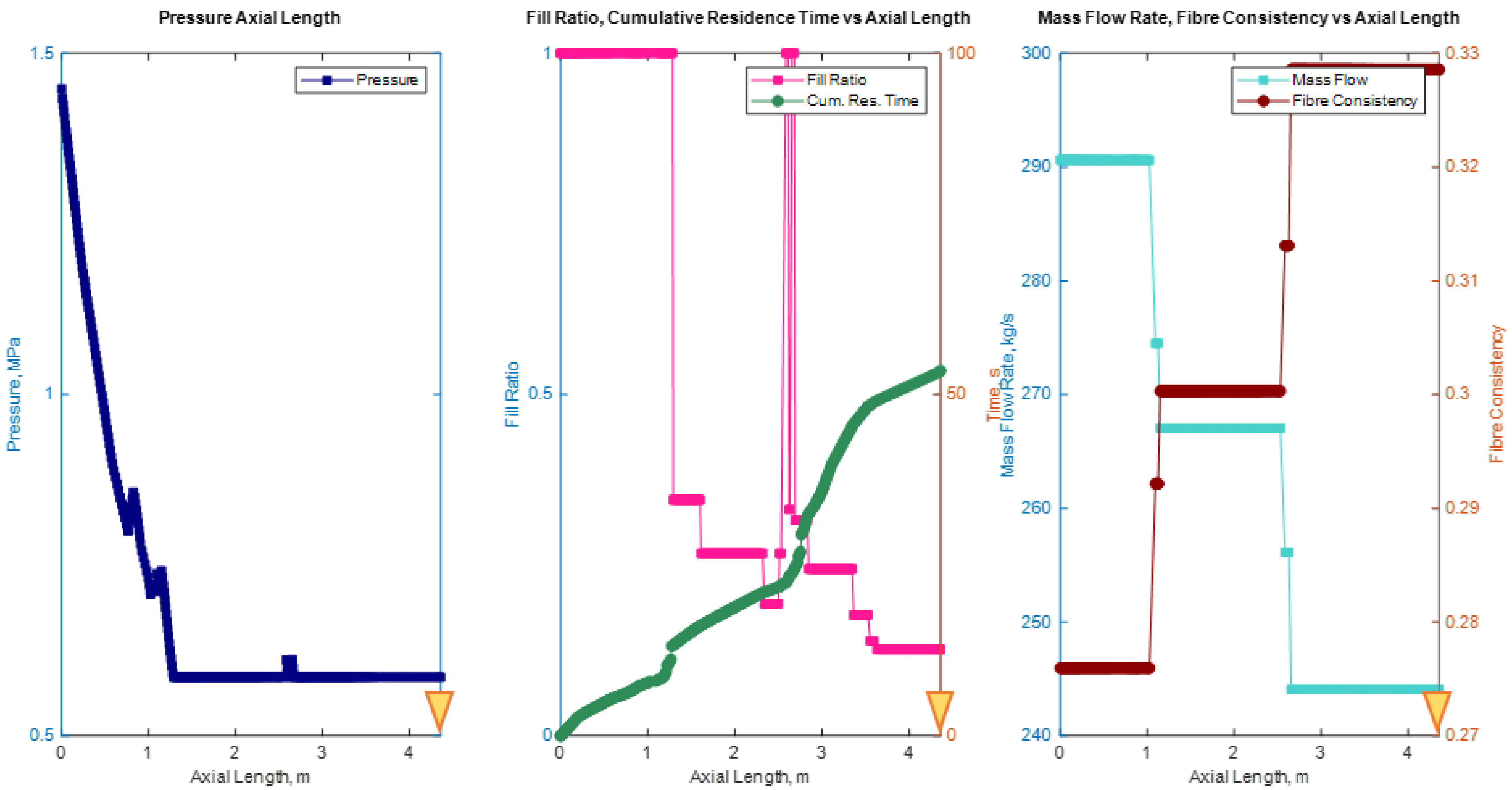

Figure 50: Simulation results for screw configuration 18, case 2

4.2.4.1. Effect of Operational Parameters

The effect of dry fibre mass flow rate and wash liquid mass flow rate on total liquid extraction flow rate and the exit swollen fibre density were investigated according to the experimental design outlined in Table 11. The design was a two-level, two-factor full factorial design with one additional simulation carried out at the centre point. The centre point values corresponded to the average or most frequently used operating conditions for Greenfield's extrusion system based on screw configuration 21. For this screw configuration, the average dry fibre mass flow rate was 91.5 kg/s, while the most frequently utilized wash liquid flow rate was 1.00 L/min per filtering section (or 0.50 L/min per spacers screw element). The high and low levels for dry fibre mass flow rate were +/- 5% (i.e. 86.9 kg/s and 96.0 kg/s respectively), while the high and low levels assessed for the wash liquid flow rate were +/- 25% (i.e. 0.75 L/min and 1.25 L/min respectively). The simulations were carried out using screw configuration 21 shown in Figure 47.

Table 11: Experimental design for net liquid extraction rate and exit swollen fibre density investigations

Standard Order	Dry Mass Flow Rate (A)	Wash Liquid Vol. Flow Rate (B)	Net Liquid Extraction Vol. Rate, L/min	Exit Swollen Fibre Density, kg/m^3
0	91.5 (0)	1.00 (0)	1.12	730.0
1	86.9 (-)	0.75 (-)	0.63	734.8
2	96.0 (+)	0.75 (-)	0.61	725.7
3	86.9 (-)	1.25 (+)	1.63	734.8
4	96.0 (+)	1.25 (+)	1.61	725.7

Liquid absorption coefficient: 3.2×10^{-5} kg/m$^{2}\cdot$s$^{1/2}$
Dry fibre density (based on swollen fibre volume): 201.5 kg/m^3
Exit Pressure: 1.45 MPa
Inlet Pressure: 0.59 MPa
Screw speed: 315 s^{-}

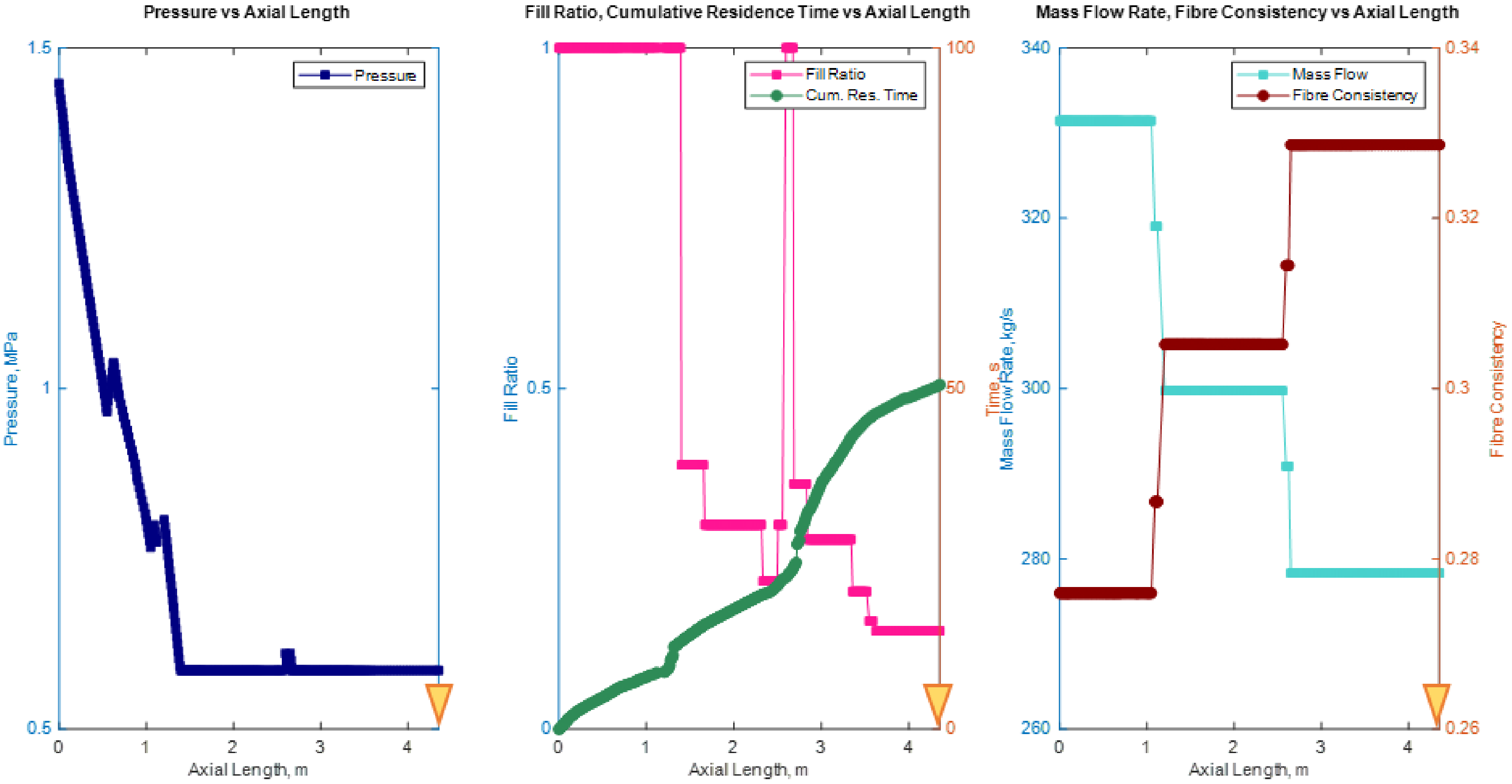

Figure 51: Centre point simulations for screw configuration 21

All other parameters, such as the material properties of the fibres, the design and operating conditions of the extruder and the simulator control conditions, were kept constant for all simulations. However, the method used to maintain certain parameters, the inlet consistency in particular, required more than a simple numerical specification. The inlet consistency of the fibrous suspension entering the extruder (0.33) was obtained from simulations ran at the centre point test conditions using an exit swollen fibre density of 730.0 kg/m^3. Although this value was kept constant for all simulations, the value for inlet consistency had to be iterated by manipulating the value of swollen fibre density due to the back-calculating design of TSESimFibre.

Table 11 also summarizes the results of the net liquid extraction rates and exit swollen fibre densities that were obtained from the DOE simulations. However, further insight into those results will be found in the succeeding subsections. Additionally, the simulation results for the steady state case (the center point values) are shown in Figure 51.

4.2.4.1.1. Liquid Extraction Rate

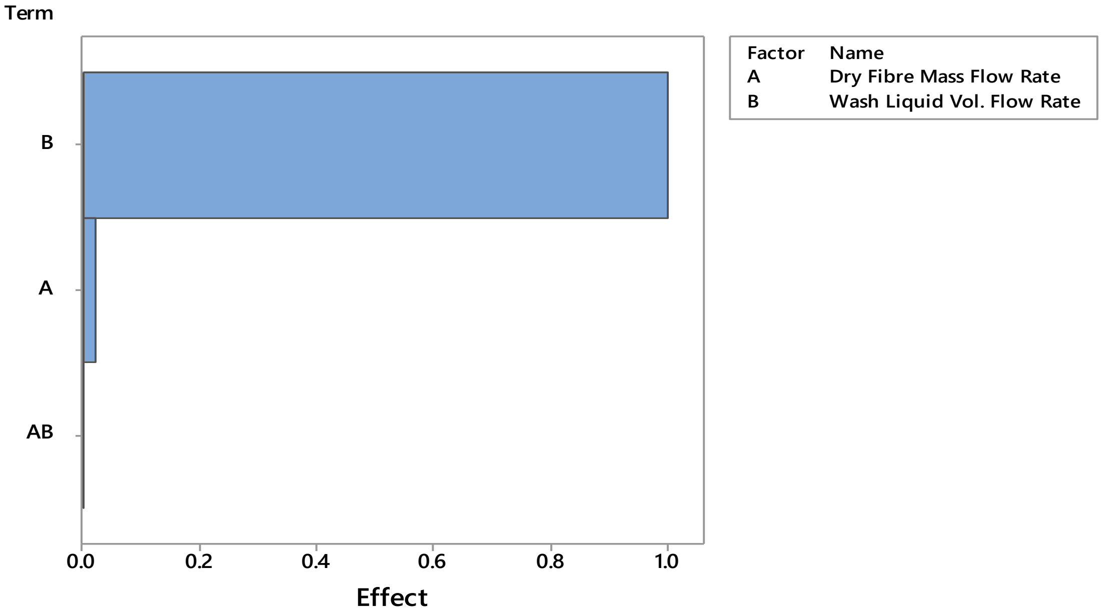

Figure 52: Pareto plot for net liquid extraction rate

Equation 101: Factorial Regression for Net Liquid Extraction Rate

$$Q_{filtrate} = 1.115 - 0.01\,\dot{m}_{f,dry} + 0.50\,Q_{wash\ liquid}$$

The factorial regression equation detailing the dependence of net liquid extraction flow rate on dry fibre mass flow rate and wash liquid volumetric flow rate is shown in Equation 101. From this equation and the Pareto Plot in Figure 52, it could be seen that the wash liquid flow rate had a significantly greater effect on the net liquid flow obtained from the filters. In fact, the dry fibre flow rate had a very small effect on the overall liquid flow rate from the filters, and its interaction with wash liquid flow rate was negligible. Consequently, net liquid extraction rate can be thought to depend only on the rate at which wash liquid is supplied. Equation 101 also indicates that a positive correlation exists between the filtrate and wash liquid flow rates, which means that increases to the amount of wash liquid will increase the total amount of filtrate collected. This result is consistent with what is expected due to the principle of conservation of mass, and due to the fact that all other flow altering factors were kept constant during the simulation.

4.2.4.1.2. Exit Swollen Fibre Density

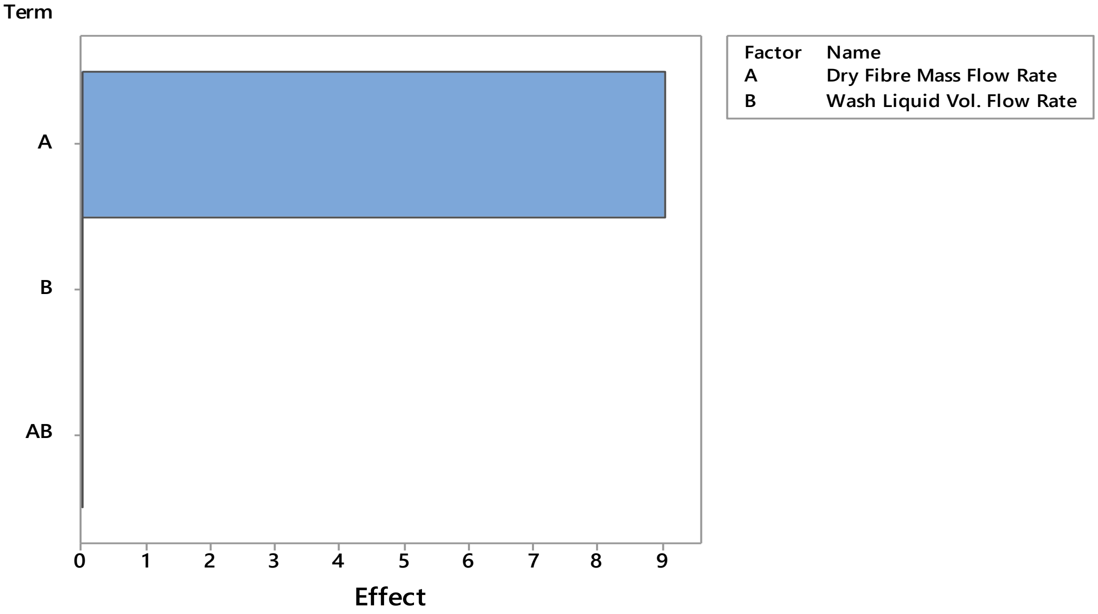

Figure 53: Pareto plot for Exit Swollen Fibre Density

Equation 102: Factorial Regression for Exit Swollen Fibre Density

$$\rho_{sf} = 730.20 - 4.53\, \dot{m}_{f,dry}$$

The factorial regression equation detailing the dependence of the exit swollen fibre density on dry fibre mass flow rate and wash liquid volumetric flow rate is shown in Equation 102. From this equation and the Pareto Plot in Figure 53, it could be seen that the dry fibre flow rate was the only factor affecting the density of the swollen fibres leaving the extruder. Both the wash liquid flow rate and its associated interaction term had no effect on the final density of the exiting fibres and consequently, those two terms were dropped from the regression equation. Equation 102 also indicates that a negative correlation exists between the exit swollen fibre density and dry fibre mass flow rate, which means that swollen fibres with larger densities leave the extruder when the dry fibre mass flow rate is lower. This result is plausible since the density of the swollen fibres is directly related to the amount of liquid it is able to absorb. Lower mass flow rates allow the fibres to spend longer times in the aqueous filter environment, which allows them to absorb larger amounts of liquid that increase their final densities.

4.2.4.2. Effect of Screw Configuration

The effect of two unique screw configuration parameters on net liquid extraction flow rate and exit swollen fibre density was determined for the second variant of Greenfield's screw configuration 21. In this variant, only the most downstream, 40 mm length filtering section is retained, as can be seen in Figure 54. All other filtering screw elements were changed to conveying screw elements to ensure analysis simplicity, and to maintain a constant screw profile length for all simulations. The two design parameters explored were the axial location of the reverse screw element from the filter, and the length of the spacers forming the filter. In Greenfield's screw configuration 21, the reverse screw element is located 425 mm away from the most downstream filtering unit. For all simulations, liquid was injected at a flow rate of 1.00 L/min and the liquid absorption coefficient of the fibres was $3.2\text{x}10^{-5}$ kg/m^2·s$^{1/2}$. The dry fibre mass flow rate was 91.5 kg/s, which was the average dry fibre mass flow rate recorded by Greenfield during their trials with screw configuration 21. The initial consistency of the fibres entering the extruder was 0.29, and it was again kept constant for each investigated scenario by iterating the exit swollen fibre density. The simulation results for the specifications outlined above are shown in Figure 55.

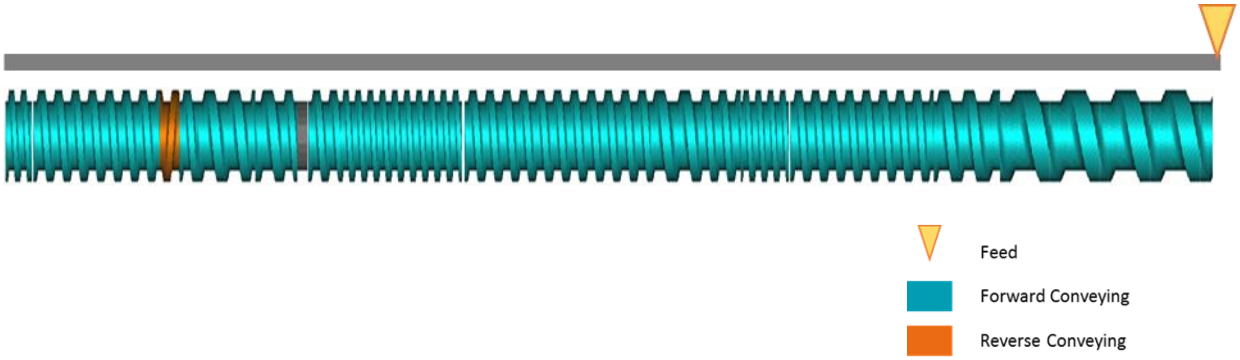

Figure 54: Second variant of Greenfield's screw configuration 21

4.2.4.2.1. Reverse Screw Element from Location from Spacer

From Figure 56, it could be seen that the general proximity of the reverse screw element to the filter had no significant effect on the liquid extraction rate of the filtrate, or the exit swollen fibre density. This result is plausible since the residence time of the fibres in the filter is unaffected by its neighbouring screw elements for extruders operating at steady state, and because residence time is the major factor affecting liquid absorption (and for this case, filtrate flow rate) in systems containing identical fibres. It should be pointed out that the location of the reverse screw element has some effect on the pressure profile near the filter, which in turn affects the effective mass flow rate of water expressed during consolidation. However, the contributions of the effective expressed mass flow rate are small due to the small time afforded for consolidation, making the effect of pressure, and consequently reverse screw element location, negligible. Therefore, if the aim is to maximize liquid extraction from an extruder, there is little need to complicate the screw profile with reverse screw elements as they have no effect on the liquid extraction capabilities of the system. Unfortunately, it was impossible to identify this occurrence in Greenfield's trial data since the location of the reverse screw element, the length of the spacer and the general screw configuration varied with each trial.

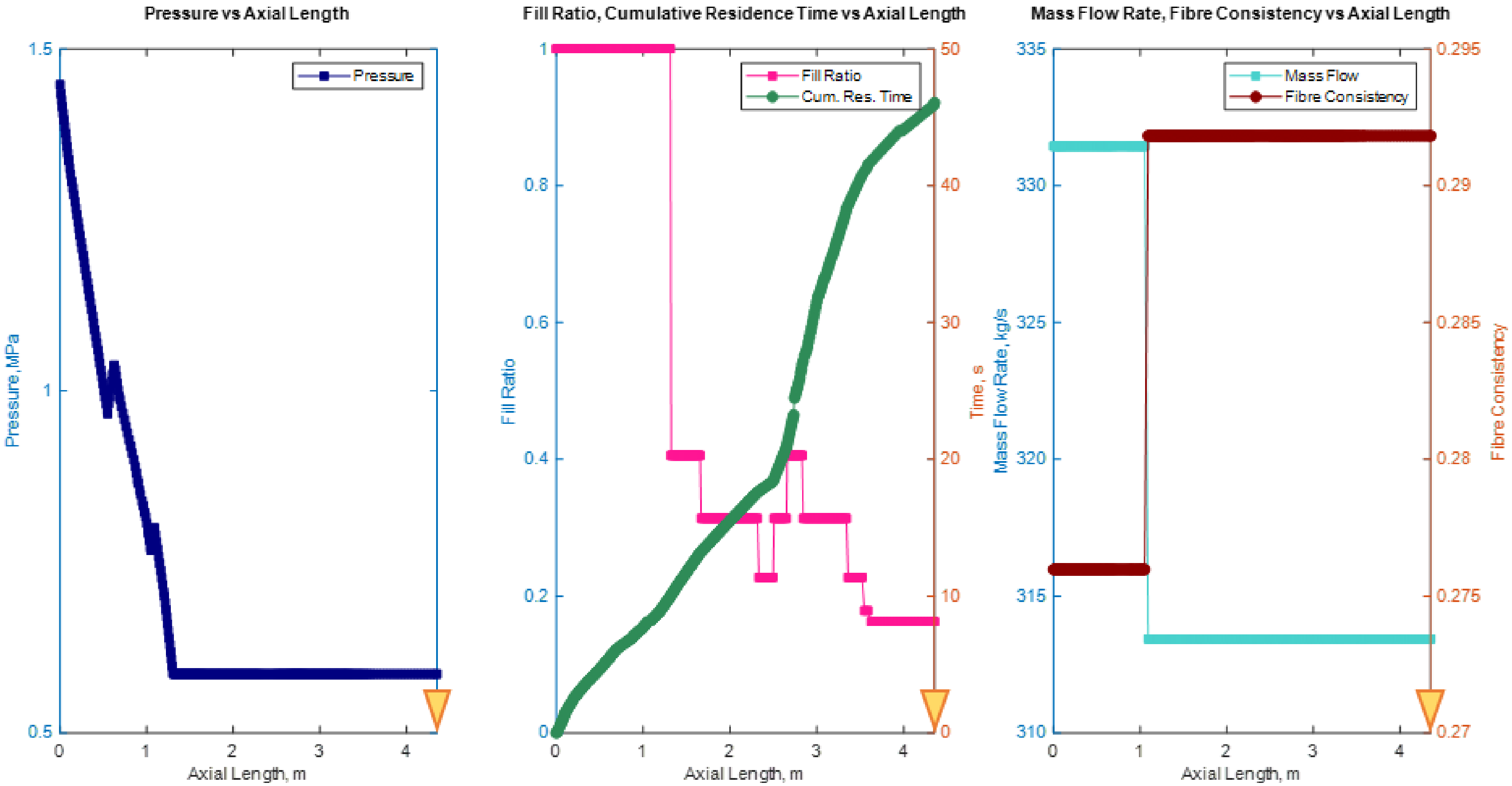

Figure 55: Simulation results for screw configuration 21, second variant

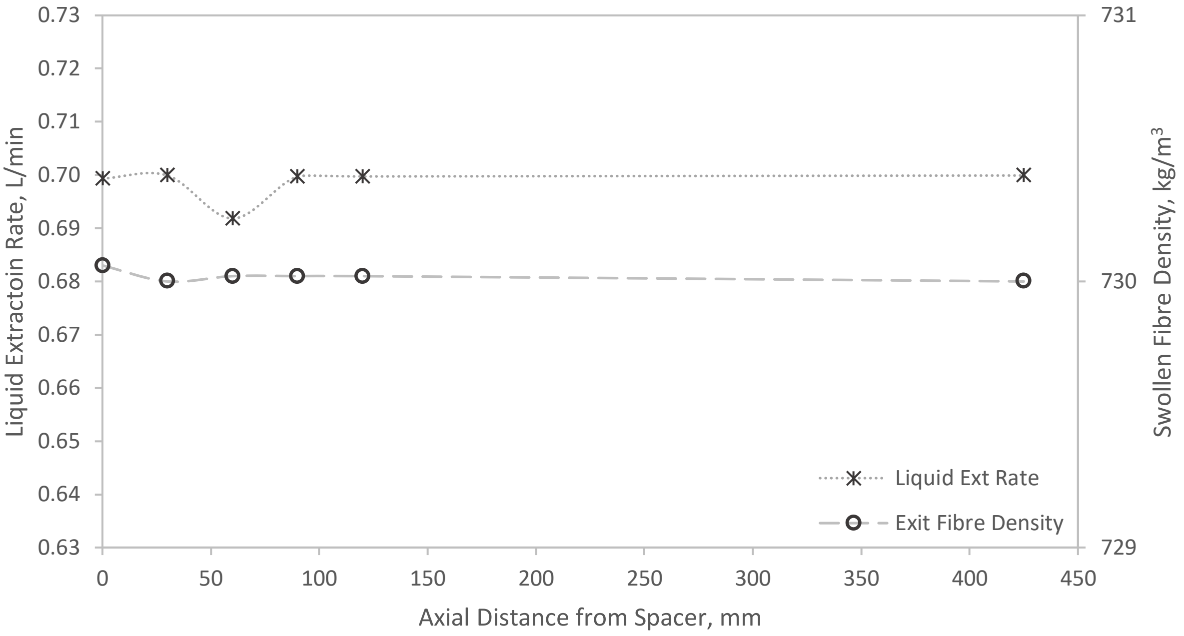

Figure 56: Effect of reverse screw element/filter proximity on net liquid extraction flow rate and swollen fibre density

4.2.4.2.1. Filter Length

Figure 57 summarizes the effect of filter length on net liquid extraction flow rate and swollen fibre density. From this figure, it could be seen that the longer the filter, the smaller the amount of liquid collected, and the larger the swollen fibre density of the exiting fibres. This behaviour is attributable to the residence time increases associated with an increase in volume. If the volume of the filter is increased without any changes to the fibre mass flow rate, the fibres spend more time in the filter, allowing them to absorb more wash water. This increases the final density of the fibres, and reduces the amount of liquid collected from the filters. Again, it was impossible to identify this occurrence in Greenfield's trial data due to the complicated geometry of their filters, and inconsistencies in the method used to carry out their trials.

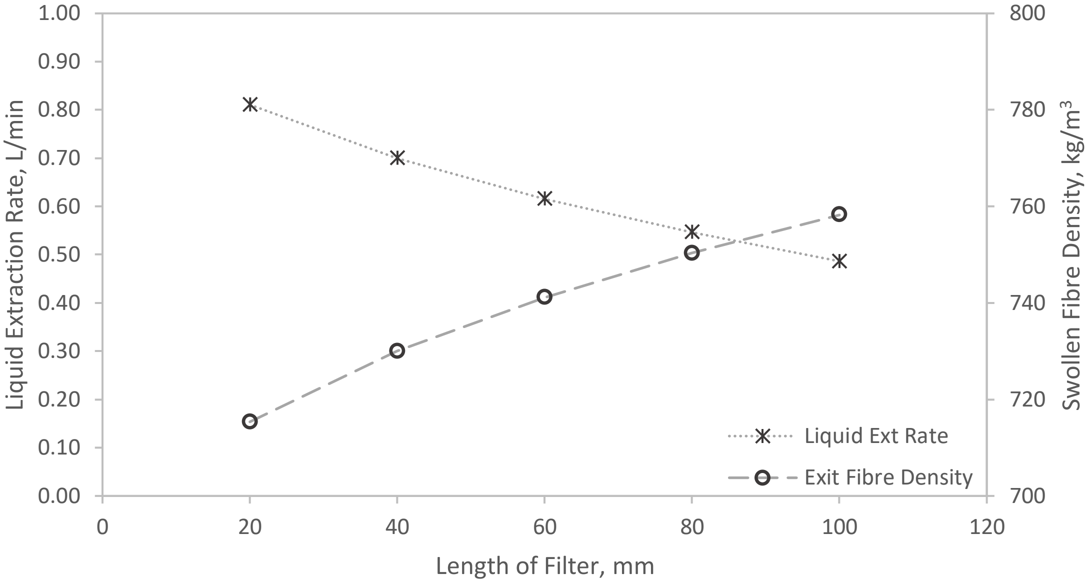

Figure 57: Effect of filter length on net Liquid extraction flow rate and swollen fibre density

5. Conclusions

Experimental

The material properties of two differently processed poplar fibres were investigated using a series of established chromatography and microscopy techniques, and standard practices in geotechnical engineering. These procedures were selected in order to gain an in-depth knowledge of the physical, chemical and material properties of the fibres that were entering and leaving Extruder 2 from Greenfield's biomass pre-treatment system. Such characterisations yielded numerous correlations and constants useful to the development of the novel global extruder model for suspension processing. The major conclusions from these experiments are presented below:

1. The extent of extrusion (from multiple extrusion stages) had very little effect on the chemical properties of the poplar wood fibres. However, the process had a significant effect on length distribution and average fibre length. This finding is expected since extrusion is primarily a physical process.

2. The permeability of the poplar wood fibres was affected by the fibre length distribution and consequently, its average fibre length. This is expected since the permeability of a material is highly sensitive to its porosity, which is in turn sensitive to particulate shape and size in granular systems. Systems of smaller particulates experience tighter packing which in-turn lowers their porosity and permeability.

3. The compressibility and friction properties of the poplar wood fibres were not affected by water content or fibre length distribution. The observation is justified since experimentation was carried out under drained conditions, and because both properties are inherent to the material composing the fibres.

4. Wood fibre suspensions are mechanically similar to fibrous peats. This permits direct use of geotechnical engineering techniques for characterisation, particularly in the areas of consolidation and friction. This finding is expected since the two fibres are mostly composed of xylem material from tree stems. The observation promises to be extremely

useful for many different wood fibre processing applications by providing a slew of alternative measurement and modelling techniques.

Numerical

A novel global simulator was developed for predicting the performance of suspension-processing twin screw extruders. The model was based on the plasticating extruder algorithm proposed by Vergnes et al. (1998), and underwent several alterations before being suitable for suspension-processing applications. The first alteration performed was replacement of the Power Law model with the Herschel-Bulkley model to account for the differing rheologies between fibrous suspensions and polymer melts. The second alteration was the incorporation of Terzaghi's 1D Consolidation equation to describe the consolidating behaviour of the suspension in the flightless screw elements. The novel model was coded in MATLAB, and the validation procedures yielded an average, absolute percent difference of 26.7% for the net liquid extraction flow rates between Greenfield's trial data and the simulator's predictions. Given the project limitations and the novelty of this work, this difference was deemed acceptable, and a parametric study was carried out to assess the effects of various design and operation parameters on the performance of the extruder. The effect of two different operating parameters (wash liquid flow rate and dry fibre density) and two different screw configuration features (reverse screw element location and filtering spacer length) on the exit swollen fibre density and net filtrate flow rate were investigated, and the major conclusions from which are presented below:

5. Regarding operating conditions, the net liquid extraction rates leaving the filtering spacers screw elements was positively correlated to the mass flow rate of wash liquid injected at the site. These observations are easily justified by the principle of conservation of mass.

6. Regarding operating conditions, the swollen fibre density of the exiting fibres was negatively correlated to the rate at which fibres are fed to the extruder (dry basis). This prediction is plausible since increases to dry fibre mass flow rate reduces the residence time of the fibres in the filter which in turn, reduces the amount of liquid absorbed.

7. The location of the reverse screw element with respect to the filtering spacers had a negligible effect on the net liquid extraction and final swollen fibre density predictions.

This seems reasonable since extraction rates are mainly influenced by the wash liquid flow rates to the filter, which is unaffected by the specific screw configuration utilized. Additionally, the location of reverse screw elements mostly influenced the expressed liquid flow rate from consolidation in the filter (by altering the axial pressure profile), which made up a very small fraction of the net liquid extraction rate.

8. The length of the filtering spacers had a significant effect on both the net liquid extraction rates and densities of the swollen fibres leaving the extruder. This seems reasonable since a larger filtering region has a larger residence time, and facilitates more opportunities for absorption. Consequently, a reduction in net liquid extraction and an increase in swollen fibre density ensues.

6. Recommendations

1. Development of a method to measure the absorption coefficient of wood fibres. The method employed in the text relied on force-fitting the simulation to a trial data set to elucidate the necessary coefficient. The accuracy of this procedure is reliant on the accuracy of the dataset used, and may not provide the most precise estimations due to embedded process errors, variance from operations, and data recording uncertainties.

2. Acknowledgement of temperature dependence in the model and simulator. The effect of temperature on the model predictions was neglected due to a lack of applicable literature resources, and the inability to perform measurements due to equipment unavailability. However, the effect of temperature on a fibrous suspension is expected to be significant, and is also expected to strongly affect the suspension consistency and its rheological properties.

3. Acknowledgement of the effects of surface tension in the model and simulator, which were ignored to facilitate easier modelling. While the assumption is acceptable for low and medium consistency pulps, it becomes more unsuitable as the consistency of the suspension increases since undissolved gas bubbles become more frequent. The presence of those bubbles helps provide mechanical strength to the flocs they are found within due to the surface tension forces acting at their gas/liquid interfaces. These forces can significantly alter the flow and consolidation behaviour of the suspension and consequently, the quality of the simulator’s predictions.

4. Acknowledgement of expression in the conveying sections of the extruder. Although expression is assumed to occur in the filtering sections only, there is the potential for the fibres to be subjected to great pressures during conveyance (i.e. at reverse screw elements) which could also lead to expression. This could result in the development of significant liquid backflow streams which might affect the accuracy of consistency and flow calculations at various points along the extruder screw profile.

References

Barrès C, Vergnes B, Tayeb J (1991). An Improved Thermal Model for the Solid Conveying Section of a Twin-Screw Extrusion Cooker. Journal of Food Engineering 15(3), 167–185

Bell FG (2013). Foundation Engineering in Difficult Ground, Revised. Elsevier, Chatham

Bird RB, Stewart WE, Lightfoot EN (2001). Transport Phenomena, Second Ed. Wiley

Booy ML (1978). Geometry of Fully Wiped Twin-Screw Equipment. Polymer Engineering & Science 18(12), 973–984

Bouvier JM, Campanella OH (2014). Extrusion Processing Technology: Food and Non-Food Biomaterials. John Wiley & Sons.

Broyer E (1975). A Theoretical Model for the Cavity Filling Process in Injection Molding. Journal of Rheology 19(3), 423

Broyer E, Gutfinger C, Tadmor Z (1975). Evaluating Flows of non—Newtonian Fluids by the Method of Equivalent Newtonian Viscosity. 21(1), 198–200

Campbell N, Reece J (2005). Biology, Seventh. Pearson (Benjamin Cummings), United States

Candanedo L, Derome D (2005). Numerical Simulation of Water Absorption in Softwood. In: Proceedings of the 9th International IBPSA Conference. pp 123–130

Canedo E (1999). Computer Simulation of Plastics Compounding Operations in Twin-Screw Extruders. Society of Petroleum Engineers Technical Conference 45310–316

Coduto DP (1999). Geotechnical Engineering: Principles and Practices, 1st ed. Prentice-Hall, Upper Saddle River, NJ

Dantzig JA, Tucker CL (2001). Modeling in Materials Processing. Cambridge University Press

Daoxing Y, Hong L (2016). Fluidization Characteristics of Medium-High-Consistency Pulp Fiber Suspensions with an Impeller. Int J Rotating Mach

Das BM (2009). Principles of Geotechnical Engineering, 7th ed. Cengage Learning, Stamford, CT

Derakhshandeh B, Kerekes RJ, Hatzikiriakos SG, Bennington CPJ (2011). Rheology of Pulp Fibre

Suspensions: A Critical Review. Chemical Engineering Science 66(15), 3460–3470

Duffy GG (2006). Measurements , Mechanisms and Models: Some Important Insights into the Mechanisms of Flow of Fibre Suspensions. Annual Transactions of the Nordic Rheology Society 14(0), 19

Ellis B, Smith R (2008). Polymers: A Property Database, Second Edi. CRC Press

Elsey JR (2002). Dynamic Modelling, Measurement and Control of Co-Rotating Twin-Screw Extruders. University of Sydney, Australia

Farid MM (2010). Mathematical Modeling of Food Processing. CRC Press

Fredlund D, Rahardjo H (1993). Soil Mechanics for Unsaturated Soils. John Wiley & Sons, USA

Gallos A, Paës G, Allais F, Beaugrand J (2017). Lignocellulosic Fibers: A Critical Review of the Extrusion Process for Enhancement of the Properties of Natural Fiber Composites. RSC Advances 7(55), 34638–34654

Germaine A V., Germaine JT (2009). Geotechnical Laboratory Measurements for Engineers. John Wiley & Sons, Hoboken, NJ

Giles HJ, Mount EI, Wagner JJ (2004). Extrusion: The Definitive Processing Guide and Handbook. William Andrew Inc., USA

Guy R (2001). Extrusion Cooking: Technologies and Applications. Elsevier

Heldman DR, Lund DB, Sabliov C (2006). Handbook of Food Engineering, 2nd edn. CRC Press

Higuchi T (2012). Biochemistry and Molecular Biology of Wood. Springer, Berlin

Huat BBK, Prasad A, Asadi A, Kazemian S (2014). Geotechnics of Organic Soils and Peat. CRC Press, Leiden

Isikgor FH, Becer CR (2015). Lignocellulosic Biomass: A Sustainable Platform for the Production of Bio-Based Chemicals and Polymers. Polymer Chemistry 6(25), 4497–4559

Jiang Q (2008). Modelling Flow, Melting, Solids Conveying and Global Behavior in Intermeshing, Counter Rotating Twin Screw Extruders. the University of Akron

Karth S (1967). Factors Affecting Wood Quality And Quantity Aan Consequently Pulp Manufacture.

South African Forestry Journal 61(1), 17–24

Kazemian S, Huat BBK, Prasad A, Barghchi M (2011). A State of Art Review of Peat: Geotechnical Engineering Perspective. International Journal of Physical Sciences 6(8), 1974–1981

Kazi SN, Duffy GG, Chen XD (2015). Kazi, S. N., G. G. Duffy, and X. D. Chen. "Heat Transfer Coefficient of Flowing Wood Pulp Fibre Suspensions to Monitor Fibre and Paper Quality. Applied Thermal Engineering 78(0), 172–184

Kerekes R (2017). Power Requirements for Pulp Suspension Fluidization.

Kerekes RJ, Soszynski RM, Doo PAT (1985). The Flocculation of Pulp Fibres. In: Proceedings of the 8th Fundamental Research Symposium, Mechanical Engi- neering Publications, Oxford, England. pp 265–310

Kohlgrüber K (2008). Co-Rotating Twin-Screw Extruders: Fundamentals, Technology, and Applications. Hanser

Kolleman FFP, Cote WA (1986). Principles of Wood Science and Technology, Vol. I. Solid Wood. Springer-Verlag, New York

Kretschmer K, Bastian M, Potente H, Thümen A (2005). Computer Aided Simulation of Co-Rotating Twin Screw Extruders. KGK Kautschuk Gummi Kunststoffe 58(5), 246–251

Lafleur PG (2014). Polymer Extrusion. John Wiley & Sons

Landva AO, Pheeney PE (1980). Peat Fabric and Structure. Canadian Geotechnical Journal 17(3), 416–435

Lea ND, Brawner CO (1963). Highway Design and Construction over Peat Deposits in Lower British Columbia. Highway Research Record (7), 1–32

Leong-poi L, Allen D (1992). Direct Measurement of the Yield Stress of Filamentous Fermentation Broths with the Rotating Vane Technique. Biotechnology and bioengineering 40(3), 403–412

Lepage RTM (2012). Moisture Response of Wall Assemblies of Cross- Laminated Timber Construction in Cold Canadian Climates. University of Waterloo

Lin Y, Tanaka S (2006). Ethanol Fermentation from Biomass Resources: Current State and Prospects. Applied Microbiology and Biotechnology 69(6), 627–642

Lovegrove J, Williams J (1973). Solids Conveying in a Single Screw Extruder; a Comparison of Theory and Experiment. Journal of Mechanical Engineering Science 15(3), 195–199

MacLean JD (1941). Thermal Conductivity of Wood. Heating, piping & air conditioning 13(6), 380–391

Malherbe S, Cloete TE (2002). Lignocellulose Biodegradation: Fundamentals and Applications. Reviews in Environmental Science and Biotechnology 1(2), 105–114

Mesri G, Ajlouni M (2007). Engineering Properties of Fibrous Peats. Journal of Geotechnical and Geoenvironmental Engineering 133(7), 850–866

Noorolahi S, Khazaei J, Jafari S (2008). Modeling Cyclic Water Absorption and Desorption Characteristics of Three Varieties of Wood. In: World Conference on Agricultural Information and IT, Tokyo University of Agriculture

Okoh ET (2014). Water Absorption Properties of Some Tropical Timber Species. Journal of Energy and Natural Resources 3(2), 20–24

Orisaleye JI, Ojolo SJ (2018). Parametric Analysis and Design of Straight Screw Extruder for Solids Compaction. Journal of King Saud University - Engineering Sciences 31(1), 86–96

Osipov V (2015). Physicochemical Theory of Effective Stress in Soils. Springer International Publishing, Switzerland

Oswell JM (1991). Elastic Plastic Behaviour of a Sand-Bentonite Mixture. University of Manitoba

Potente H, Ansahl J, Klarholz B (1994). Design of Tightly Intermeshing Co-Rotating Twin Screw Extruders. International Polymer Processing 9(1), 11–25

Potente H, Ansahl J, Wittemeier R (1990). Throughput Characteristics of Tightly Intermeshing Co-Rotating Twin Screw Extruders. International Polymer Processing 5(3), 208–216

Potente H, Melisch U, Palluch K (1996). A Physico-Mathematical Model for Solids Conveying in Co-Rotating Twin Screw Extruders. International Polymer Processing 11(1), 29–41

Qazi SS, Li D, Briens C, et al (2017). Antioxidant Activity of the Lignins Derived from Fluidized-Bed Fast Pyrolysis. Molecules 22(3), 372

Radmanović K, Đukić I, Pervan S (2014). Specific Heat Capacity of Wood. DRVNA INDUSTRIJA 65(2), 151–157

Rahman MS (2009). Food Properties Handbook, 2nd edn. CRC Press

Rauwendaal C (2014). Polymer Extrusion, 5th edn. Carl Hanser Verlag GmbH & Company KG

Ross RJ (2010). Wood Handbook: Wood as an Engineering Material, Centennial. USDA Forest Service, Forest Products Laboratory, General Technical Report FPL-GTR-190, Madison, WI

Schniewind (editor) A (1989). Concise Encyclopedia of Wood and Wood-Based Materials, First. Elsevier Science

Shirato M, Hayashi N, Iwata M, et al (1985). Continuous Expression of Slurry in a Screw Press. International Chemical Engineering 25(1), 88–96

Shirato M, Murase T, Hayashi N, et al (1978). Fundamental Studies on Continuous Extrusion Using a Screw Press. International Chemical Engineering 18(4), 680–688

Shirato M, Murase T, Iwata M (1983). Pressure Profile in a Power-Law Fluid in Constant-Pitch, Straight-Taper and Decreasing-Pitch Screw Extruders. International Chemical Engineering 32(2), 323–331

Shirato M, Murase T, Iwata M, Nakatsuka S (1986). The Terzaghi-Voigt Combined Model for Constant-Pressure Consolidation of Filter Cakes and Homogeneous Semi-Solid Materials. Chemical Engineering Science 41(12), 3213–3218

Shirato M, Murase T, Iwata T (1982). Pressure Profiles in Constant-Pitch, Straight-Taper and Decreasing-Pitch Screw Extruders. International chemical engineering 22(3), 470–478

Skelland AHP (1958). Correlation of Scraped-Film Heat Transfer in the Votator. Chemical Engineering Science 7(3), 166–175

Stevens C (2010). Industrial Applications of Natural Fibres: Structure, Properties and Technical Applications (Volume 10 of Wiley Series in Renewable Resource). John Wiley & Sons, Wiltshire, Great Britain

Stevens M, Covas J (2012). Extruder Principles and Operation, Second. Springer Science & Business Media B.V, Netherlands

Stevens MJ (1985). Extruder Principles and Operation. Elsevier Applied Science Publishers

Strutt DB (1998). A Study of Reactive Flow of Polypropylene In Single and Twin Screw Extruders. University of Waterloo, Canada

Sumida M (2013). Flow Properties of Wood Pulp Suspensions in Pipes. World Academy of Science, Engineering and Technology, International Journal of Mechanical, Aerospace, Industrial, Mechatronic and Manufacturing Engineering 7(11), 2202–2206

Szydlowski W, White JL (1988). A Non-Newtonian Model of Flow in a Kneading Disc Region of a Modular Intermeshing Corotating Twin Screw Extruder. Journal of Non-Newtonian Fluid Mechanics 28(1), 29–46

Tadmor Z, Gogos C (2013). Principles of Polymer Processing. John Wiley & Sons, New Jersey

Tadmor Z, Klein I (1978). Engineering Principles of Plasticating Extrusion. Krieger

Tadmor Z, Klein I (1970). Engineering Principles of Plasticating Extrusion. Van Nostrand Reinhold Co.

Tang H, Wrobel L, Fan Z (2003). Fluid Flow Aspects of Twin Screw Extruder Process: Numerical Simulations of TSE Rheomixing. Modelling and Simulation in Materials Science and Engineering 11(5), 771

Tayeb J, Vergnes B, Della Valle G (1988). Theoretical Computation of the Isothermal Flow Through the Reverse Screw Element of a Twin Screw Extrusion Cooker. Journal of Food Science 53(2), 616–625

Terzaghi K (1943). Theoretical Soil Mechanics. Wiley, New York

Todd D (1988). Heat Transfer in Twin Screw Extruders. In: Society of Plastics Engineers 46th Annual Technical Conference & Exhibits, Atlanta, USA. pp 54–58

Venter MJ, Kuipers NJM, De Haan AB (2007). Modelling and Experimental Evaluation of High-Pressure Expression of Cocoa Nibs. Journal of Food Engineering 80(4), 1157–1170

Ventura C, Blanco A, Negro C, et al (2007). Modeling Pulp Fiber Suspension Rheology. Tappi Journal 6(7), 17–23

Vergnes B, DellaValle G, Delamare L (1998). A Global Computer Software for Polymer Flows in Corotating Twin Screw Extruders. Polymer Engineering Science 38(11), 1781–1792

Vergnes B, Souveton G, Delacour ML, Ainser A (2001). Experimental and Theoretical Study of Polymer Melting in a Co-Rotating Twin Screw Extruder. International Polymer Processing 16(4), 351–362

Wang Y, White JL (1989). Non-Newtonian Flow Modelling in the Screw Regions of an Intermeshing Corotating Twin Screw Extruder. Journal of Non-Newtonian Fluid Mechanics 32(1), 19–38

Ward JC, Simpson WT (2001). USDA Agricultural Handbook AH-188. Dry Kiln Operator's Manual. Forest Products Laboratory, Madison, WI

Westenbroek APH (2000). Extrusion Pulping of Natural Fibre. PhD Thesis. University of Twente

White JL, Kim BJ, Bawiskar S, Keum JM (2001). Development of a Global Computer Software for Modular Self-Wiping Corotating Twin Screw Extruders. Polymer-Plastics Technology and Engineering 40(4), 385–405

Willems P, Kuipers NJM, De Haan AB (2008). Hydraulic Pressing of Oilseeds: Experimental Determination and Modeling of Yield and Pressing Rates. Journal of Food Engineering 89(1), 8–16

Yamaguchi H, Ohira Y, Kogure K, Mori S (1985a). Deformation and Strength Properties of Peat. Proceedings of 11th international conference on soil mechanics and foundation engineering 42461–2464

Yamaguchi H, Ohira Y, Kogure K, Mori S (1985b). Undrained Shear Characteristics of Normally Consolidated Peat Under Triaxial Compression and Extension Conditions. Soils and Foundations 25(3), 1–18

Zheng J (2014). Mechanical Pretreatment of Corncobs for Bioethanol Production by a Twin-Screw Extruder. PhD Thesis. The University of Western Ontario

(2010). ASTM D2216 Standard Test Methods for Laboratory Determination of Water (Moisture) Content of Soil and Rock by Mass. ASTM International, West Conshohocken, PA

(2011a). ASTM D2435 Standard Test Methods for One-Dimensional Consolidation Properties of Soils Using Incremental Loading. ASTM International, West Conshohocken, PA

(2011b). ASTM D3080 Standard Test Method for Direct Shear Test of Soils under Consolidated Drained Conditions. ASTM International, West Conshohocken, PA

(2018). ASTM D2573 Standard Test Method for Field Vane Shear Test in Saturated Fine-Grained Soils. ASTM International, West Conshohocken, PA

(2016). ASTM D4648 Standard Test Methods for Laboratory Miniature Vane Shear Test for SaturatedFine-Grained Clayey Soil. ASTM International, West Conshohocken, PA

Curriculum Vitae

Name Keller Joshell Hadassah George

Post-Secondary Education and Degrees

PhD in Chemical Engineering
Dissertation: Development of a Co-Rotating, Fully Intermeshing Twin-screw Extruder Model for the Extrusion of Natural Fibre Suspensions
The University of Western Ontario
London ON, Canada
2015 -2019

MESc in Chemical Engineering
Dissertation: Investigations in Hydrodynamics and Mixing Pattern in the Bubble Column Equipped with Internals
The University of Western Ontario
London ON, Canada
2013 - 2015

BSc in Chemical Engineering
Illinois Institute of Technology
Chicago IL, USA
2010 - 2013

Work Experience

Researcher

London ON, Canada
PhD in Chemical Engineering
2013 -2019

Teaching Assistant
London ON, Canada
PhD in Chemical Engineering
2014 -2019

Publications

George KJH, Jhawar AK, & Prakash A (2017). Investigations of flow structure and liquid mixing in bubble column equipped with selected internals. Chemical Engineering Science 170, 297-305

Conferences

KJH George (2018). Mechanical Properties of Poplar Fibers. 15th International Symposium on Bioplastics, Biocomposites and Biorefining, Guelph ON

KJH George, A Prakash (2014). Gas Holdup and Liquid Mixing in Bubble Column Equipped with Novel Internals. 64th Canadian Chemical Engineering Conference, Niagara Falls ON